UCRL 6036

UNIVERSITY OF CALIFORNIA

Ernest O. Lawrence

Radiation Laboratory

AEC RESEARCH AND DEVELOPMENT REPORT

LIVERMORE SITE

UCRL-6036
Nuclear Rocket &
Ramjet Engines, C-86
M-3679 (24th Ed.)

This document contains 146 pages.
This is copy 113 of 157 Series A .

UNIVERSITY OF CALIFORNIA
Lawrence Radiation Laboratory
Livermore, California

Contract No. W-7405-eng-48

PLUTO QUARTERLY REPORT NO. 4

(April – June 1960)

by

The Nuclear Propulsion Division Staff

July 1, 1960

DISTRIBUTION

Series A

	Copy No.
LRL Livermore,	
Information Division	1 - 15
Harold Brown	16
John S. Foster	17
C.M. Van Atta	18
Gerald W. Johnson	19
Theodore C. Merkle	20 - 24
Harry L. Reynolds	25
Richard P. Connell	26
James W. Bell	27
Roger E. Batzel	28
Albert J. Kirschbaum	29
Henry C. McDonald, Jr.	30
W. Blake Myers	31 - 35
Albert J. Rothman	36
James S. Kane	37
William C. Grayson, Jr.	38
LRL Berkeley,	
Wallace B. Reynolds	39
Hayden S. Gordon	40
LRL Mercury, Nevada,	
James L. Olsen	41
Division of Military Application, Washington,	
Brig. Gen. A.D. Starbird	42
U.S. Atomic Energy Commission, Washington,	
Irving Hoffman	43 - 50
Air Force Special Weapons Center	51
Air Research and Development Command (RDRAP)	52
Air Research and Development Command (RDRRA)	53
Air Technical Intelligence Center	54
Air University Library	55
Albuquerque Operations Office	56
Advanced Research Projects Agency	57

DISTRIBUTION (Contd.)

Series A

	Copy No.
Argonne National Laboratory	58
Army Ballistic Missile Agency	59 - 60
Assistant Secretary of Defense, R&D (WSEG)	61
Atomic Energy Commission, Washington	62 - 65
Atomics International	66
Battelle Memorial Institute	67
Brookhaven National Laboratory	68
Bureau of Naval Weapons	69 - 72
Bureau of Naval Weapons (SPO)	73
Bureau of Ships	74
Chicago Operations Office	75
Defense Atomic Support Agency, Sandia	76
Defense Atomic Support Agency, Washington	77
duPont Company, Aiken	78
General Electric Company (ANPD)	79 - 81
General Electric Company, Richland	82 - 83
Lockland Aircraft Reactors Operations Office	84
Los Alamos Scientific Laboratory	85 - 86
Marquardt Aircraft Company	87
National Aeronautics & Space Administration, Cleveland	88 - 89
National Aeronautics & Space Administration, Washington	90 - 91
New York Operations Office	92
Oak Ridge Operations Office	93
Office of Naval Research	94
Office of the Assistant for Operations Analysis DCS/O	95
Office of the Chief of Naval Operations	96
Patent Branch, Washington	97
Phillips Petroleum Company (NRTS)	98
Pratt and Whitney Aircraft Division	99
San Francisco Operations Office	100
Sandia Corporation	101
School of Aviation Medicine	102

DISTRIBUTION (Contd.)

Series A

	Copy No.
Union Carbide Nuclear Company (ORNL)	103
USAF Project RAND	104 - 105
U.S. Naval Postgraduate School	106
Wright Air Development Division	107 - 112
Technical Information Service Extension	113 - 157

PLUTO QUARTERLY REPORT NO. 4

Table of Contents

PLUTO QUARTERLY REPORT NO. 4

(April – June 1960)

Lawrence Radiation Laboratory, University of California
Livermore, California

CHAPTER I. TORY II-A

SECTION I. NEUTRONICS

Snoopy Experiments Involving Gaps between Core and Reflector

A series of experiments have been performed recently with the Snoopy system on assemblies which had gaps, or voids, between the core and side reflector. The motivation lies in the fact that the core and side reflector of Tory II-A are separated by such a gap, and the cost in reactivity is appreciable. An immediate application of the findings is illustrated in UCRL-5925: Chapter I, Section I. There, a calculational procedure is established which adequately treats the presence of a core-reflector gap using the diffusion codes Zoom and Angie.

Fourteen configurations were studied and are listed in Table I-1. Subsidiary experiments such as fission traverses and reactivity worth of incremental increases in critical height were also performed. Considerable information can be derived from the findings, independent of their fundamental relation to the computer codes. Values for reflector savings may be determined for various side reflector thicknesses. Reactivity costs of core-reflector gaps are available, as well as effects of addition of material to the gaps. The role of the end reflector has been studied as well as side reflector length. The latter group is three-dimensional in nature and so cannot be examined with the currently available codes at LRL.

Experimental Findings

The Snoopy experiments were performed in a standard way, as described in report UCRL-5175. The vane system utilized the graphite cruciform which

Table I-1. Critical Assemblies Containing Core-Side Reflector Gaps*

Exp. No.	L (in.)	W (in.)	H_c (in.)	H_c (corr.)[a] (in.)	T_r (in.)	T_v[d] (in.)	ρ_c (g/cc)	ρ_r (g/cc)	C/U^{235}	Comments
92	48.5	48.5	35.9	35.57	---	---	1.633	----	296	
93	42.5	42.5	32.11	31.92	6.0	---	1.632	1.70	295	$\frac{\Delta k}{\Delta H_c}$ = \$2.44/inch (Exp. 116)
94	42.5	42.5	29.16	28.97	12.0	---	1.636	1.70	295	± 10%[f]
97	42.5	42.5	33.32	33.13	6.0	1.0	1.632	1.70	295	
99	42.5	42.5	34.44	34.25	6.0	2.0	1.632	1.70	295	
103	42.5	42.5	35.49	35.30	6.0	3.0	1.632	1.70	295	
105	42.5	42.5	28.85	28.66	6.0	2.0	1.632	1.70	295	6.0" end reflector[b] [e]
106	42.5	42.5	28.63	28.44	6.0	2.0	1.632	1.70	295	7.0" end reflector, H_R = 30.3"
107	42.5	42.5	29.63	29.44	6.0	2.0	1.632	1.70	295	6.0" end reflector, H_R = 29.65"
111	42.5	42.5	34.2	34.01	6.0	3.0	1.632	1.70	295	Material in gap[c]
112	42.5	42.5	33.2	33.01	6.0	2.0	1.632	1.70	295	" " "
113	42.5	42.5	32.3	32.11	6.0	1.0	1.632	1.70	295	" " "
119	36.5	36.5	36.06	35.73	6.0	---	1.635	1.70	298	$\frac{\Delta k}{\Delta H_c}$ = \$1.96/inch (Exp. 121)
122	36.5	36.5	40.6	40.27	6.0	2.0	1.635	1.70	298	± 5%(f)

*See Fig. I-1.

(a) Corrected for vane slot voids.

(b) H_c + 6.0" = H_R, where H_R is the height of the side reflector.

(c) Stainless steel, 0.122" thick; aluminum, 0.72" thick; polyethylene, 0.124" thick.

(d) Density of aluminum honeycomb in gap: 0.018 g/cc.

(e) ρ (end reflector) = ρ (side reflector) for Exp. 105, 106, and 107.

(f) These values were found by performing a series of inverse multiplication measurements at two different assembly heights with a control rod calibrated in dollars.

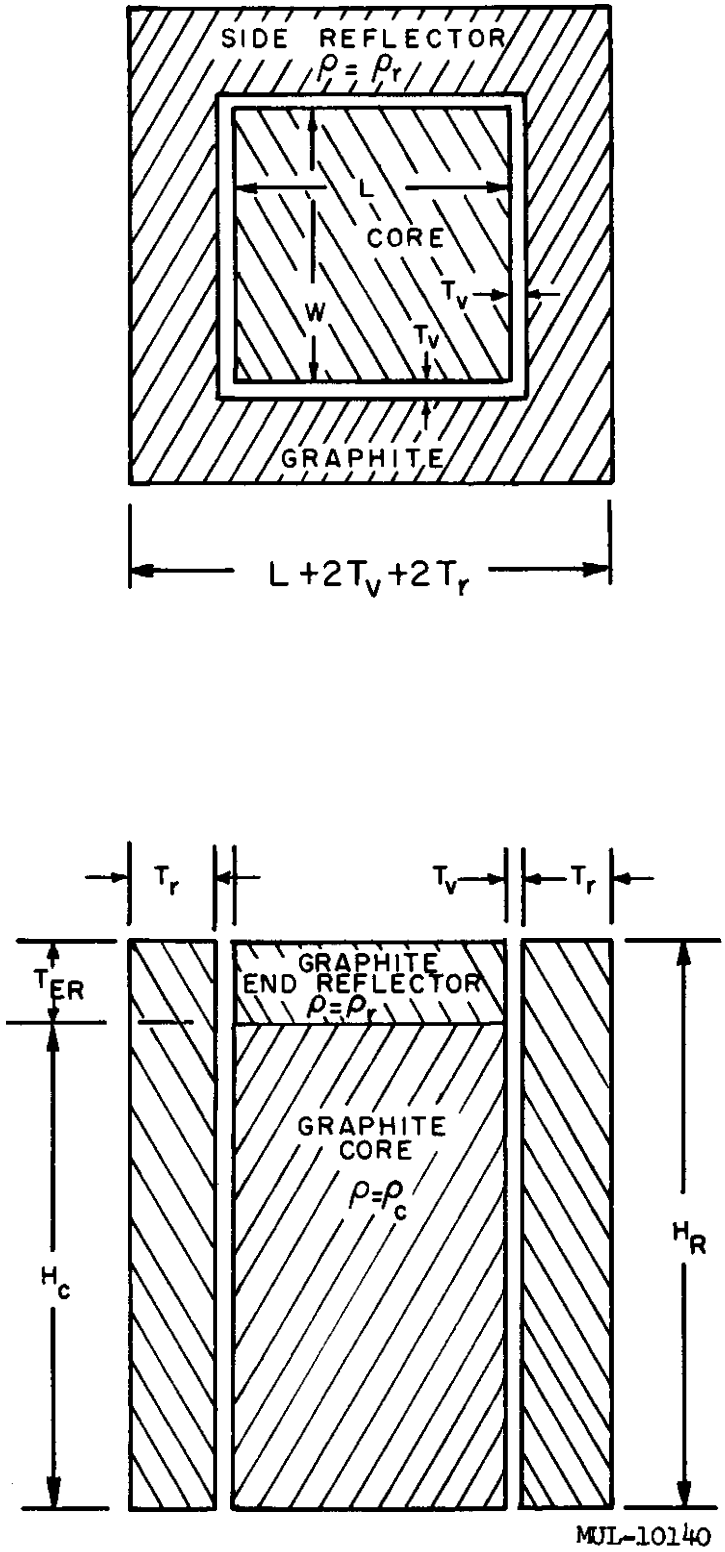

Fig. I-1. Critical assembly configuration for Table I-1.

accommodated cadmium vanes earlier. In the present series the vane contained enriched B^{10}. Corrections have been made to the critical height for the presence of the vanes. These were made on the basis of weighting the reduced density due to the vanes by ϕ^2. Such a procedure has been verified in the case of bare Spade BeO systems, where the gaps were in a median plane. See page 24 for Air Gap Studies with the Spade Facility, which lists the Spade experiments cited, and a demonstration of the validity of the weighting procedure. The corrections to the critical height were only about 0.2" in magnitude. The results are given in Table I-1.

The graphite employed was found by chemical analysis to contain from ten to fifteen atom parts per million by weight of boron. A pulsed neutron source experiment indicated a poison level equivalent to thirteen atom parts per million of boron. The nominal displacement of fuel foils was 4 mils per 1/2 inch. The fuel foils contained 93.2% U^{235} by weight. Reference is made to UCRL-5175 for more complete detail.

In addition to the experiments listed in Table I-1, several fission traverses on experiments 93, 97, 99, 103, 105, and 119 were performed using a fission counter. The studies were concentrated around the interface gaps. Axial traverses as well as traverses normal to the planes of the gaps were taken.

Reflector Savings

Several of the experiments performed are easily analyzed to determine the trade-off value of core material to reflector material. One speaks of "reflector savings" in this context. The exact definition employed in this paper differs from that of Glasstone and Edlund.[1] The quantity here is dimensionless:

$$\text{Reflector Savings} = \frac{\text{Thickness of core mod + fuel material, in g/cm}^2 \text{ which replaces reflector and maintains criticality}}{\text{Thickness of reflector, in g/cm}^2}$$

It is assumed that the core moderator is of the same material and approximate density as the reflector. In the present set of experiments, such a condition exists. Observe that as the reflector thickness decreases to zero, the reflector savings should approach unity. The reader should be alerted to the finding that reflector savings are a marked function of the core spectrum. For more thermal systems, the savings decrease more rapidly from unity

[1] Glasstone and Edlund, "Elements of Nuclear Reactor Theory," p. 234 (1952).

with increasing reflector thickness. The assemblies here have a median fission energy in the center of the core of approximately 20 volts. The calculations have been performed by reference to the fact that if the geometry of a critical reactor is varied such that its buckling is maintained constant, the reactor remains critical. Densities are assumed to remain constant. The data of Experiments 92, 93, 94, and 119 have been interpreted to yield results which are given in Table I-2 and Fig. I-2. The uncertainties are based on an uncertainty in the critical height, H_c, of ± 0.2 inches. Reflector thicknesses have been converted to correspond to reflectors of density: 1.633 g/cc ($= \rho_c$).

Table I-2. Reflector Savings

Core Cross Section	Reflector Thickness	Reflector Savings
42.5" × 42.5"	6.25"	0.980 ± 0.038
42.5" × 42.5"	12.50"	0.906 ± 0.044
36.5" × 36.5"	6.30"	0.945 ± 0.018

An additional value may be found from comparison of Experiments 99 and 105. The difference between the two experiments lies in the fact that the latter has an end reflector, 6 in. thick, while the former has a uniform core over the entire height of the core. Here

Reflector Saving = 0.89 ± 0.03.

It is clear therefore that for reactors which neutronically resemble the assemblies treated, reflectors of thickness less than 6 in. may be, after a slight correction for reflector savings, equated to core material and thereafter the resultant assembly could be considered as bare. This practice is warranted when one is concerned with the system reactivity. If, however, specific questions arise which are sensitive to the actual geometry and spatially dependent spectra of the original reflected system, the use of the notion of reflector savings may not be permitted. It is gratifying to find, experimentally, large values for reflector savings.

One notes also that the end reflector experiments cited must be treated by three-dimensional neutronic codes if they are to be solved analytically. These undoubtedly require a great deal of computer time and a large investment in development time and manpower. Cited here are experimental data

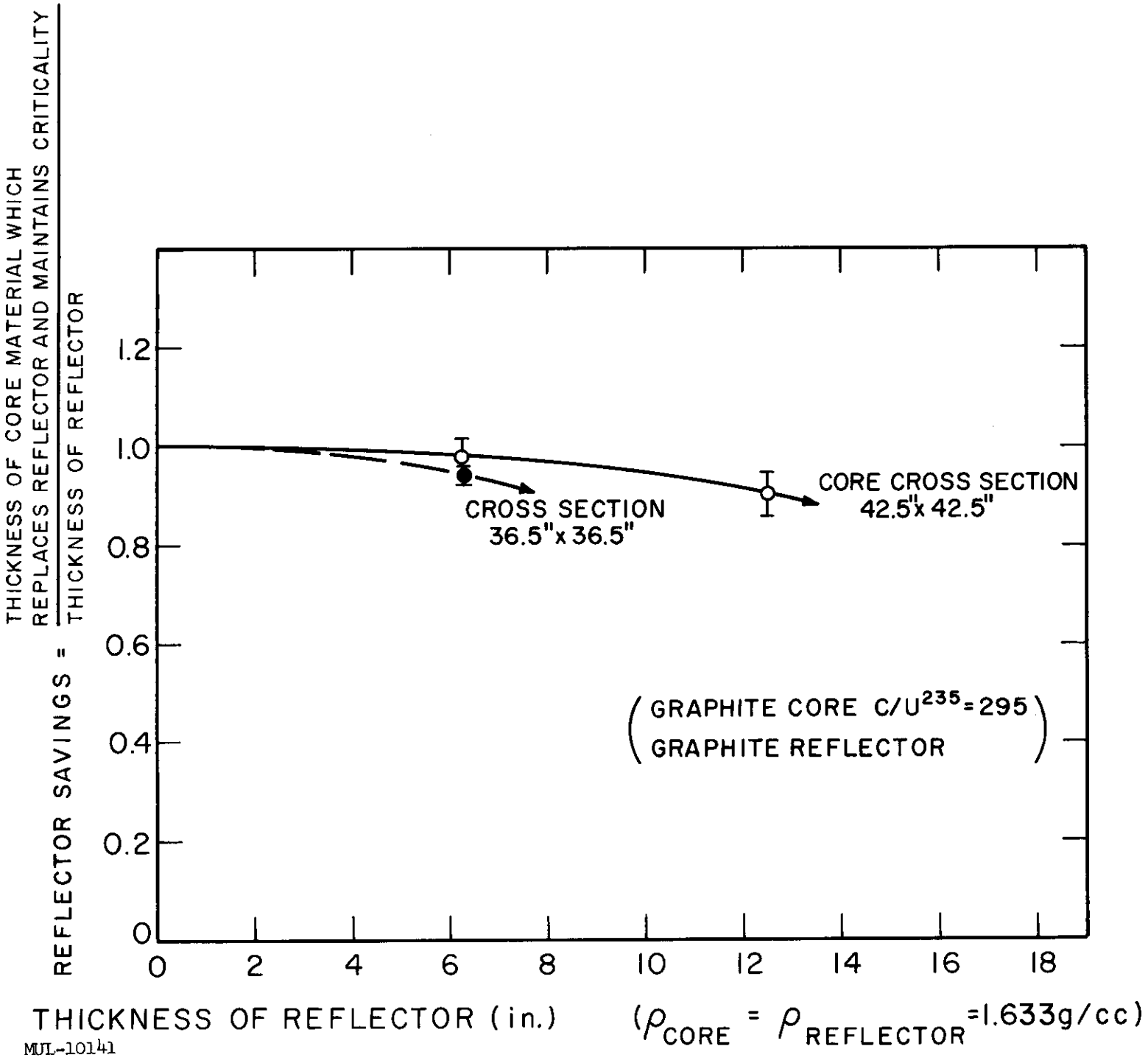

Fig. I-2. Reflector savings vs reflector thickness (Exps. 92, 93, and 94).

and interpretations which lead to the conclusion that there may be situations where that aspect of the problem which causes it to be three-dimensional in nature may be replaced by an equivalent description which renders the system two-dimensional, or even one-dimensional. To reiterate, three-dimensional codes are justified only when the accuracy of solution is noticeably affected by transformation to a simpler system.

Gap Studies: Core – Side-Reflector Gaps

A gap, or spacing between the core of a reactor and its reflector, has the adverse effect of uncoupling the core from reflector. In a cylindrical system or one similar to that which we consider here, the uncoupling is achieved by greater axial leakage from the gap openings because of a large migration length in the gap region. When the gap is sufficiently small, the loss is due to simple diffusion effects whereas large gaps allow streaming to occur as well.

Peripheral gaps ranging from 1 to 3 in. in width have been studied here. The neutronic effects have been found to be appreciable. The dependence of H_c, the critical height, on gap width, is illustrated in Fig. I-3; it summarizes some of the data of Table I-1. The variation is quite linear and so suggests a simple mechanism. Since, for small gap widths (i.e., $T_v \lesssim \lambda_{transport} \simeq 1.0$"), diffusion theory is expected to hold (see page 24), one would be inclined to feel that the linear behavior of H_c on T_v suggests that diffusion theory is applicable even at $T_v \simeq 3.0$ in. However, it may be that at larger values of T_v studied, the effect of streaming on H_c is counteracted by the tendency for H_c to approach a limiting value which corresponds to complete uncoupling of the reflector. This value is: $H_c^f = 43.5$ in. If linearity of H_c vs T_v persisted, a gap of 10.5 in. would yield the value of H_c^f, which is much larger than the maximum value of T_v treated. It would appear therefore that streaming plays a small role in the present set of experiments.

The cost in reactivity of the peripheral gaps may be derived from the findings of Exps. 116 and 121 (which apply to the geometries of Exps. 93 and 119, Table I-1).* The procedure involved converting the configuration of Exp. 119 (Table I-1) to a bare assembly with a buckling of 2.337×10^{-3} cm^{-2} ($\rho = 1.633$ g/cc) which is that value for the bare assembly of Exp. 92. The reflector savings value of Table I-2 was used, of course, since savings value

*See Comments, Table I-1.

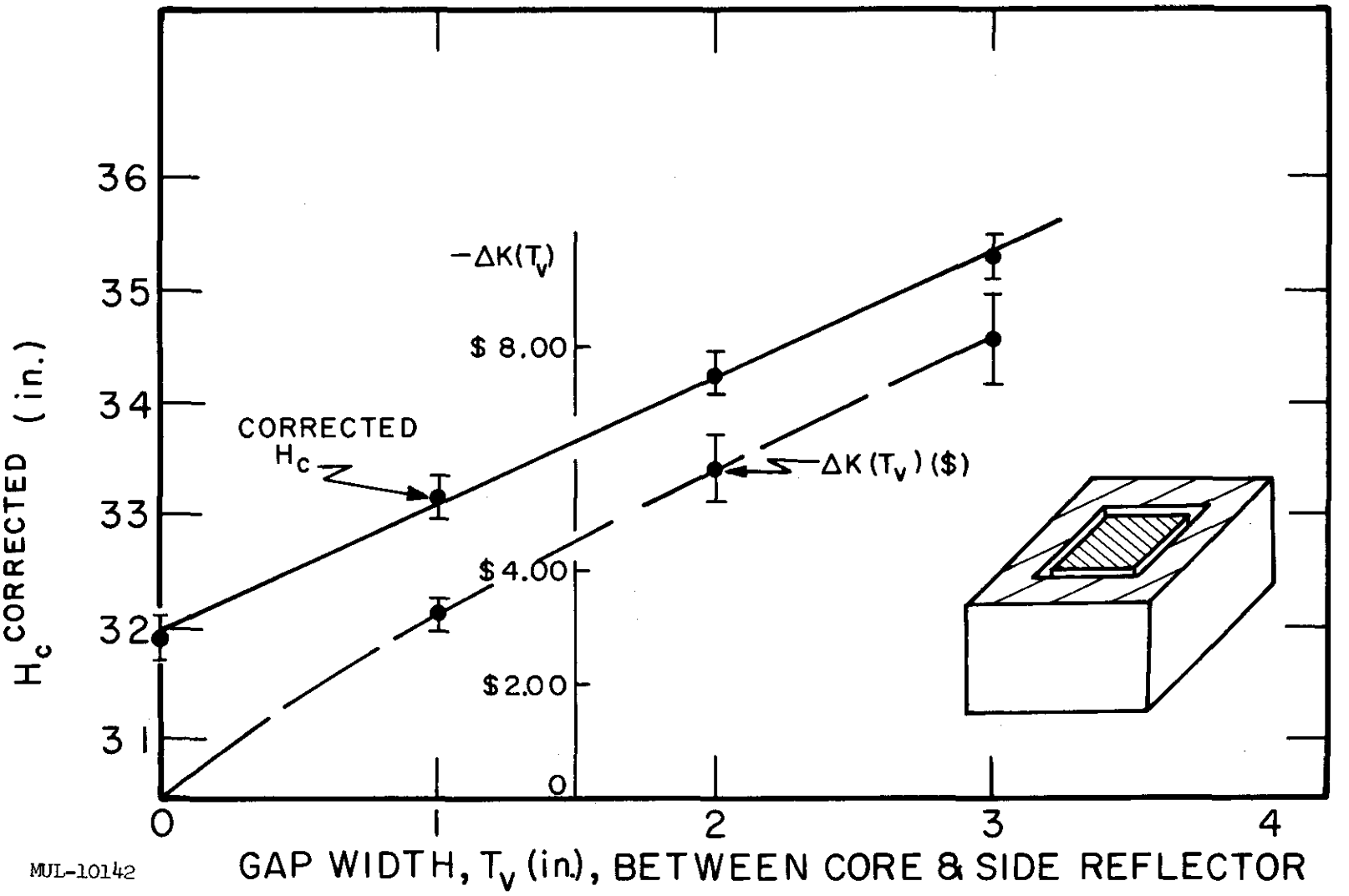

Fig. I-3. Effect of gap width of assembly with 42.5" × 42.5" core cross section on gap width.

was derived with reference to the buckling of the bare system. It is necessary to follow such a course in the calculations because a change in critical height has an effect on reactivity which depends on its effect on B^2. A computation gives, for Exp. 119,

$$dB^2/dH_c = 5.82 \times 10^{-5} \text{ cm}^{-2}/\text{in.}$$

which corresponds to

$$\Delta k_{eff}/\Delta H_c = \$1.96/\text{in. (Exp. 121)}$$

If we take $\beta = 0.0069$, it follows incidentally that

$$\Delta k/(\Delta B^2/B^2) = 0.542 \left(\frac{\text{absolute units of k}}{\text{fractional change of } B^2}\right)$$

The fraction is expected to be less than unity. In a thermal system, it can be shown to be $M^2B^2/(1 + M^2B^2)$, where $M^2 = \tau + L^2$. The large value of the fraction implies considerable leakage and therefore a nonthermal system in this situation. Since the fraction (dB^2/dH_c) varies as $(H_c + 2\Delta)^{-3}$, one may compute it for various values of H_c. A consistency check between Exps. 121 and 116 gives, on the basis of the latter dependence and the finding of Exp. 121, a value of \$2.72/in. for Exp. 116 whereas the measured value was \$2.44/in ± 10%. The disagreement is ~11% which is barely outside of the experimental uncertainty. Figure I-4 illustrates the dependence of $\Delta k/\Delta H_c$ on H_c, and also $\Delta B^2/\Delta H_c$ on H_c.

Figure I-3 depicts the cost in reactivity of the various gaps of Exps. 97, 99, and 103. An average of ~ \$3.00/in. of gap is observed, or roughly $\Delta k/\Delta T_v \simeq -0.020 \text{ in.}^{-1}$. Clearly these gaps have a significant effect on the neutron balance of the system.

A major justification for performance of the above experiments arises from the close dependence of digital computer calculations on such findings. A method was developed for treating voids with a diffusion code. There, one performs a sequence of calculations in which the gap is filled with successively less moderator material so that a relationship is developed between k_{eff} and (ρ/ρ_o) where ρ_o was taken as the reflector density. One then draws a tangent at some point of the curve and extrapolates to $\rho/\rho_o = 0$, for the correct k^o_{eff}. (In the present instance, $k^o_{eff} \sim 1.025$ as found from calculations for critical assemblies not containing gaps.) That point at which the tangent is drawn (to extrapolate to $k_{eff} = 1.025$) has been found to be $\rho/\rho_o \sim 0.5$. The validity for this scheme depends on proper interpretation

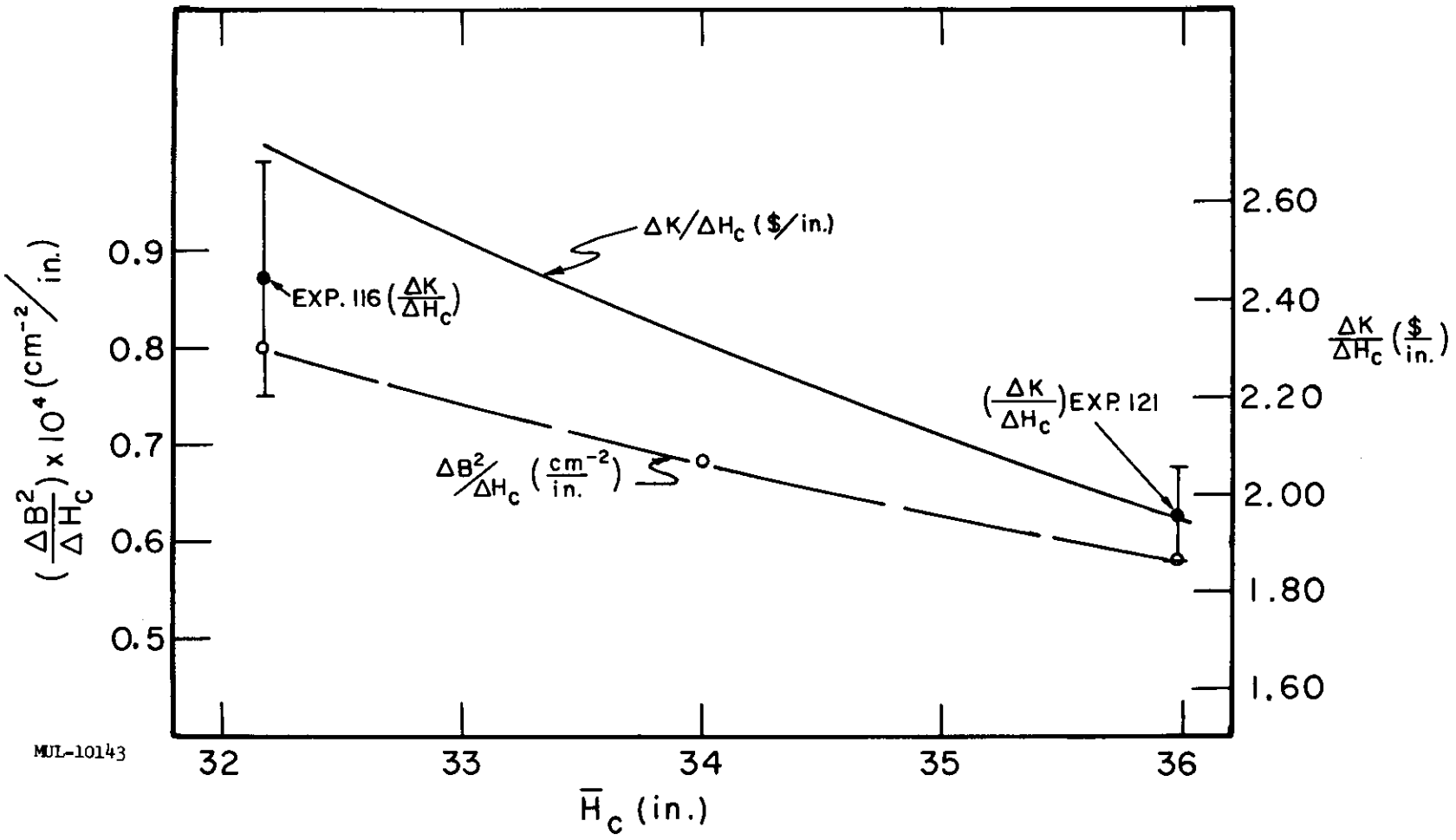

Fig. I-4. Dependence of $\Delta B^2/\Delta H_c$ and $\Delta k/\Delta H_c$ on critical height, H_c.

of the present experimental data. Clearly one assumes in the above recipe that $dk_{eff}/d(\rho/\rho_o)$ is constant for low values of ρ/ρ_o. Although the experiments were performed following a procedure where the reflector thickness was always 6.0" while the calculational recipe in effect varied reflector thickness, one could by recourse to the observations on reflector savings relate experiment to calculation. It has been verified that $dk_{eff}/d(\rho/\rho_o)$ is constant for values of ρ/ρ_o less than 0.5. The calculations are straightforward and will not be given here. Of course, if one deals with very large gaps (e.g., $T_v > 5$ in.), the recipe should be expected to fail.

Material Placed in Gap

An attempt was made to determine the effect on reactivity of structural material placed in the gap. The material was in the form of sheets and filled a one-inch gap almost completely. Directly in contact with the core was stainless steel, 0.122" thick. In contact with that was aluminum, 0.72" thick. A sheet of polyethylene 0.124" thick completed the sandwich. Their chemical analyses are given in Table I-3. Table I-1 lists the results as Exps. 111, 112, and 113. Reference to Fig. I-4, which gives $(\Delta k/\Delta H_c)$ ($/inch), demonstrates that the filler material has a constant reactivity effect of +$2.81 ±5% in the range: $1" \leq T_v \leq 3"$. Observe that a positive reactivity contribution is realized. It follows that the moderating effect of the filler material offsets its poisoning effect. Another observation may be made comparing the effect on reactivity of the filler material compared to graphite of equivalent thickness (ρ_r = 1.70 g/cc). Straightforward interpretation of Exps. 92, 93, and 94 yields the result that the material is 0.50 as effective as graphite of equal thickness (ρ_r = 1.70 g/cc).

Length of Side Reflector

Experiments 106 and 107 were performed to demonstrate the effect of length of the side reflector on reactivity. In actual construction of a reflected reactor, it is often impossible to have a side reflector whose length, H_R (see Fig. I-1) is equal to the total reactor length. In the experiments under attention, the length of an end-reflected critical system was modified, and H_R was adjusted to return the system to criticality. In Exp. 106 (as compared to Exp. 105), the end reflector thickness was increased effectively 0.75" and H_R was decreased 4.36". (The former number takes into account a correction for slight change in H_c.) Experiment 107 differed from its predecessor, Exp. 106, by conversion of the innermost inch of end reflector to active core volume.

The effect was to decrease H_R by 0.65 in. Two trade-off values result:

$$\Delta T_{\text{end refl.}} = 1.0'' \rightarrow \Delta H_R = 5.82''$$

and

$$\Delta H_{\text{core}} = 1.0'' \rightarrow \Delta H_R = 6.48''$$

Table I-3. Chemical Analyses of Gap Filler Material

Element	SS-304	Aluminum	Polyethylene
(Spectroscopic)[a]			
B	ND	ND	ND
Cd	ND	ND	ND
Mn	8000 ± 30%	--	--
Mo	8000 ± 30%	--	--
Sl	4000 ± 30%	--	--
Tl	200	--	--
Sm	ND	ND	ND
Gd	ND	ND	ND
Eu	ND	ND	ND
Dy	ND	ND	ND
Cu	5000 ± 30%	--	--
(Chemical)[b]			
Cr	19%		
Ni	9.5%		
Fe	70%		
P			
S			
Thickness	0.122"	0.72"	0.124"

(a) All entries in parts per million by weight.
ND = not detectable.

(b) Entries as weight percent.

An additional finding is that of a sort-of reflector savings of the end reflector:

$$(\text{Reflector Saving})_{\text{End Reflector}} = 0.90$$

This is in agreement with the earlier finding of 0.89 ± 0.03, although the details of the experiments differ.

One sees therefore that slight deviations of side reflector length from a desired value affects the reactivity slightly. In the present geometry, one finds $(\Delta k/\Delta H_R) \simeq \$0.40$/in., or ~ 0.003/in. in absolute units.

Summary of Angie Calculations

All experiments listed in Table I-1 except those of three-dimensional nature (i.e., Exps. 105-7) have been represented in various Angie (two-dimensional) calculations. The results are given in Table I-4. Those values of k_{eff} for the configurations not containing gaps fall uniformly around $k_{eff} = 1.025$. Ideally, k_{eff} should be unity. The discrepancy is not understood. It is not due to the two-dimensional nature of the problem since the k_{eff} of Exp. 92, a bare parallelepiped, is also 1.025. Both Angie and Zoom (the one-dimensional code) utilize eighteen energy groups of equal logarithmic width. The cause of the discrepancy may lie in the choice of cross sections. Improvements are currently being made in the techniques of computing the cross sections. Also, newer experimental data are being incorporated.

In configurations involving gaps from 1 to 3 in. in thickness, a sensible value for that (ρ/ρ_r) at which extrapolation of the tangent to the k_{eff} vs (ρ/ρ_r) curve is made is

$$(\rho/\rho_r) \simeq 0.50\ (\pm 0.05)$$

Report UCRL-5925* illustrates in detail the technique for determining the proper k_{eff} for a system containing a gap.

The value of k_{eff} for Exp. 113 (i.e., 1" gap filled with stainless steel, aluminum and polyethylene) is 1.037, or ~ 0.012 higher than others in Table I-3. Since it was found experimentally that the filler material added \$2.81 to the system reactivity which is $\Delta k \simeq 0.0194$, the error implies a ~60% overestimate of the effect of the gap material. Expressed another way, the error of $\Delta k \simeq 0.012$ is equivalent to $\Delta H_c = 0.7$ in. which is much larger

* Chapter I, Section I.

Table I-4. Summary of Results of Angie Calculations

Exp. No.	L (in.)	W (in.)	H_c (corr.)[a] (in.)	T_r (in.)	T_v (in.)	C/U^{235}	k_{eff}[b]	$(\rho/\rho_r)_T$[c]	Comments
92	48.5	48.5	35.57	---	---	296	1.0255	---	
93	42.5	42.5	31.92	6.0	---	295	1.0253	---	
94	42.5	42.5	28.97	12.0	---	295	(1.0163)[d]	---	
97	42.5	42.5	33.13	6.0	1.0	295	---	0.54[d]	
99	42.5	42.5	34.25	6.0	2.0	295	---	0.45[d]	
103	42.5	42.5	35.30	6.0	3.0	295	---	0.50[d]	
111	42.5	42.5	34.01	6.0	3.0	295	---	0.57	Material in Gap[e]
112	42.5	42.5	33.01	6.0	2.0	295	---	0.25	Material in Gap[e]
113	42.5	42.5	32.11	6.0	1.0	295	1.0371	---	Material in Gap[e]
119	36.5	36.5	35.73	6.0	---	298	1.0258	---	
122	36.5	36.5	40.27	6.0	2.0	298	---	0.42	

[a] Corrected for vane slots.

[b] Density of core assumed in all cases to be: $\rho_c = 1.633$ g/cc. Reflector density: $\rho_r = 1.70$ g/cc.

[c] Value of (ρ/ρ_r) within gap at which tangent to k_{eff} vs (ρ/ρ_r) should be drawn. Extrapolation to $(\rho/\rho_r) = 0$ gives k_{eff} for system with gap. See Text.

[d] Estimated from results of previous work reported in UCRL-5925.

[e] Composition given in Table I-3.

than the uncertainty of ± 0.2 in. A possible direction for explanation of the discrepancy may be toward the transport character of the filler material. Since it differs radically from the surrounding moderator, subtle transport corrections may be in order. The surprisingly low value of $(\rho/\rho_r)_T$ of Exp. 112 is a further indication of incomplete understanding of gap material effects of the type examined.

Fission traverses in several of the assemblies were made using a commercial fission counter which contains a very thin layer of U^{235}. Figures I-5 and I-6 compare the experimental findings of Exps. 93 and 119, and the corresponding results from Angie. The peaks in the experimental curves arise because of spaces between fuel foils. The traverses were taken normal to the face of a side reflector and approximately centered on the face. Agreement is seen to within ± 10% in the (Power per Unit Unshielded Fuel Mass) as a function of position, except within the side reflector. There, the computed value is ~15% below the measured value.

Figures I-7 and I-8 show experimental traverses normal to a side reflector for a 1" and 2" gap (i.e., Exps. 97 and 99). The uncoupling effect is very recognizable.

Vertical traverses in the gaps have shown some rather interesting results. The traverses had a characteristic cos $[\pi x/(L + 2\Delta)]$ shape. The extrapolation length, Δ, however, varied radically from expected values. Within the core proper, $\Delta \simeq 2.0$ cm whereas in the gap of Exp. 99, $\Delta = 7.6$ cm! The traverses of Exp. 105, shown in Fig. I-9, also exhibit this anomaly. The latter observation illustrates the risk one takes in performing traverses or worth determinations in regions of low density. For example, "rod bump" determinations of control rods when performed near the outer surfaces of the assembly, will give answers that will be in error because of the existence of the assembly hole which accommodates the rod.

In the end-reflected system, Exp. 105, traverses showed a marked peaking in the end reflector. A vertical traverse in the gap did not show this. Figure I-9 illustrates the findings.

The Angie results are seen, therefore, to agree satisfactorily with the experiments where comparisons may be made. A few isolated and relatively unimportant discrepancies persist. The agreement between experimental and calculated traverses is particularly gratifying.

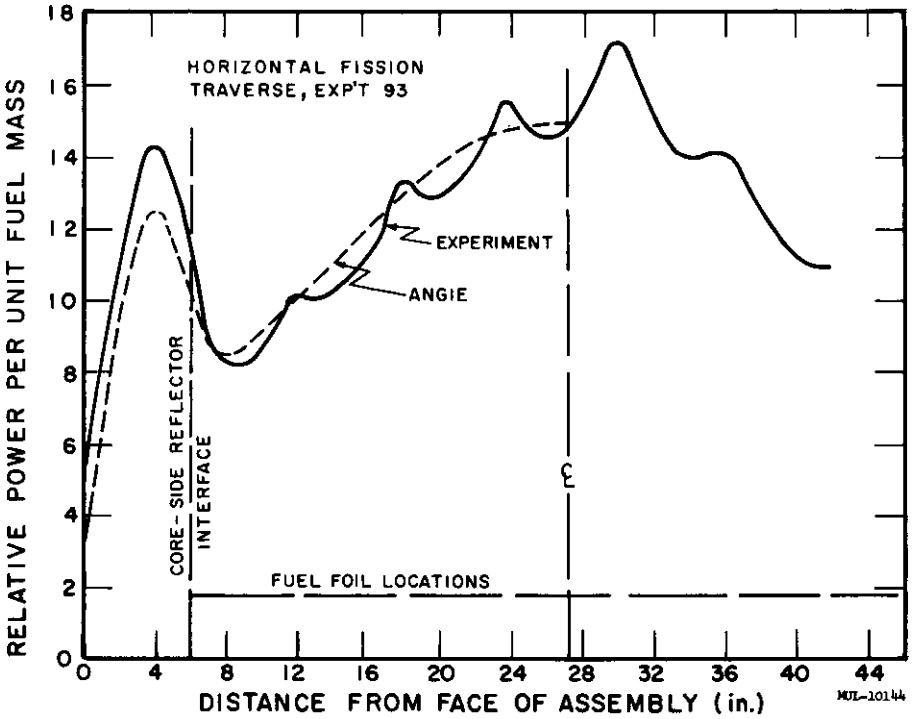

Fig. I-5. Horizontal fission traverse, Exp. 93.

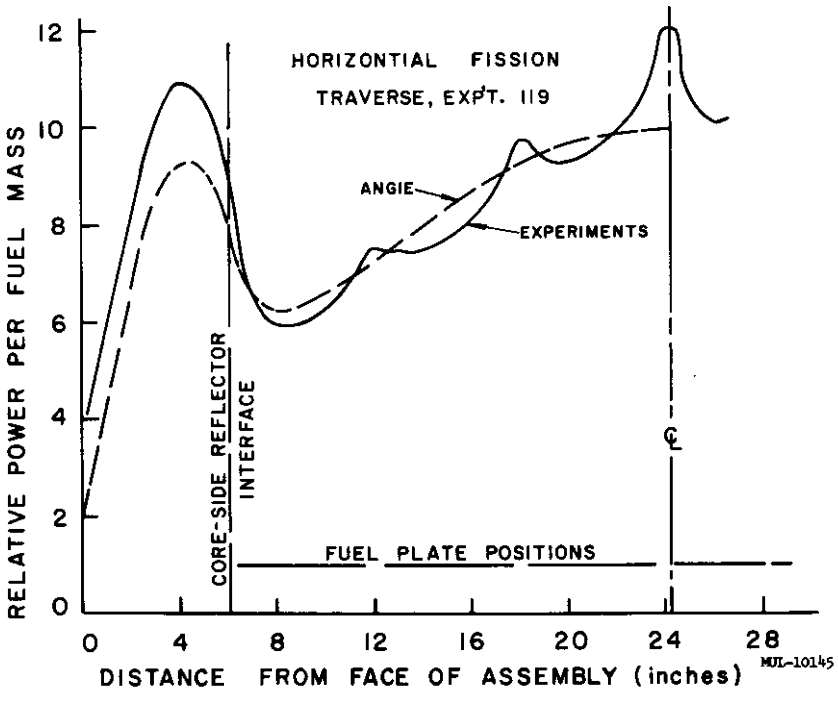

Fig. I-6. Horizontal fission traverse, Exp. 119.

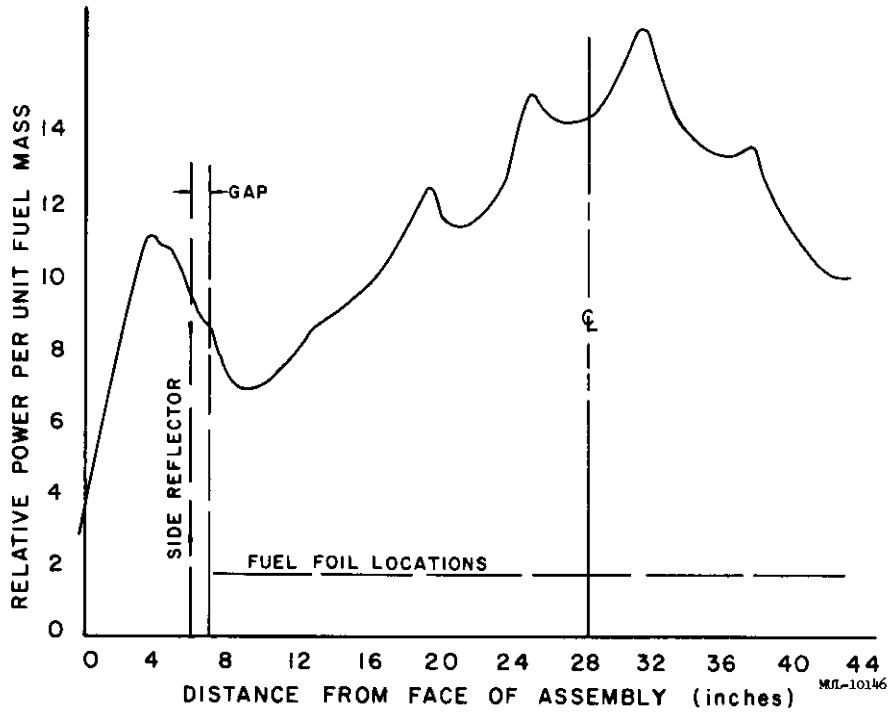

Fig. I-7. Horizontal fission traverse, Exp. 97.

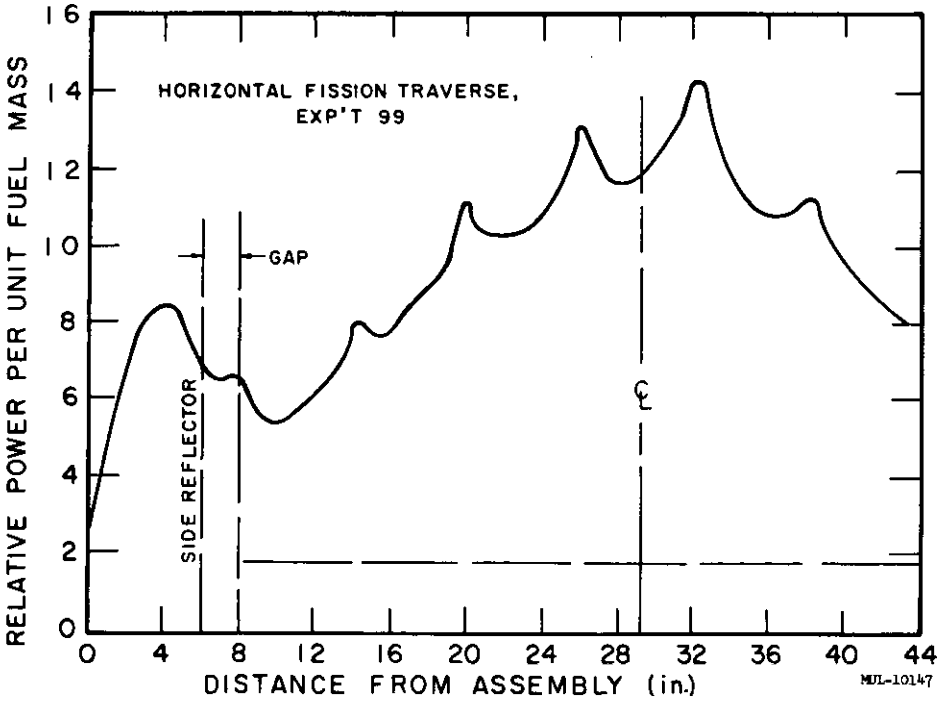

Fig. I-8. Horizontal fission traverse, Exp. 99.

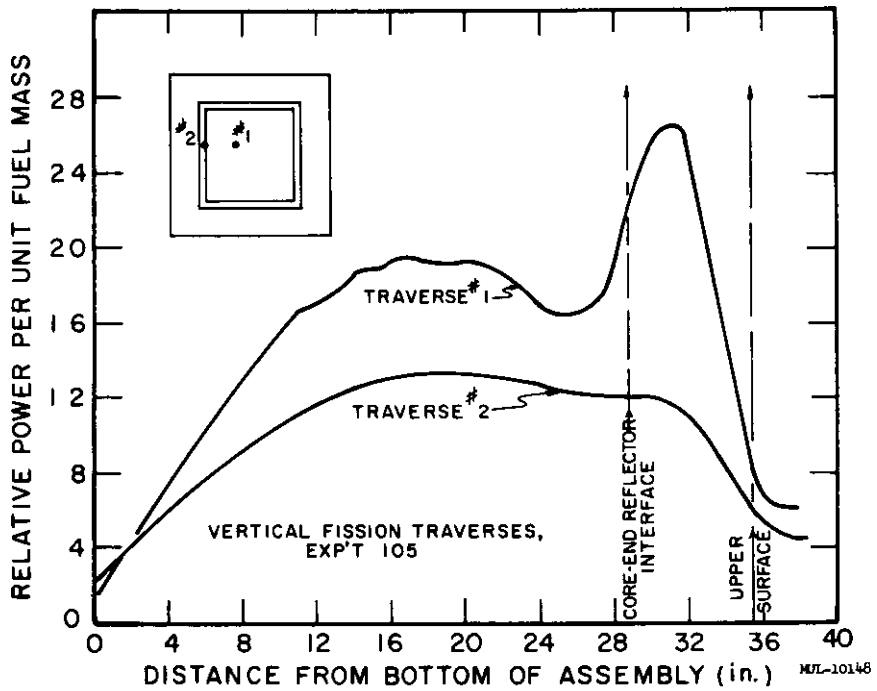

Fig. I-9. Vertical fission traverses, Exp. 105.

Conclusions

1. In an attempt to understand more clearly the nature of gaps between core and reflectors fourteen different critical assembly experiments were conducted. These involved graphite as core moderator and reflector material. The core was loaded with enriched uranium (i.e., 93.2% U^{235}) to a molar ratio of

$$C/U^{235} \simeq 295:1$$

2. Values of reflector savings were derived directly from the experiments. For 6-in. reflectors, savings values ranging from 0.89 to 0.98 were found, depending on the geometry.

3. Direct reactivity effects of core-side reflector gaps were determined. In the geometry considered, a cost of

$$\Delta k_{eff}/\Delta T_{void} \simeq -0.020 \text{ in.}^{-1}$$

was found. There was no clear indication of neutron streaming from gaps up to 3 in. in thickness.

4. A representation of structural material in the gap — namely, a sandwich of stainless steel, aluminum and polyethylene — had a significant effect on reactivity. The sandwich had an effect independent of gap thickness.

5. End reflectors were studied. A reflector savings value for a 6-in.-thick end reflector was determined to be 0.89.

6. The effect of a variation in side reflector length was related to core length variation. It was found that an increase in core length of a critical reactor of 1.0 in. requires a decrease in side reflector length of 5.8 in. in order to remain critical.

7. A calculational technique has been established which allows the use of a neutron diffusion code in determining the reactivity of a reactor which contains major voids.

8. Generally good agreement was observed between the Angie results and experiment. A value of $k_{eff} = 1.025$ was found for the basic systems in the present family. Agreement with measured fission traverses was satisfactory.

Air Gap Studies with the Spade Facility

A variety of critical assembly experiments have been performed on the Spade facility to investigate effects of different kinds of gaps in reactors. One set was concerned with bare rectangular parallelepipeds split in two at a median plane. The gaps were no larger than one inch. Another set dealt with "sandwich crits" (see Fig. I-10), and gaps in the median plane of the core as well as at the core-reflector interface were studied. A third set dealt with "box crits" (see Fig. I-11), and gaps were present at the core-reflector interface.

The results are listed in Table I-4. In all cases, the BeO core density was $\rho_{BeO} = 2.86$ g/cc, the graphite reflector density was $\rho_g = 1.70$ g/cc.

The BeO was found, from a pulsed neutron source experiment, to have a 7 ± 4 mb thermal neutron absorption cross section, indicating the absence of impurities.[1] By the same procedure the graphite indicates a poison level equivalent to 13 atom parts per million. Chemical analysis gives for the latter 12.5 ± 2.5 atom parts per million of boron which is in good agreement with the pulsed neutron determination.[2]

---

[1] UCRL-5369, Pt. 1 (Revised).

[2] UCRL-5175, p. 4.

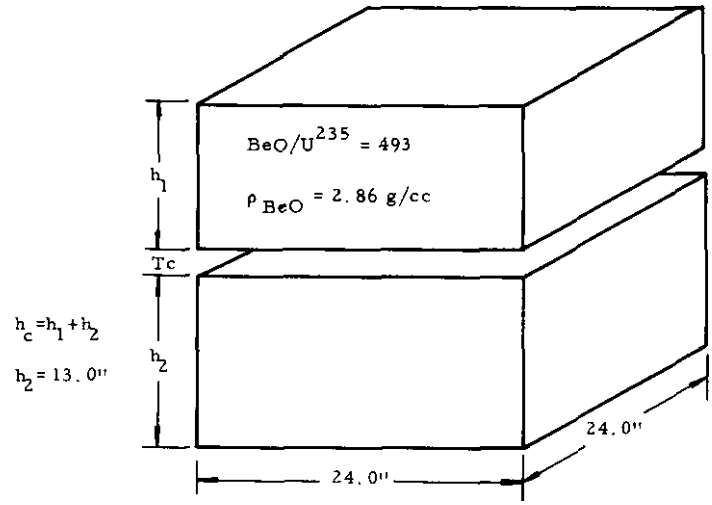

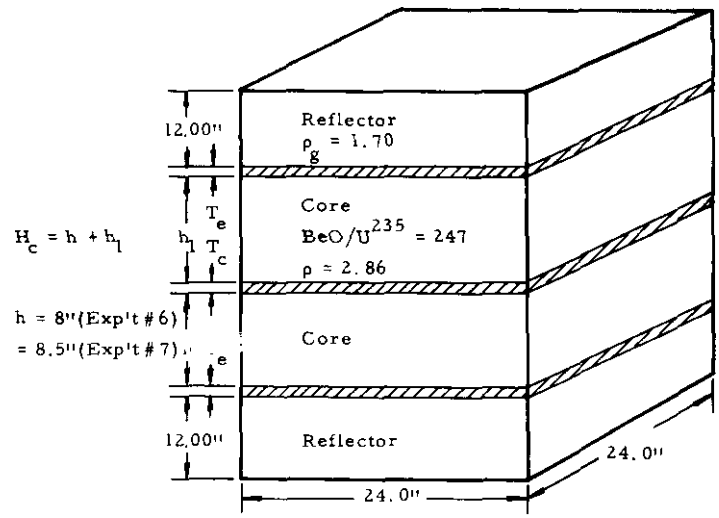

Fig. I-10.

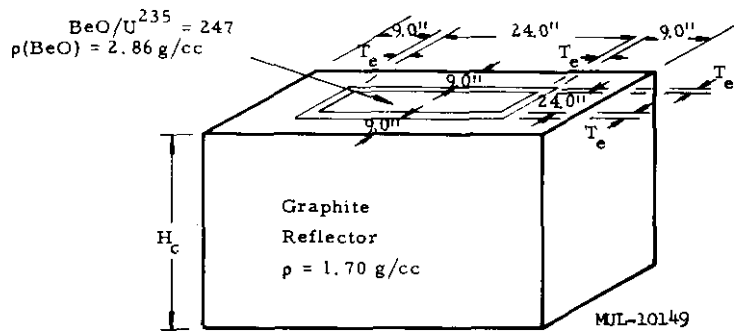

Fig. I-11.

Neutronic Worth of Gaps

The first group of experiments listed in Table I-5 deals with very simple configurations, which enables one to employ the concept of buckling. In particular, it is of interest to establish whether removal of moderator material from a simple bare system results in a predictable change in buckling.

Table I-5

Exp. No.	Description	BeO/U^{235}	T_c (in.)	T_E (in.)	H_c[a] (in.)	"Void" Contents
1	Bare BeO	493	---	---	22.2	---
2	Bare BeO	493	0.470	---	24.53	Hexcell Al (ρ = 0.053)
3	Bare BeO	493	0.937	---	27.56	Hexcell Al (ρ = 0.053)
4	Bare BeO	493	0.970	---	25.53	Hexcell, 1/2" graphite ρ = 1.70
5	Sandwich	247	---	---	14.4	---
6	Sandwich	247	0.470	---	16.54	Hexcell Al (ρ = 0.053)
7	Sandwich	247	0.937	---	18.96	Hexcell Al (ρ = 0.053)
8	Sandwich	247	---	0.47	15.47	Hexcell Al (ρ = 0.053)
9	Box	247	---	---	16.25	Styrofoam (ρ = 0.032)
10	Box	247	---	0.50	16.6	Styrofoam (ρ = 0.032)
11	Box	247	---	1.00	17.0	Styrofoam (ρ = 0.032)
12	Box	247	---	1.063	17.3	air

[a] H_c is the critical height not including the gaps, T_c or T_e.

It is shown in the present section that the neutronic worth of a moderator varies simply as ϕ^2. It is necessary in the calculation to employ the fact that if a reactor (1) of dimensions, ${}_1r_i$, and densities ${}_1\rho_i$, is critical, then another (2) in which $({}_2r_i)$, $({}_2\rho_i) = ({}_1r_i)\,({}_1\rho_i)$ is also critical. A corollary is

$$B_2^2 = B_1^2 \times (\rho_2/\rho_1)^2$$

in the case of a bare homogeneous system. The above expressions are simply an argument from constancy of mean-free-paths.

The buckling of Exp. 1 of Table I-4 is found to be $(7.72 \pm 0.05) \times 10^{-3}$ cm^{-2} at a BeO density of 2.86 g/cc. The uncertainty is due to the accuracy of measuring H_c (i.e., $\pm$ 0.2 in.). The buckling of the Exp. 2 is 7.145×10^{-3} cm^{-2} while that of Exp. 3 is 6.64×10^{-3} cm^{-2}. Here, the extrapolation length is 1.3 cm, and overall dimensions determine the buckling. Now in the case of Exp. 2, the apparent change in density is

$$\frac{\Delta\rho}{\rho} \simeq \frac{0.47}{25.0} = 0.019$$

However, the gap is in a median plane and so $\overline{\phi^2_{gap}}/\overline{\phi^2} = 2.0$. $\overline{\phi^2_{gap}}$ is averaged over the gap. The effective density change is then twice that listed above. Applying the argument of constancy of mean-free-paths, one finds

$$B^2 \text{ (Exp. 2)} = 7.71 \times 10^{-3} \text{ cm}^{-2} (\rho_{eff} = 2.86)$$

One sees agreement within the accuracy of the experiment. The overall change in active critical height was 2.3 in. An uncertainty of $\pm$ 0.2 inches implies then an experimental uncertainty in the test of $\pm$ 9%.

In Exp. 3, we find by the same procedure,

$$B^2 \text{ (Exp. 3)} = 7.61 \times 10^{-3} \text{ cm}^{-2} (\rho_{eff} = 2.86)$$

Here the agreement is not as good. Observe however that the difference in B^2 is equivalent to a $\Delta H_c = 0.47''$, whereas the active core height change was 5.36". In other words the ϕ^2 procedure accounted for 91% of the effect of the larger gap.

The latter slight disagreement is reasonable. One expects the streaming mechanism to become more important as the gaps increase in width. The tendency would be to require a larger critical height than would be predicted by the ϕ^2 rule. A smaller value for B^2 would result. The findings of Exp. 3 are in accord with this. Unfortunately, quantitative estimates of streaming are not quite justified because of the accuracy of the experiment.

Revised Tory II-A-1 Fuel Loading Distribution

The fuel distribution as specified can be considered essentially final. In fact, assembly of the first core is actually under way according to the fuel element loading map as shown in Figs. I-12 and I-13.

The first part of this section describes the basic assumptions and constants which were used in neutronic calculations preparatory to the fuel chart. This chart has been dated May 16, 1960.

Basic Assumptions Leading to the Fuel Map of May 16, 1960 (Fig. I-12)

The characteristic parameters which entered into the determination of the present fuel distribution can be summarized as follows: (All data are nominal and are listed at ambient temperatures.)

1. For the Core

Average fuel loading[1]	5.954 wt%
max loading	7.49 wt%
min loading	3.53 wt%
Average, effective, fueled BeO density	3.049 g/cc
Percent of theoretical density in fueled BeO	97
Percent of theoretical density in structural BeO	96
Total mass of fueled BeO	859.352 kg
Total mass of structural BeO	4.1868 kg/in.
Total mass of BeO, from fueled	808.183 kg
Total mass of OyO_2	51.168 kg
Total mass of U-235	41.980 kg
Total mass of U-238	3.063 kg
Moderator to U-235, molar ratio	222.68
Total, equivalent, frontal area of reactor	839.569 in^2
Equivalent frontal area of fueled BeO	386.466 in^2
Equivalent frontal area of structural BeO	88.478 in^2
Total flow area through fuel tubes	272.26 in^2
Total flow area through tension tubes	21.19 in^2
Total, equivalent frontal void area	343.385 in^2
Porosity[2]	0.4133
Core length: medium, fueled region	44.506 in.
Core volume in fueled region	37,365.858 in^3
Use of tension tubes with an equivalent, total frontal area of	21.19 in^2
Flat-to-flat dimensions, fuel tubes	0.297 in^2
Flow orifice diameter, fuel tubes	0.2005 in^2
Number of fueled tubes in core cross section	8623
Theoretical density of OyO_2	10.83 g/cc
Theoretical density of BeO	3.008 g/cc
Self-shielding in Hastelloy tension tubes	yes

[1] Weight OyO_2/Weight of total fueled BeO.

[2] Ratio of flow area to frontal area of fuel elements.

2. For the Gap Region Between Core and Reflector

Equivalent frontal area of shroud	10.612 in^2
Corresponding to an equivalent thickness of	0.09844 in.
Equivalent frontal area of pressure vessel	77.213 in^2
Equivalent frontal area of coolant water	11.495 in^2
Self-shielding in shroud Hastelloy	yes
Correlation to Snoopy critical assemblies	yes

3. For the Side Reflector

Equivalent frontal area of graphite	3998.008 in^2
Equivalent frontal area of coolant water	147.264 in^2
Equivalent frontal area of aluminum	48.888 in^2
Equivalent frontal area of voids	12.56 in^2
Calculational uncertainty in area determinations	±0.1%
Average, measured density of dry graphite	1.784 g/cc
Average, measured water absorption in graphite	1.755%
Average, measured, thermal graphite cross section with impurities but without absorption water	5.835×10^{-4} cm^{-1}
Self-shielding in boron steel tubes	yes

4. For the Inlet Reflector

Flat-to-flat dimension of tubes	0.297 in^2
Flow orifice diameter in tubes	0.2005 in.
Percent of theoretical density	97
Same equivalent, frontal areas as those pertaining to the fueled core region	
Thickness of reflector	6.046 in.

5. For the Exit Reflector

Flat-to-flat dimension of tubes	0.297 in.
Flow orifice diameter in tubes	0.2005 in.
Percent of theoretical density	97
Same equivalent, frontal areas as those pertaining to the fueled core region	
Thickness of reflector	2.000 in.

6. For the Front Retainer Plate

Thickness of Rezistal R-347 plate	0.250 in.
Approximately the same equivalent frontal area is assumed for the Rezistal plate as that of the combined fueled and structural BeO in the core	474.944 in^2

7. For the Base Plate

Material of plate	0.5 Ti-Mo
Approximately the same equivalent frontal area is assumed for the base plate as that of the combined fueled and structural BeO in the core	474.944 in^2

A realization of the above magnitudes for the enumerated parameters is expected to permit the reactor to go critical at a control vane angle position of 68°. This pertains to core temperatures corresponding to high power operation.

As to the power density variations across fuel elements at the design point, it is expected to be essentially ± 2.5%. On the other hand, contrary to the considerations of ± 3% azimuthal power density variation, it was felt this time that the local effect of vanes, etc., was still relatively small, in view of other uncertainties. The fuel element class distribution as shown in Figs. I-12 and I-13, therefore, does not include azimuthal perturbations in the loading pattern.

The reduction in fuel, in contrast to what was originally predicted, can be attributed primarily to the net effect of the following items, some of which acted to counter a gain in reactivity:

a. Realization of a higher density in fueled BeO, namely, 97% of theoretical, instead of 96%.

b. Realization of a higher density in structural BeO, namely, 96% instead of 94% previously assumed.

c. Application of self-shielding effects, and hence reduction in the neutron capture, in tension tubes, in the shroud, and in the boron tubes of the control vanes.

d. Re-evaluation of the end effects in the light of more up-to-date data.

e. Realistic information for parameters of the side reflector, based upon recent analysis of components.

f. Improved neutronic representation of the distribution of structural BeO in the core and the array of tension tubes.

g. Correlation of Tory II-A neutronic calculations with those interpreting the findings from "Snoopy" critical experiments.

Effect of Photoneutrons on Shutdown Power

An evaluation of the contribution of delayed photoneutrons from the $Be^9(\gamma, n)$ reaction in Tory II-A to the reactor power after shutdown has been made.

Experimental data from Hot Box (report UCRL-5829) was used to determine an effective (γ, n) cross section for a BeO assembly; this information together with known fission product gamma decay rates after specific reactor

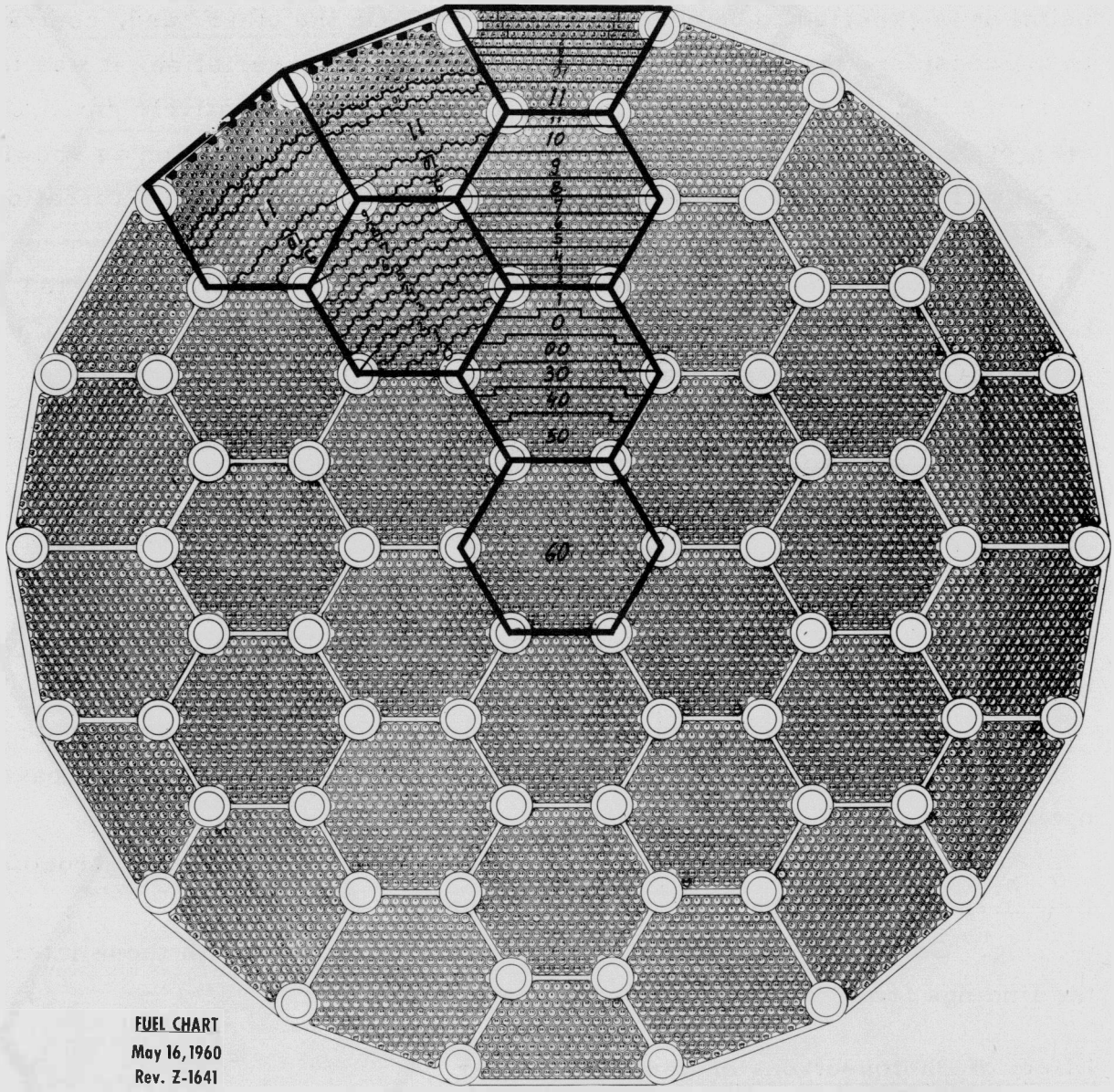
11
10
9
8
7
6
5
4
3
2
1
0
90
30
40
50
60
FUEL CHART
May 16, 1960
Rev. Z-1641
MUL-9560

Fig. I-12.

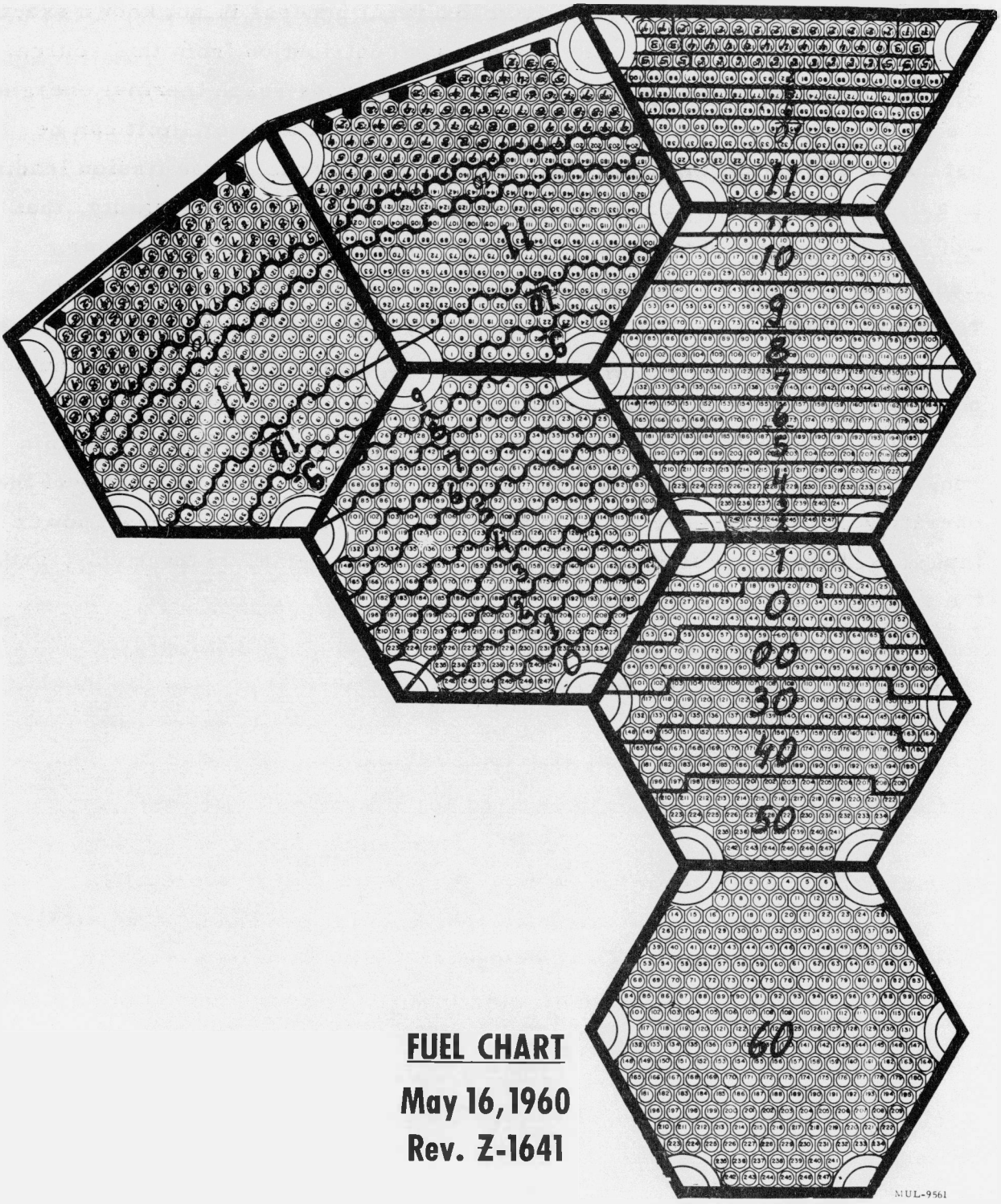

Fig. I-13.

operation times yields a photoneutron production rate as a function of time after shutdown.

Since the neutron spectrum from $Be^9(\gamma, n)$ process is not known exactly, it is difficult to imply a specific fission rate contribution from this source. However, assuming that at best all of these neutrons reach thermal energies, the probability that these will cause fission is ~0.8; a lower limit can be established by assuming that only 1 of 2.5 neutrons will cause fission leading to a 0.4 probability. We can say, therefore, with a 30% uncertainty, that ~60% of the photoneutrons will contribute to the after-shutdown power. Additional considerations must take into account the amount of negative reactivity introduced at the end of the reactor operation, this will affect the multiplication of the photoneutrons and determine the effective after-shutdown photoneutron power level.

It was found that for a negative reactivity step of $0.8 after a 1-min run, the photoneutron power level 5 minutes after shutdown is ~0.5% of the operating power. This level is comparable with the after-shutdown power that is contributed by fission product gammas and betas, respectively, under the same operating conditions.

SECTION II. TORY II-A AEROTHERMODYNAMICS*

1. During this reporting period the Tory II-A aerothermodynamic design analysis was completed. A representative set of design point parameters for the major Tory II-A components is given in Table I-6.

Table I-6

Component Design Point Parameters	
Design Point Criteria:	
Reactor inlet stagnation pressure	357 psia
Reactor inlet stagnation temperature	846°K
Fuel element maximum wall temperature	1505°K
Exit nozzle geometric area	326.24 in.
Typical Fuel Element	
Exit stagnation temperature	1343°K
Exit Mach number	0.63
Exit stagnation pressure	229 psia
Single conduit power	17.45 kw
Flow per tube	30.1 g/sec
Total fuel element power	151 Mw
Total fuel element flow	611 pps
Maximum fuel element wall temperature	1505°K
Typical Tie Rod	
Exit stagnation temperature	903°K
Exit Mach number	0.717
Exit stagnation pressure	273.4 psia
Single conduit power	31 kw
Flow per tube	482 g/sec
Total tie rod power	2.23 Mw
Total tie rod flow	76 pps
Maximum tie rod wall temperature	996.4°K
Shroud	
Exit stagnation temperature	862°K
Exit Mach number	0.293
Exit stagnation pressure	210 psia
Shroud power	317 Mw
Shroud flow	38 pps
Maximum conduit wall temperature	863°K

* Details of the calculational techniques used in Tory II-A aerothermodynamic analyses will be presented in a forthcoming UCRL report.

At the design point, the maximum temperature of the front support is expected to be about 870°K. The maximum base plate temperature should be about 1350°K, the structural link maximum temperature about 1420°K, and the wiper seal maximum temperature about 1090°K.

The total design point power of Tory II-A should be about 156 Mw. Total reactor flow rate at design conditions is expected to be 726 pps.

2. For purposes of nuclear control system and operational analysis, a lumped parameter transfer function has been derived. For reasonable operational situations, the lumped parameter recipe should predict the average fuel element temperature to within 2% of its true value at any time.

3. Floss III, the multizone, single-element, steady-state aerothermodynamic code, has been successfully used as a subroutine for a multi-element, multizone, steady-state aerothermodynamic code. The name of this new code, which is in IBM 709 production status, is NOMAC. It is now possible to calculate a complete set of parameters for a reactor containing structural as well as fueled elements. Entropy increases due to non-ideal geometries are included in the computer matching calculations. The gas velocity profile in the upstream feed duct is assumed to be independent of lateral position. Exit nozzles need be specified only as regards their isentropic geometries; the NOMAC program determines exit nozzle parameters for cases of subsonic through supersonic flow.

SECTION III. TORY II-A CONTROLS

During the current reporting period, Stage IV (analog-electronics-console) and Stage V (final systems checkout) were successfully completed and the power control system hardware was delivered to NTS or the cold critical facility as applicable. Stages I, II and III were reported in Pluto Quarterly Report No. 3 (UCRL-5925) for January-March 1960. Stage V results will be briefly summarized herein.

The tests carried out during Stage V include all the tests outlined previously in Section II(4) of the last report No. 3 and the following additions (continuing with step e of item 6 in subsection 4.1 of report No. 3):

6. Checkout of Log Power System

e. Response to Reactivity Disturbances

Power Level – P_o

Flow Rate – $\dot{W}_o$

Temperature – T_{c_o}

Period – 5 second demand

Reset Level – $P = 1.2\ P_o$, $\tau = 1$ second

Scram Level – $P = 3\ P_o$ (Log), $\tau = 1$ second

$P = 1.5\ P_o$ (Linear)

Reactivity Disturbances – ± 10¢, ± 20¢, ± $1.00

Objective – Measure stiffness of log power control system to reactivity disturbances

Record – Log P_{Demand}, Log P, $\dot{W}$, T_c, X_{rod}, θ_{vane}, P, K/τ, δk

f. Response to Flow Disturbances

Power Level – P_o

Flow Rate – Step flow rate $\dot{W}_o \rightarrow 0.1\ \dot{W}_o \rightarrow \dot{W}_o$

Temperature – Variable about T_{c_o}

Period – 5 second demand

Reset Levels – $P = 1.2\ P_o$, $\tau = 1$ second

Scram Levels – $P = 3\ P_o$ (Log), $\tau = 1.0$ seconds

$P = 1.5\ P_o$ (Linear)

Objective – Measure stiffness of log power control system to coolant disturbances

Record – Log P_{Demand}, Log P, $\dot{W}$, T_c, X_{rod}, θ_{vanes} (all 8), $X_{safety\ rod}$ (both), K/τ

g. Loss of Vernier Rod

Power Level – Ramp change $0.1\ P_o \rightarrow P_o \rightarrow 0.1\ P_o$

Flow Rate – Ramp change $0.1\ \dot{W}_o \rightarrow \dot{W}_o \rightarrow 0.1\ \dot{W}_o$

} 60 second ramp

Temperature – Constant

Period – 5 second demand

Reset Levels – $P = 1.2\ P_o$, $\tau = 1$ second

Objective – Determine response and stability of log power system when operating on vanes only

Record – Log P_{Demand}, Log P, $\dot{W}$, T_c, X_{rod}, θ_{vanes} (all 8), $X_{safety\ rod}$, K/τ, ϵ_p

7. Checkout of Scram Override System

a. Slewing One Control Element

Power Level – $P(o) = P_o$

Flow Rate – $\dot{W}(o) = \dot{W}_o$

Temperature – Variable about T_{c_o}

Period Demand – 5 seconds

Reset Level – $1.2\ P_o$, $\tau = 1$ second

Objective – Determine effect of slew operation of one control element while in the (1) manual, and (2) automatic control modes

Procedure – While in (1) manual, (2) automatic slew first one rod, then one vane, in and out. Move the control elements the minimum amount possible by going from hold to slew to hold as rapidly as possible.

Record – P_{Demand}, P, $\dot{W}$, T_c, X_{rod}, θ_{vane} (all 8), $X_{safety\ rod}$ (1), K/τ

b. Slewing All Control Elements

Power Level – $P(o) = P_o$

Flow Rate – $\dot{W}(o) = \dot{W}_o$

Temperature – Variable

Period Demand – 5 seconds

Reset Level – $1.2\ P_o$, $\tau = 1$ second

Objective – Shut down reactor as slowly and smoothly as possible using "override in."

Procedure – With reactor at initial conditions above, shut down reactor by use of "override in" switch. In order to minimize thermal stresses, move control elements in as small increments as possible by rapid switching of the "override in" switch.

c. Operator Scram Test

Power Level – P_o

Flow Rate – $\dot{W}_o$

Temperature – $T_c(o) = T_{c_o}$

Period Demand – 5 seconds

Reset Levels – 1.2 P_o, τ = 1 second

Scram Levels – 3 P_o (Log), τ = 1 second

1.5 P_o (Linear)

Procedure – At initial conditions above, scram reactor with scram button and record variables shown below until all control elements are fully inserted.

Record – P_{Demand}, P, $\dot{W}$, T_c, X_{rod}, θ_{vane} (all 8), $X_{safety\ rod}$ (both), $X_{osc.\ rod}$

d. Pump Failure Scram Test

Power Level – $P(o) = P_o$

Flow Rate – $\dot{W}(o) = \dot{W}_o$

Temperature – $T_c(o) = T_{c_o}$

Period Demand – 5 seconds

Reset Levels – 1.2 P_o, τ = 1 second

Scram Levels – 3 P_o (Log), τ = 1.0 seconds

Objective – To determine how long control system can run on accumulator charge after pump breakdown.

Procedure – At the initial conditions indicated, turn off pump, simultaneously taking power and flow rate from P_o, $\dot{W}_o$ to 0.1 P_o, 0.1 $\dot{W}_o$ on a 15 second ramp. Hold at 0.1 P_o and 0.1 $\dot{W}_o$ until scram occurs.

Record – P_{Demand}, P, $\dot{W}$, T_c, X_{rod}, θ_{vane} (all 8), $X_{safety\ rod}$ (both), $X_{osc.\ rod}$

8. Miscellaneous

Demonstrate that the reactor control system can be switched from Manual to Automatic, Automatic to Manual, Linear Power to Log Power (while in the automatic mode) and Log Power to Linear Power (while in automatic) without switching transients.

Record – P_{Demand}, Log P_{Demand}, P, Log P, X_{rod}, θ_{vane} (all 8), $X_{safety\ rod}$, K/τ

During Stage V all transient tests were run from 0.1 P_o (where P_o denotes full design power) to P_o and back to 0.1 P_o rather than from 0.2 P_o as in previous stages. System response was checked down to 0.02 P_o (the limit of the reactor analog simulation) and found to be satisfactory.

Figure I-14 shows in block diagram form the hardware which was included in the Stage V checkout. Figure I-15 shows the analog computer setup. Except for the reactor analog simulation and the Auxiliary Control Panel, all components shown are the actual Tory II-A hardware. The only power control system components not included in this checkout were the Vernistats which will be used to program power level and air flow rate at the control point (thus, they will be included in the console). Because the Vernistats were not ready for use at checkout time, the Auxiliary Control Panel was used in their place. It was used to program δk disturbances as well as air flow rate and power. For convenience it was located next to the analog computer and the system electronics during the checkout tests as shown in Fig. I-16. Figures I-17 and I-18 show several views of the electro-hydraulic actuation systems as mounted on the flatcar during Stage V tests.

Several of the Stage V test results are shown in the figures which follow:

Figure I-19 shows the closed-loop small-signal frequency response of the power control system with rod and vanes and with vanes only. It is seen that $-90°$ phase shift occurs at $\omega = 2\pi(6.4)$ rad/sec which is slightly lower than the design value of $\omega = 2\pi(9.5)$ rad/sec. The difference is caused by the slightly lower frequency response of the vernier rod actuator.

Figure I-20 shows the system response to ± 90% steps of power demand while Figure I-21 shows the system response to ± 90% steps of power demand and reactor air flow rate. These two situations represent the most extreme

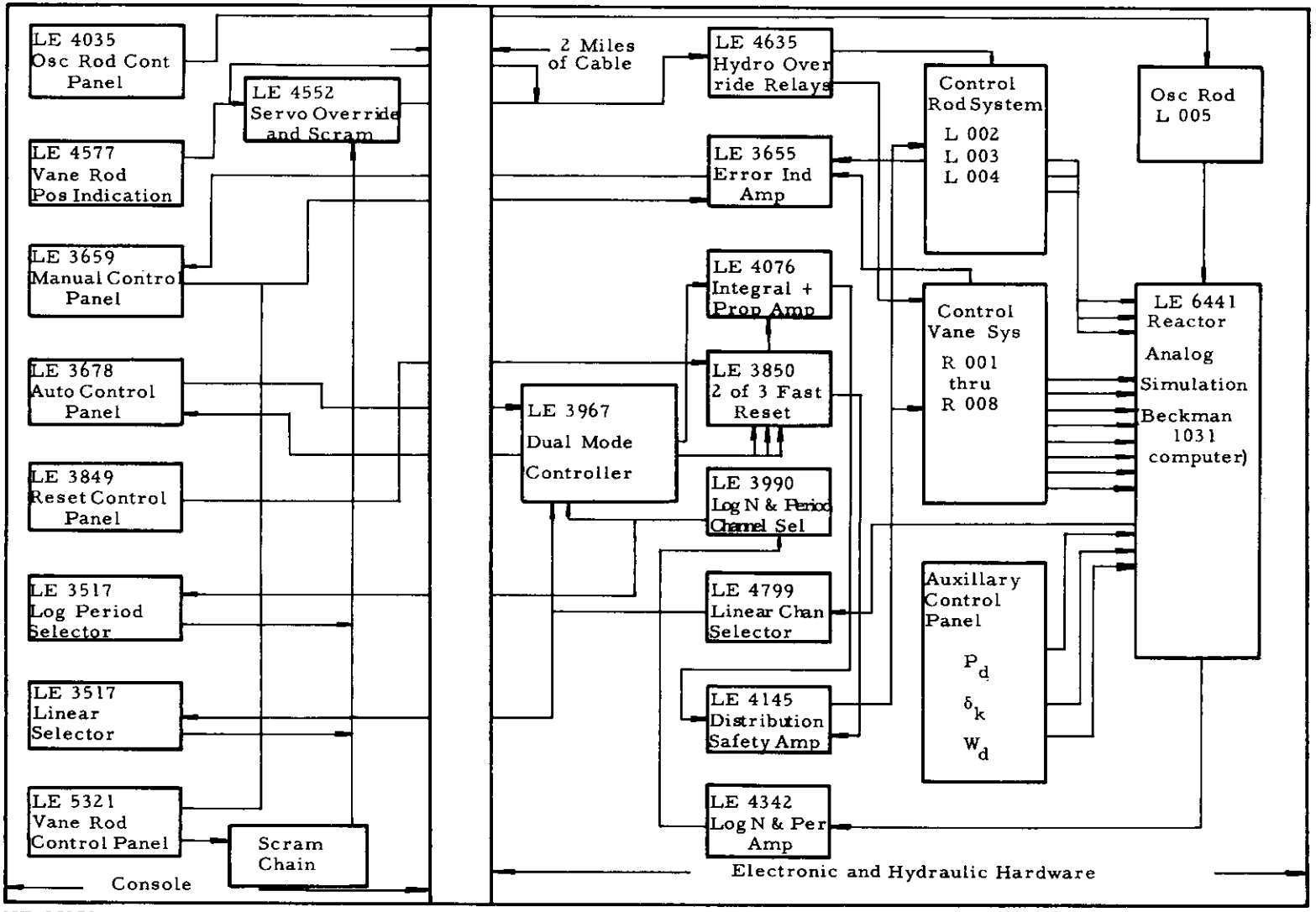

MUL-10150

Fig. I-14. Block diagram of the hardware included in Stage V checkout. (Drawing numbers are included.)

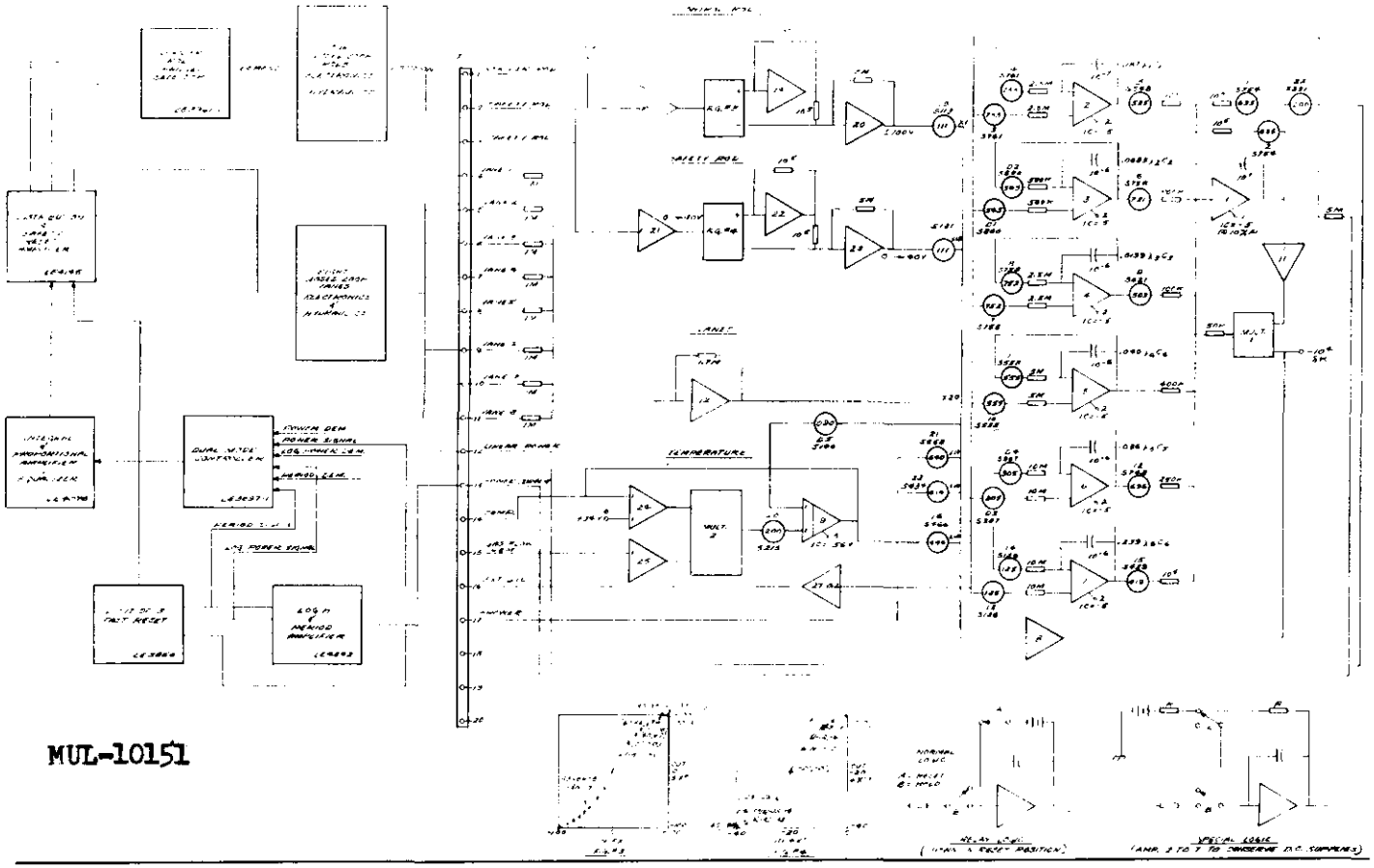

Fig. I-15. Analog computer setup used for reactor simulation during Stage V results.

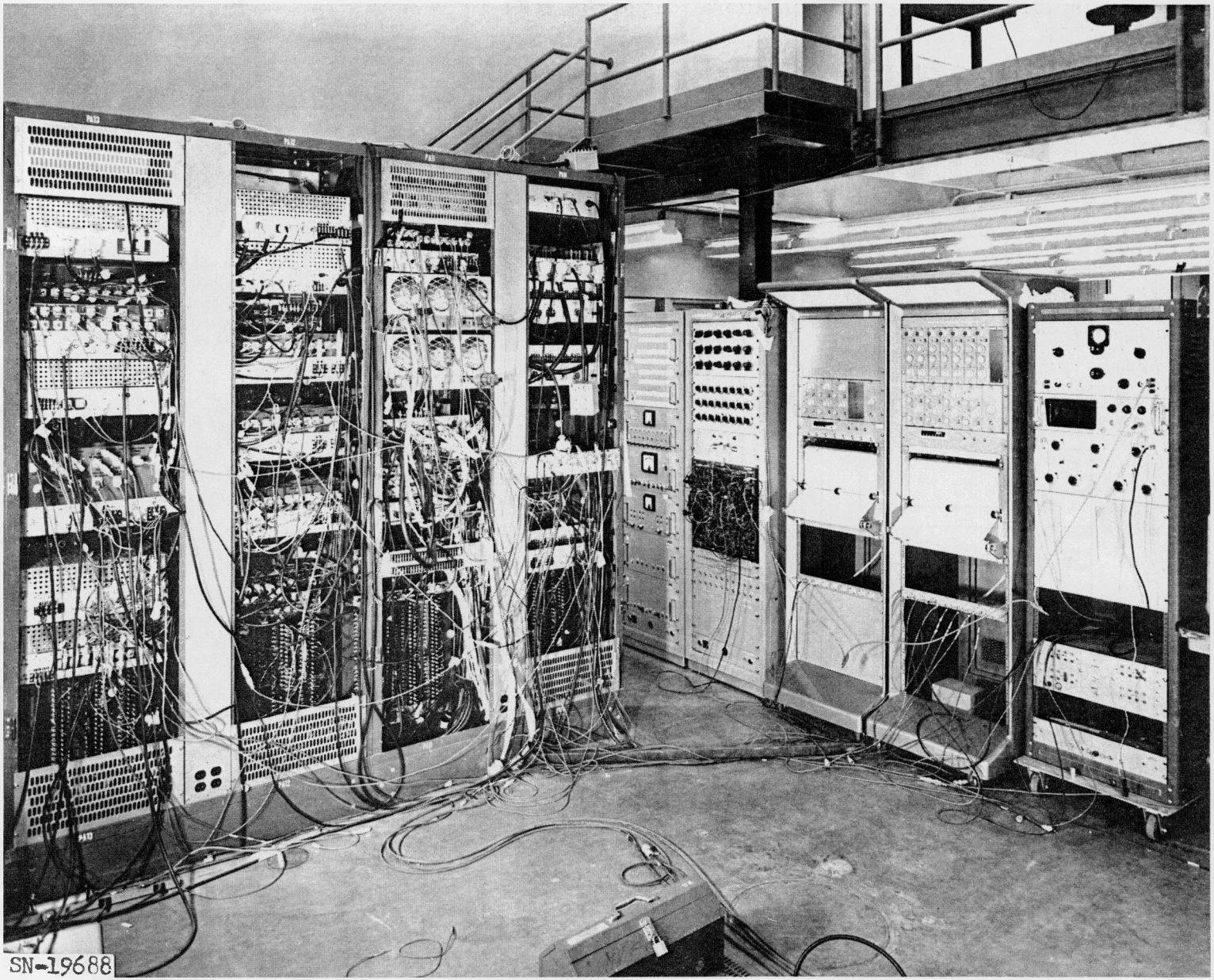

Fig. I-16. View of system electronics, analog computer and auxiliary control panel as used during Stage V checkout.

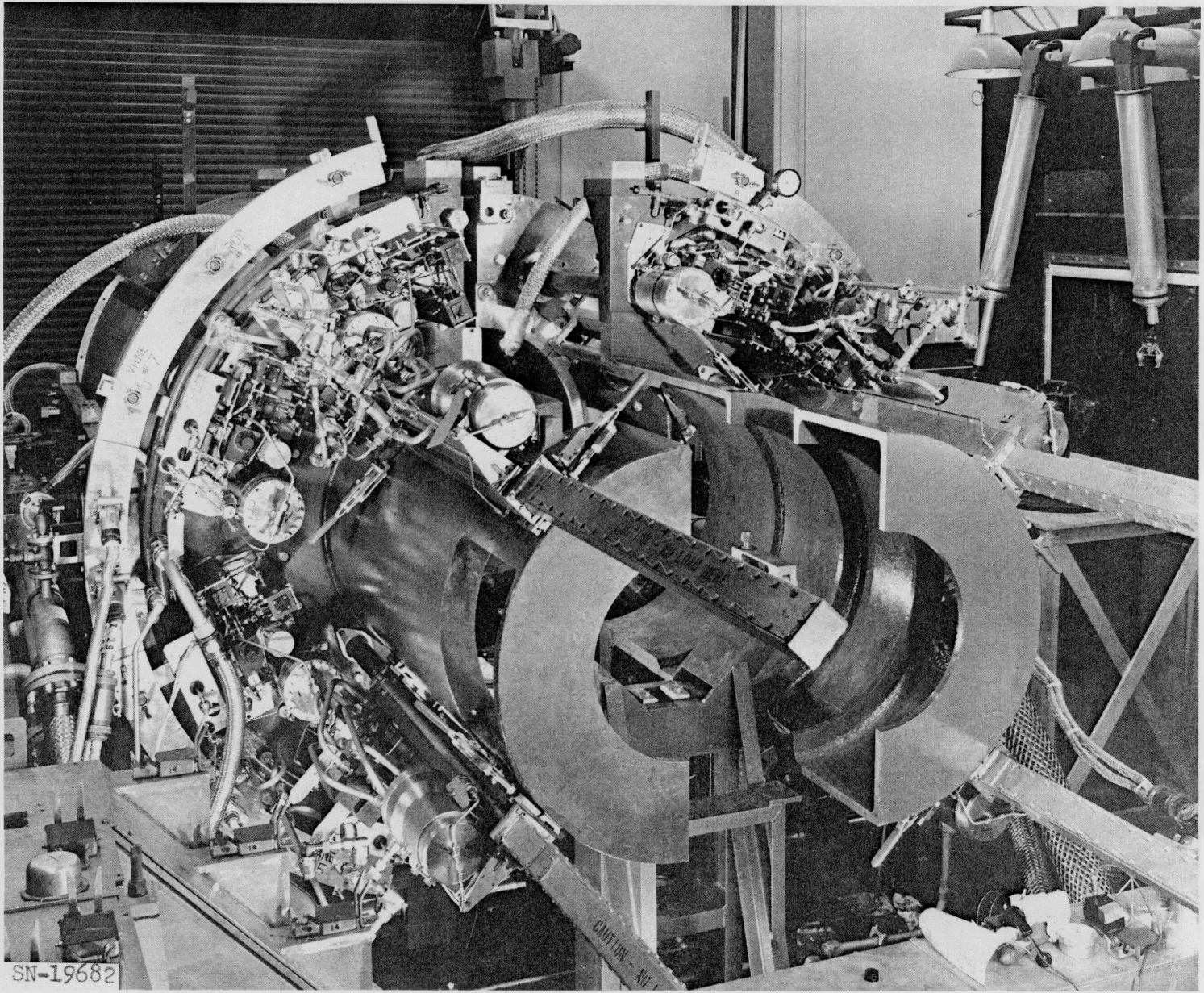

Fig. I-17. View of Tory II-A control element actuation subsystems.

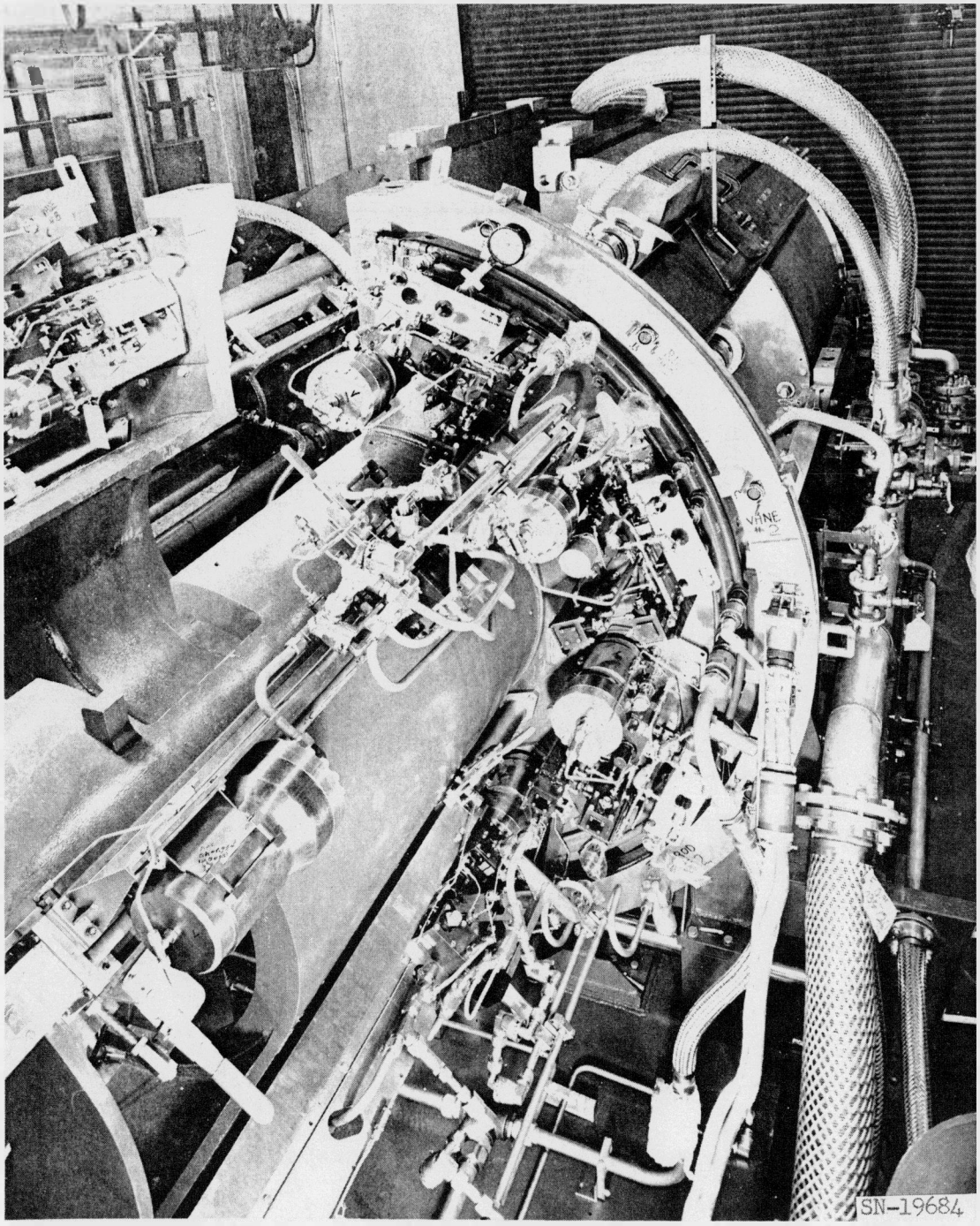

Fig. I-18. View of Tory II-A control element actuation subsystems.

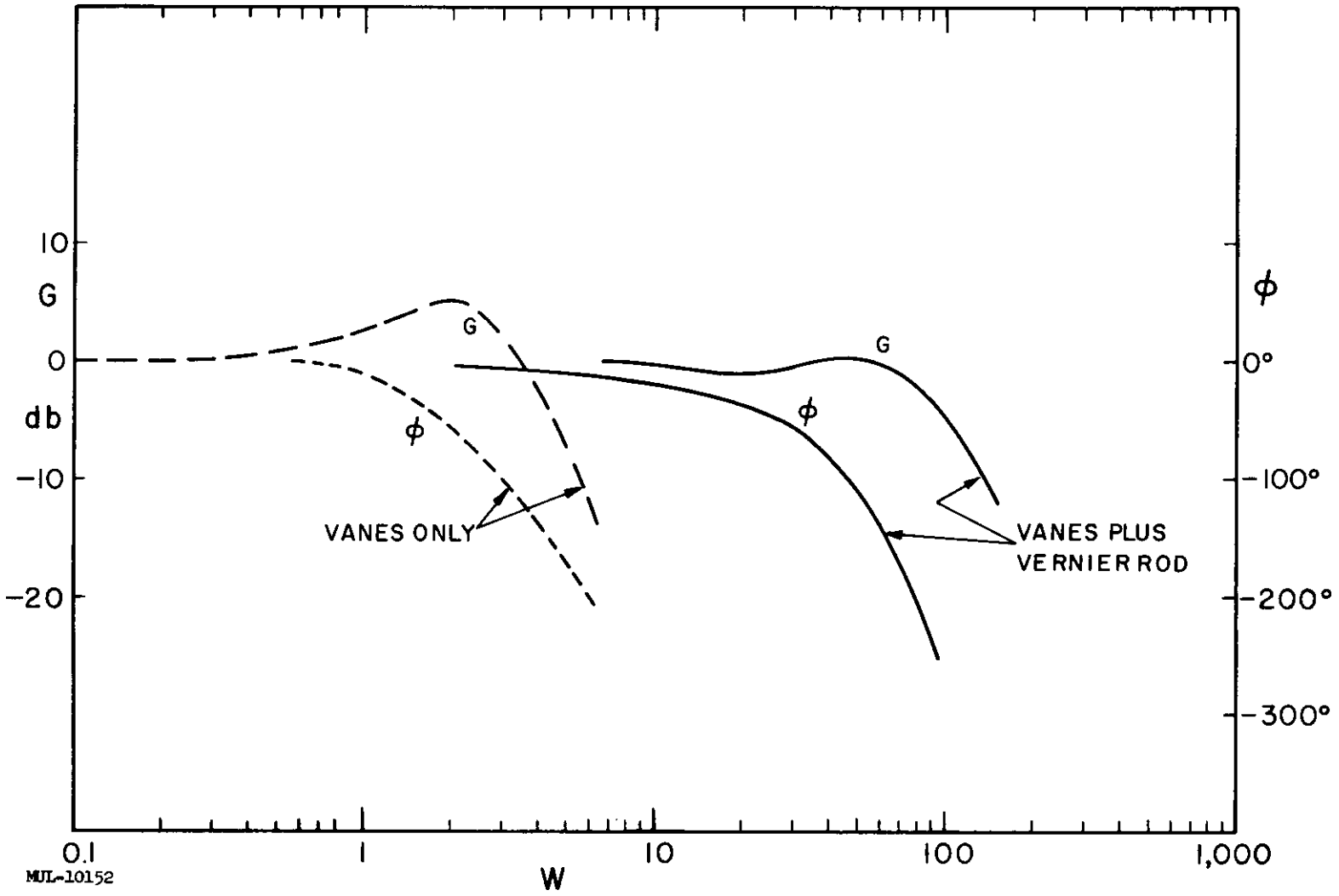

Fig. I-19. Closed loop response of the power control system, P_{out}/P_{demand}.

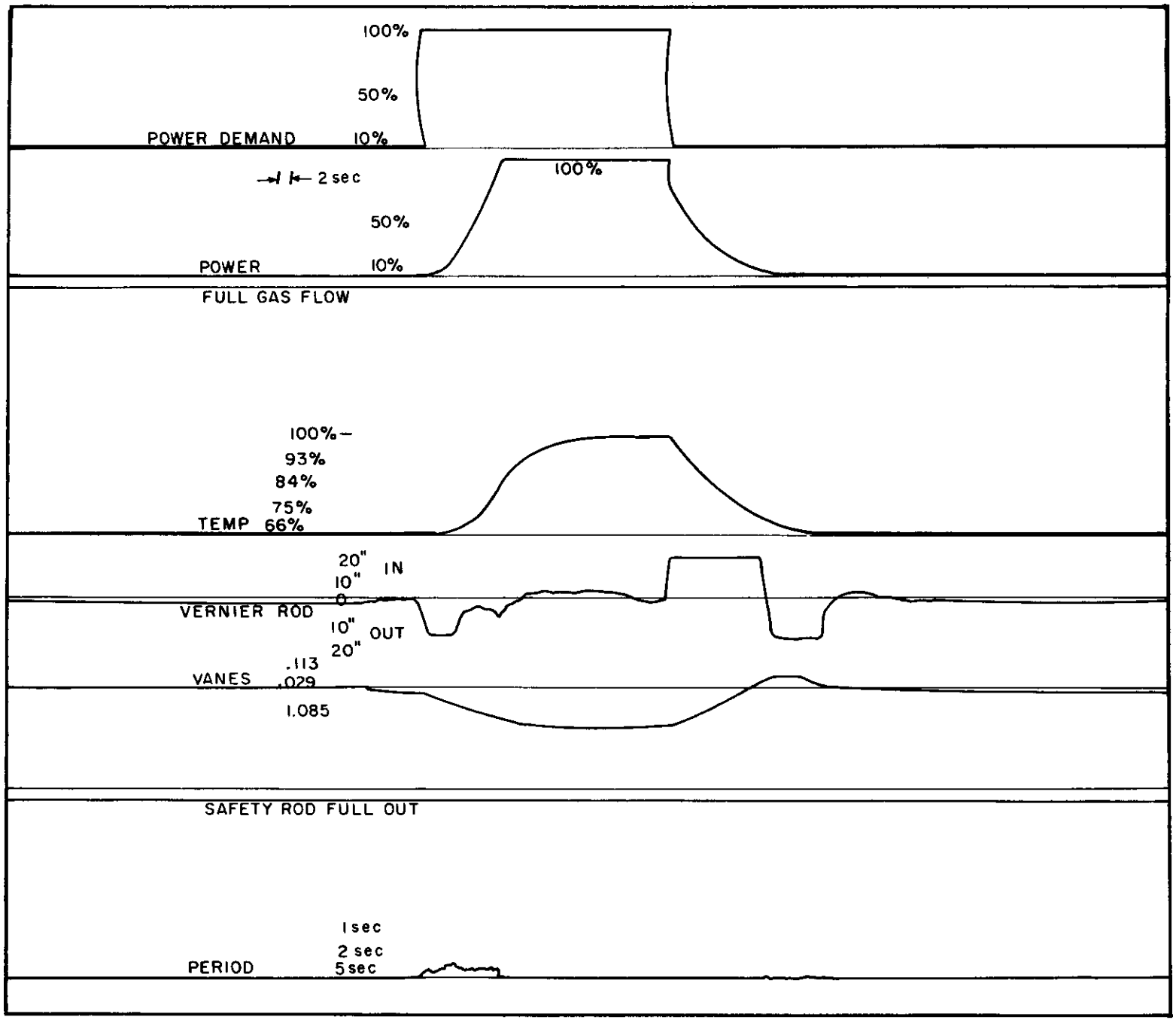

MUL-10153

Fig. I-20. Response of power control system to ± 90% P_o steps of power demands.

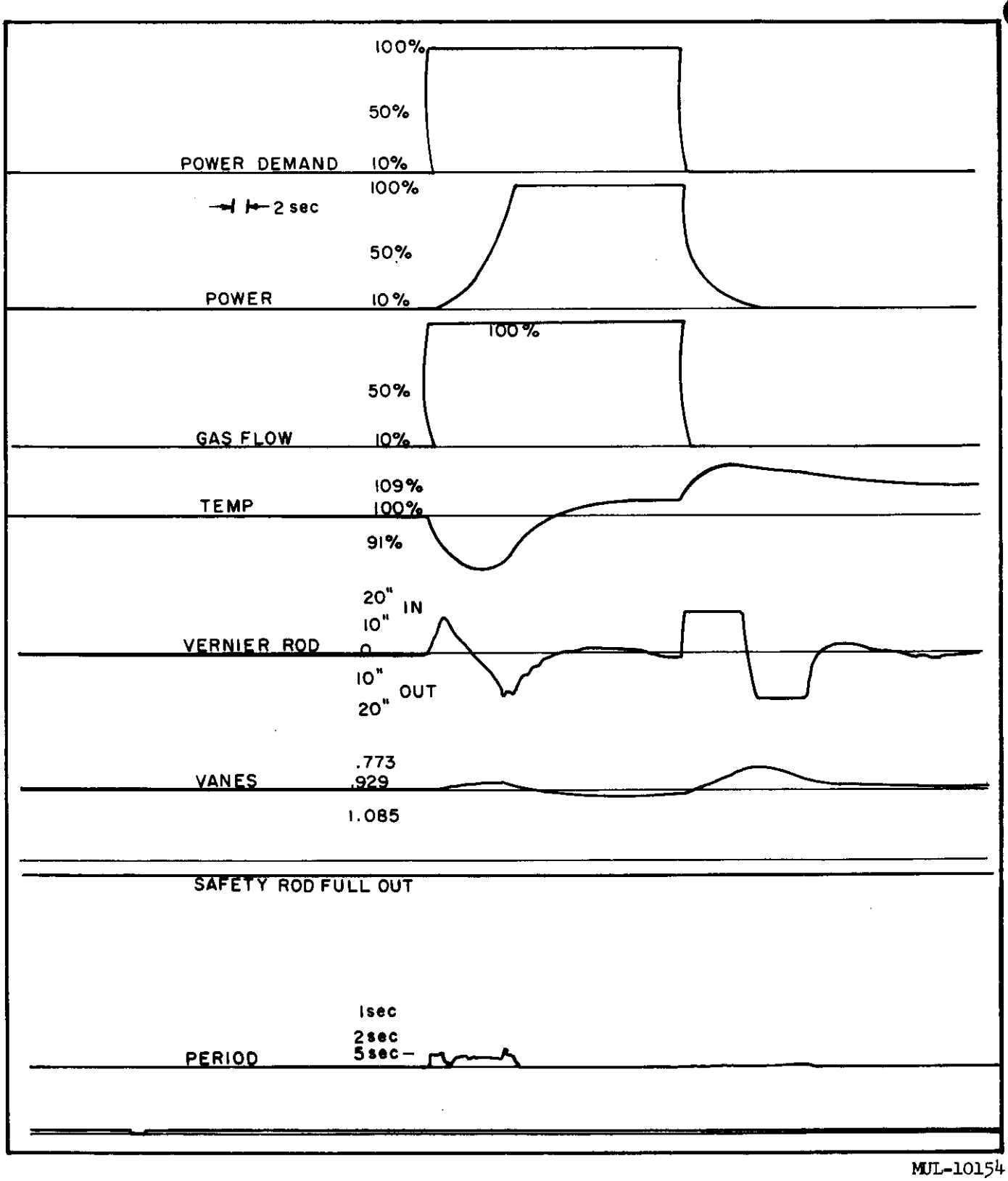

Fig. I-21. Response of power control system to ± 90% P_o steps of power demand and reactor air flow rate.

transient demands which can be envisioned for this system and, as seen, the system takes power to its final value in a stable manner.

Figure I-22 shows the response of the power control system to a typical Tory II-A program of power and air flow rate where the power is varied from 10% P_o to P_o in 60 seconds.

Figure I-23 shows the system to ± $1.00 steps of reactivity using the fast reset mode. Recovery to this accident situation was so fast that a scram did not occur.

Figure I-24 shows the response of the power control system to a ±90% P_o ramp when using "vanes-only," i.e., assuming the vernier rod was inoperative. As seen, there exists a limit cycle oscillation. This oscillation is caused by the finite resolution of the vane actuation systems, as can be shown by improving the vane resolution or raising the overall system gain. One can alternately calculate the limit cycle amplitude and frequency using nonlinear describing function analysis, and the value obtained compares closely to the observed value (within 50%). The limiting factor in getting good vane resolution was found to be the potentiometer used for feedback and indication. In Stage V this same potentiometer was used to give vane reactivity, since reactivity was assumed proportional to vane position. The potentiometers were found to have resolution ± 0.1% of full displacement (180°) or ± 0.18°. When considering 8 vanes, the resolution of the "vane-only" system is found to be approximately ± 15¢ reactivity which explains the rather large power control system "hunting."

To minimize the limit cycle amplitude, an improved potentiometer is being purchased for use with the vane system. This potentiometer has a resolution of 0.025%, so it should reduce the amplitude of the limit cycle by at least a factor of four. As seen in previous figures, use of the vernier rod eliminates the limit cycle entirely.

Figure I-25 shows the system response following an operator initiated scram. As seen, the power is dropped to 20% P_o in approximately 0.3 seconds after which the delayed neutrons slow down the power level shutdown rate.

During the Stage V checkout, approximately 25-30 hours of operation were accumulated on the entire system, with much longer operating times accumulated on the electronics chassis.

During the system checkout in Stages II-V, some 500 hours of running time was accumulated on the Tory II-A electronic chassis without any malfunctions or failures.

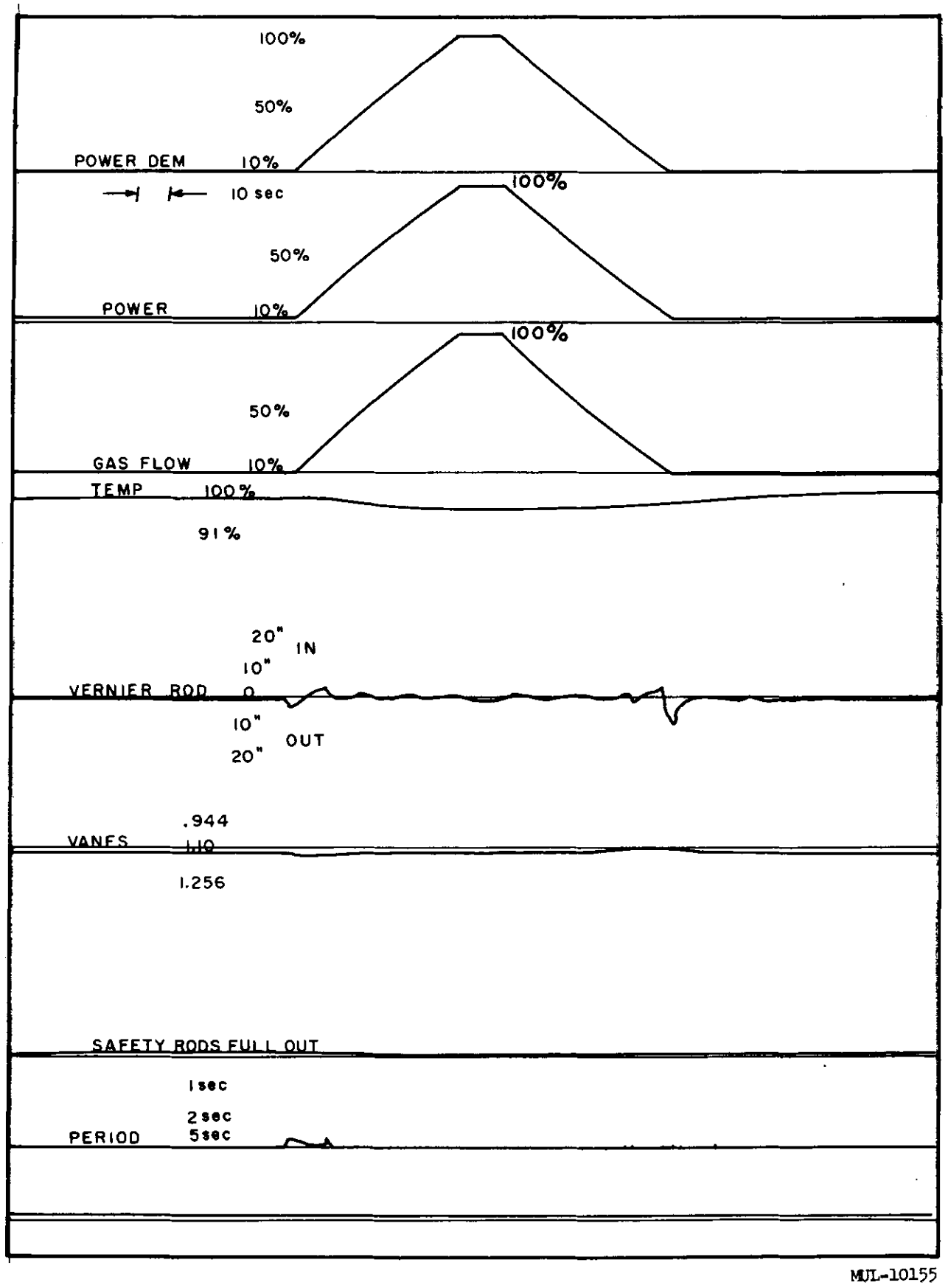

Fig. I-22. Response of power control system to ± 90% P_o ramps change in demand power (60 second slope).

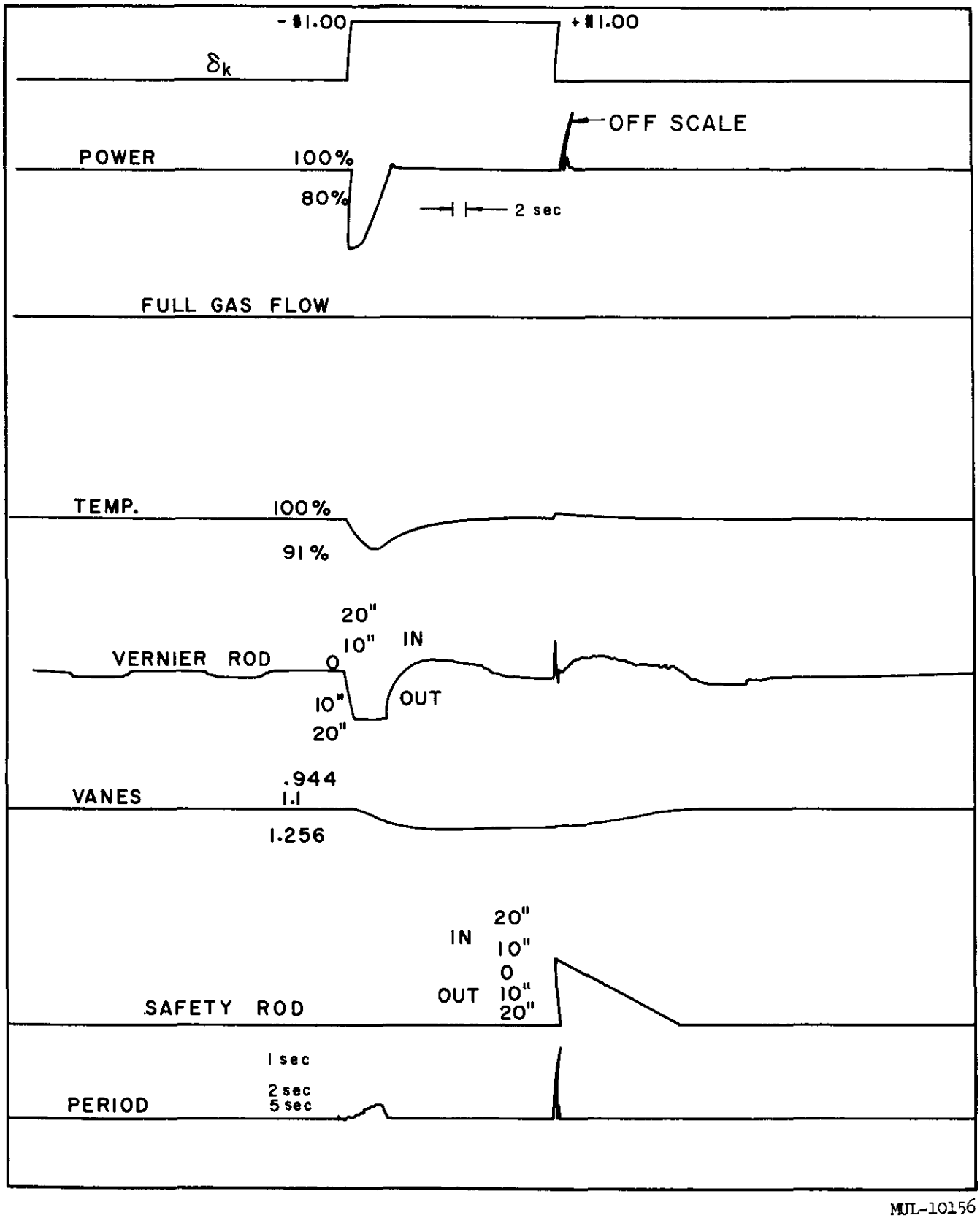

Fig. I-23. Power control system recovery to ± $1.00 steps of reactivity.

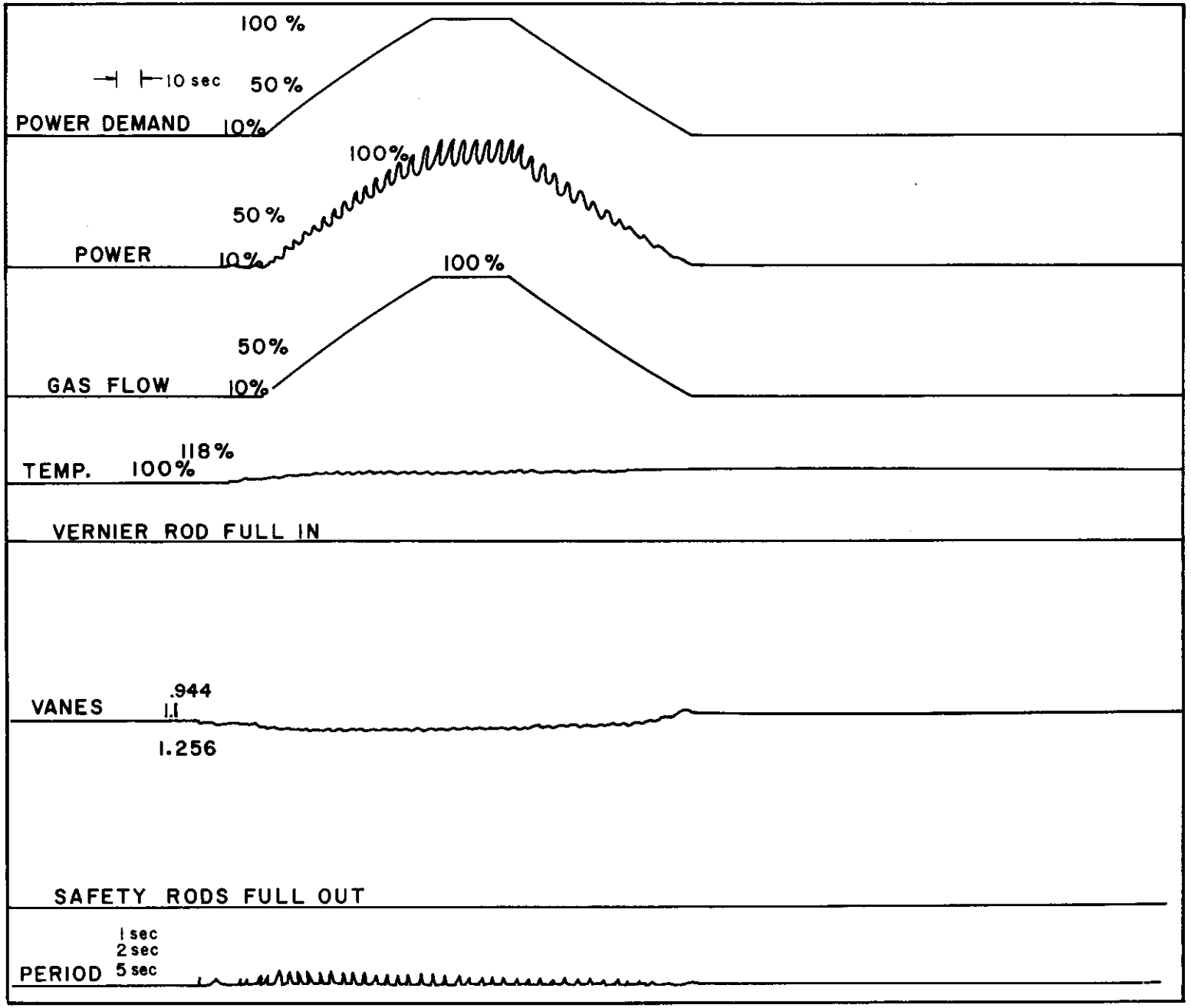

MJL-10157

Fig. I-24. Response of the power control system to ± 90% ramp changes in power when using "vanes-only" (i.e., no vernier rod).

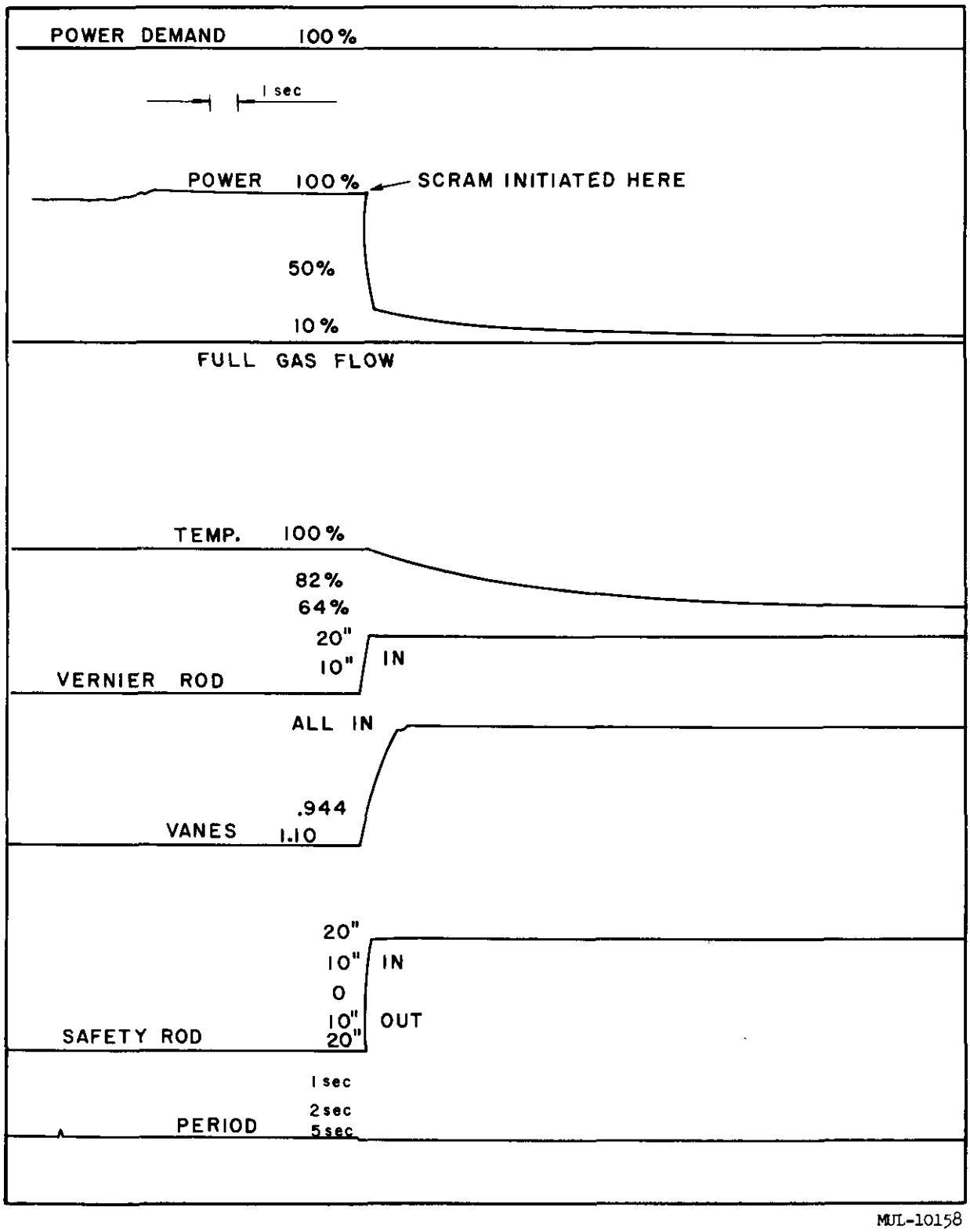

Fig. I-25. Response at system to operation initiated scram.

SECTION IV. ENGINEERING

Base Plate Testing

To date 13 hot flow tests have been made on various 0.5% Ti-Moly coated plates utilizing the Marquardt Corporation hydrogen burner facility which yields flow containing about 13% oxygen by weight at 2000°F. These tests were a continuation of the series of hot flow tests conducted on base plate materials. In this series the plates were of Tory II-A configuration and were considered to be of better material than those in the previous tests.

The "H-7" plate had slightly chamfered edges on the holes. The plate after W-2 coating at 2000°F had successive layers of molybdenum and Rokide applied to a sand-blasted surface. The "H-4" plate had a 1/16-in. radius on the holes. The W-2 was applied at 2000°F and one surface of the plate had a Rokide coat applied with no preparation of the surface. The "H-5" plate also had radii and had a W-2 coat applied at 2450°F. On one surface a Rokide coat was applied with no surface preparation.

The results of the tests appear in Table I-7. The kentanium plate was used as a checkout part. Figures I-26 through I-28 show the plates after testing.

Preliminary conclusions to be drawn from this series of tests are: Upon comparison with earlier data it is evident that

(1) Increasing the hole corner radius has noticeably increased average time-to-coating failure.

(2) A Rokide coat applied to a smooth W-2 surface has a tendency to spall; however, surface preparation and moly coating seems to improve the plate lifetime.

Table I-7. Saugus Base Plate Testing Summary

Run No.	Plate No.	Face	Sector	Coating or Material	Run Conditions	Results
1	H-1	Front	6	Kentanium	3 min at 2000°F	One major crack from hub to opposite hub but not cracked out to external surface
2	H-7	"	"	W-2 applied at 2000°F Rokide and Mo applied over sandblast W-2 surface	Same	Good (Cooper plate)

(continued)

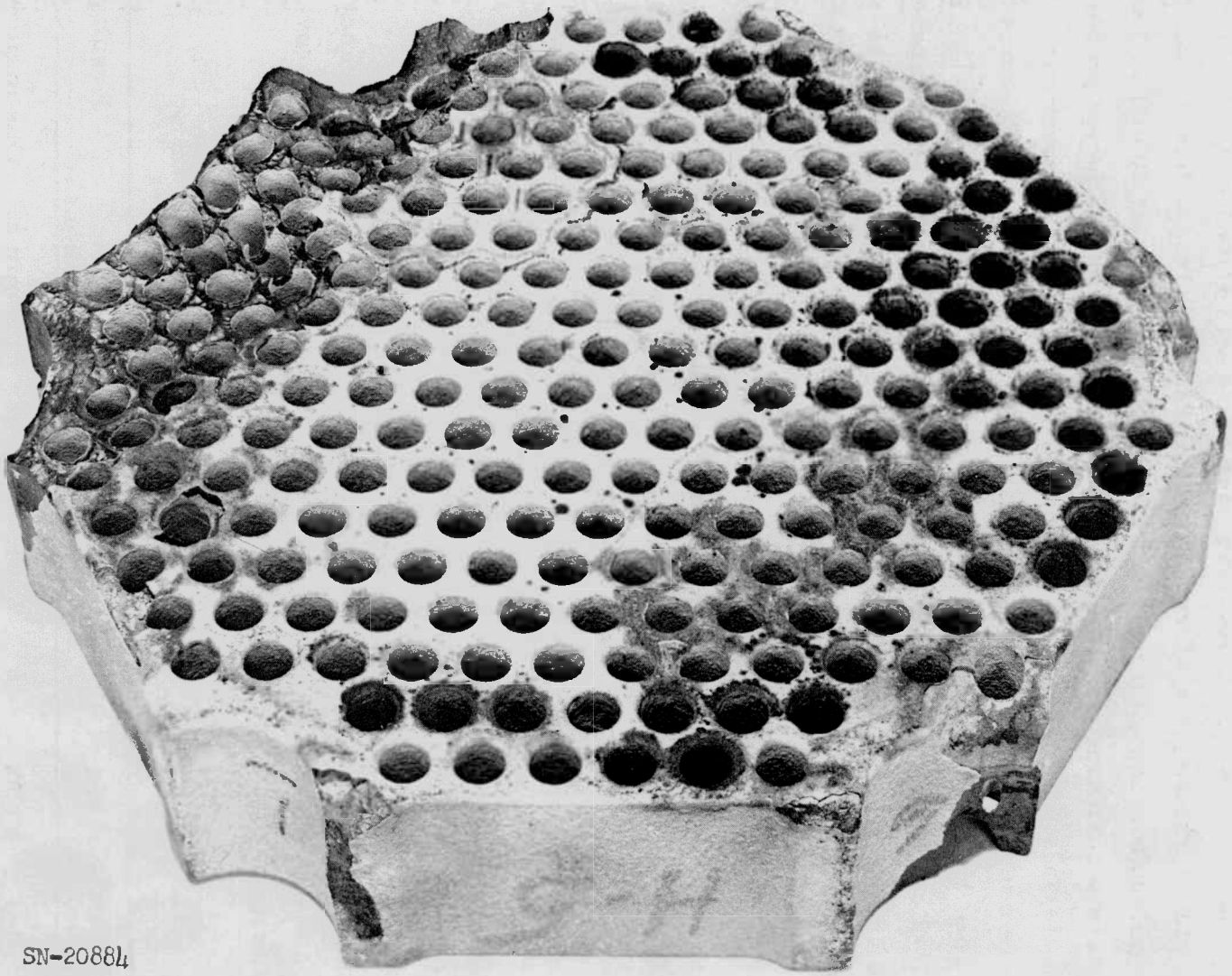

Fig. I-26. Test 142. Specimen H-5, front view after test.

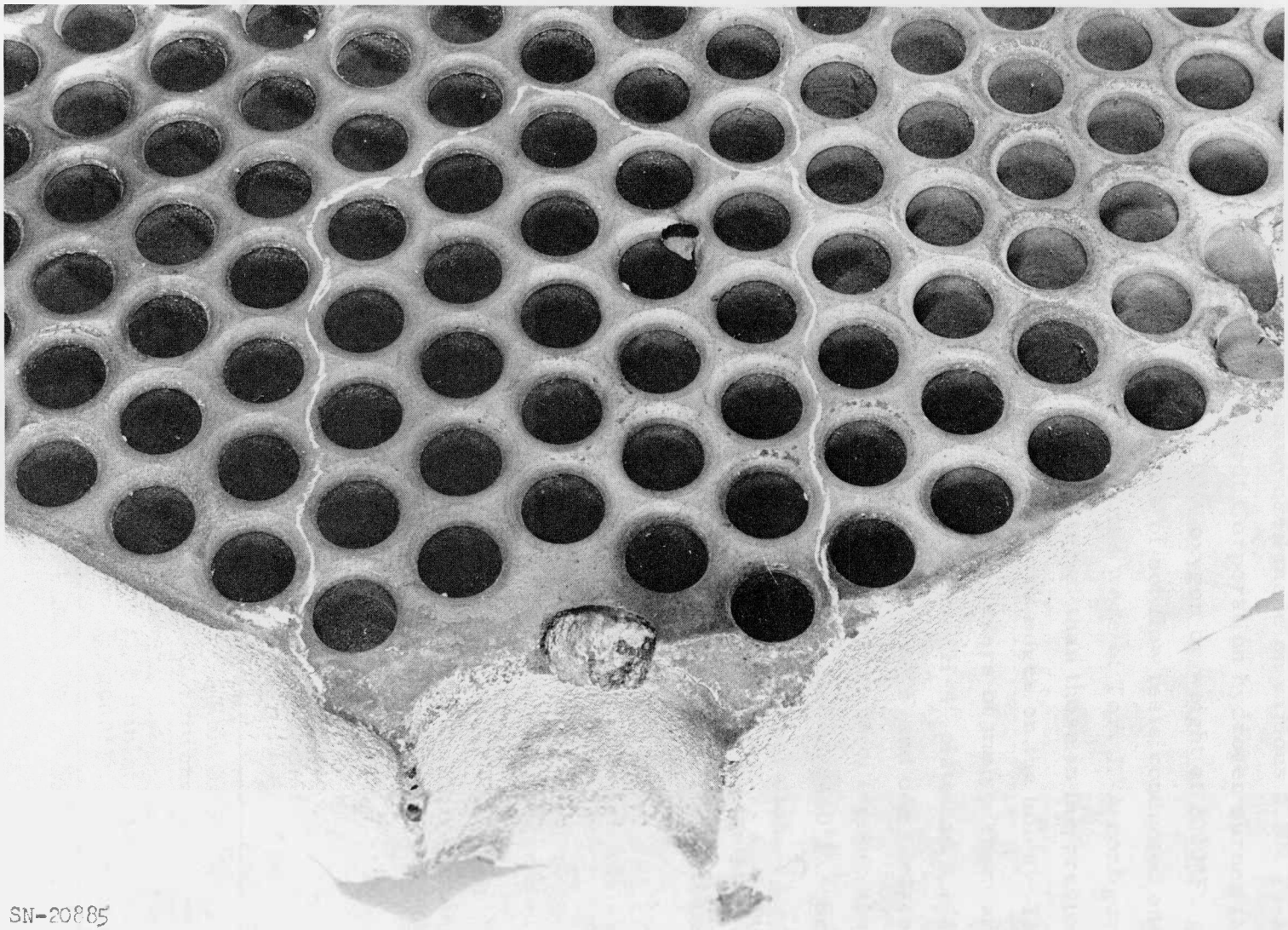

Fig. I-27. Test 142. Specimen H-5, Sector 5, rear, after 18 minutes.

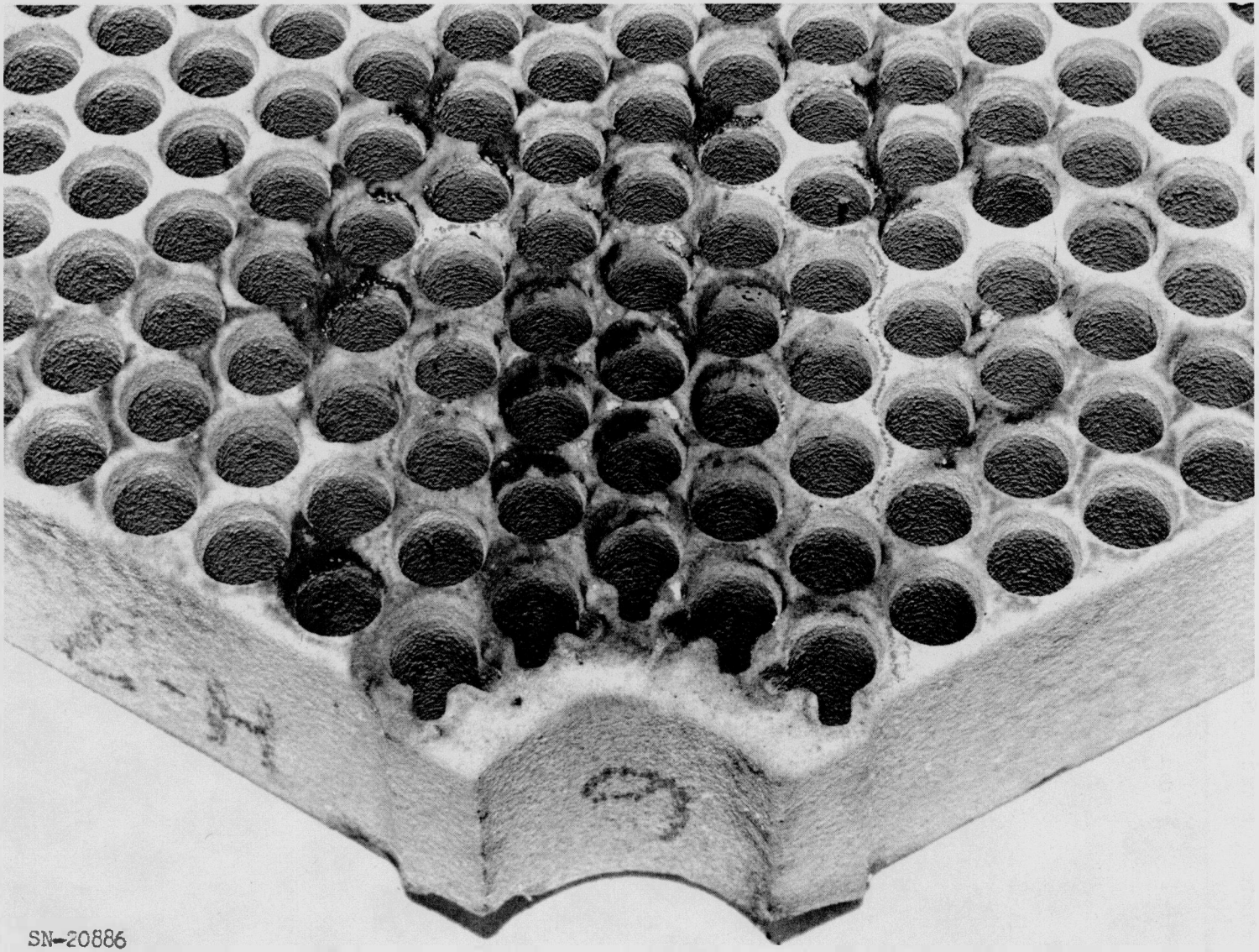

Fig. I-28. Test 142. Specimen H-7, Sector 6, front, after 18 minutes.

Table I-7. Saugus Base Plate Testing Summary (continued)

Run No.	Plate No.	Face	Sector	Coating or Material	Run Conditions	Results
3	H-1	Front	6	Kentanium	30 min at 2000°F	Continued cracking at random — previous crack continued to outside surface
4	H-7	"	"	W-2 applied at 2000°F Rokide and Mo applied over sandblast W-2 surface	15 min at 2000°F	Good — surface is discolored (Cooper plate)
5	H-4	"	"	W-2 applied at 2000°F and Rokide	3 min at 2000°F	Poor — oxidized at 2 places, Rokide chipped at 2 spots
6	H-5	"	"	W-2 applied at 2450°F and Rokide	Same	Good
7	H-5	"	"	Same	15 min at 2000°F	Oxidized one place under Rokide pin hole
8	H-5	Rear	"	W-2 applied at 2450°F	3 min at 2000°F	Oxidized on outside edges
9	H-5	"	5	Same	Same	Good
10	H-5	"	"	Same	15 min at 2000°F	Oxidized at one point
11	H-5	Front	3	W-2 applied at 2450°F and Rokide	3 min at 2000°F	Good
12	H-5	"	"	Same	15 min at 2000°F	Bad oxidation, 1/8 to 3/16 in. of erosion on 1/2 of flow face and adjacent area to next hub in one direction
14	H-4	Rear	4	W-2 applied at 2000°F	3 min at 2000°F	Good
15	H-4	"	"	Same	15 min at 2000°F	Oxidized at one point

Short Module Acoustic Fatigue Test

Following inspection and repair of the short module subsequent to the damping evaluation it was subjected to a high energy sound level to determine the structural integrity of the beryllia components in a noise environment believed to approximate the actual reactor.

The acoustic fatigue test was conducted at the Marquardt Jet Laboratory, Van Nuys, California, and was completed on April 7, 1960. The test item, as shown in Fig. I-29, was placed inside of two plastic bags. The sound attenuation of the two plastic bags was measured at random sound levels at LRL and the results are presented on Table I-8. This entire assembly was installed inside the silencer house of the jet engines utilized as heat exchangers at Marquardt.

Table I-8. Sound Attenuation of Double Plastic Bags

Random Sound	Decibel Level Outside Bags	Decibel Level Inside Bags
A	80	79
B	69	68
C	57	56

During the warmup period of the engines, the recorded sound level within the plastic bags varied between 118 and 124 decibels, and between 130 and 133 decibels during running operations. The total time accumulated was 12.2 hours at 118 to 124 decibels and 16.3 hours at 130 to 133 decibels. The frequency range versus the decibel sound level is presented on Fig. I-30. The reference sound intensity is the standard 1 microwatt/cm^2.

Upon completion of the test sufficient dust had accumulated in the bottom of the inner bag to be readily visible to the unaided eye. The dust particles ranged in size up to approximately 0.05 in. in diameter. The contamination levels were well below tolerance outside the bags. The module was then shipped back to LRL for disassembly and inspection. There were no broken or chipped parts visually observed on disassembly. A sample lot of 20-tube elements was inspected with Zyglo equipment. The Zyglo results were good and are listed on Table I-9. One factor which may result in the tests being overly severe is that pressure forces tending to restrain the tubular element exist in the reactor, whereas they do not here.

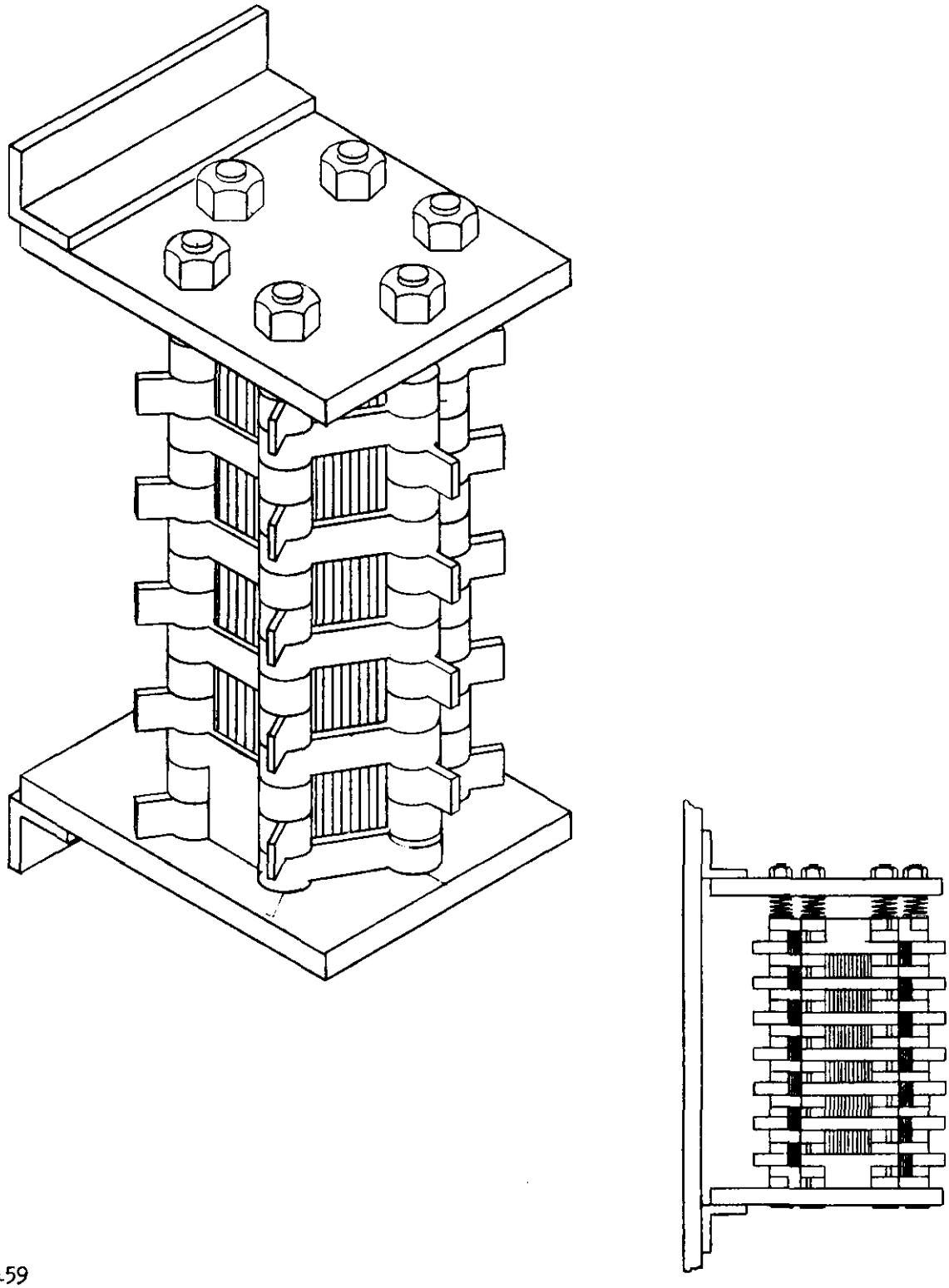

MUL-10159

Fig. I-29. Short module assembly.

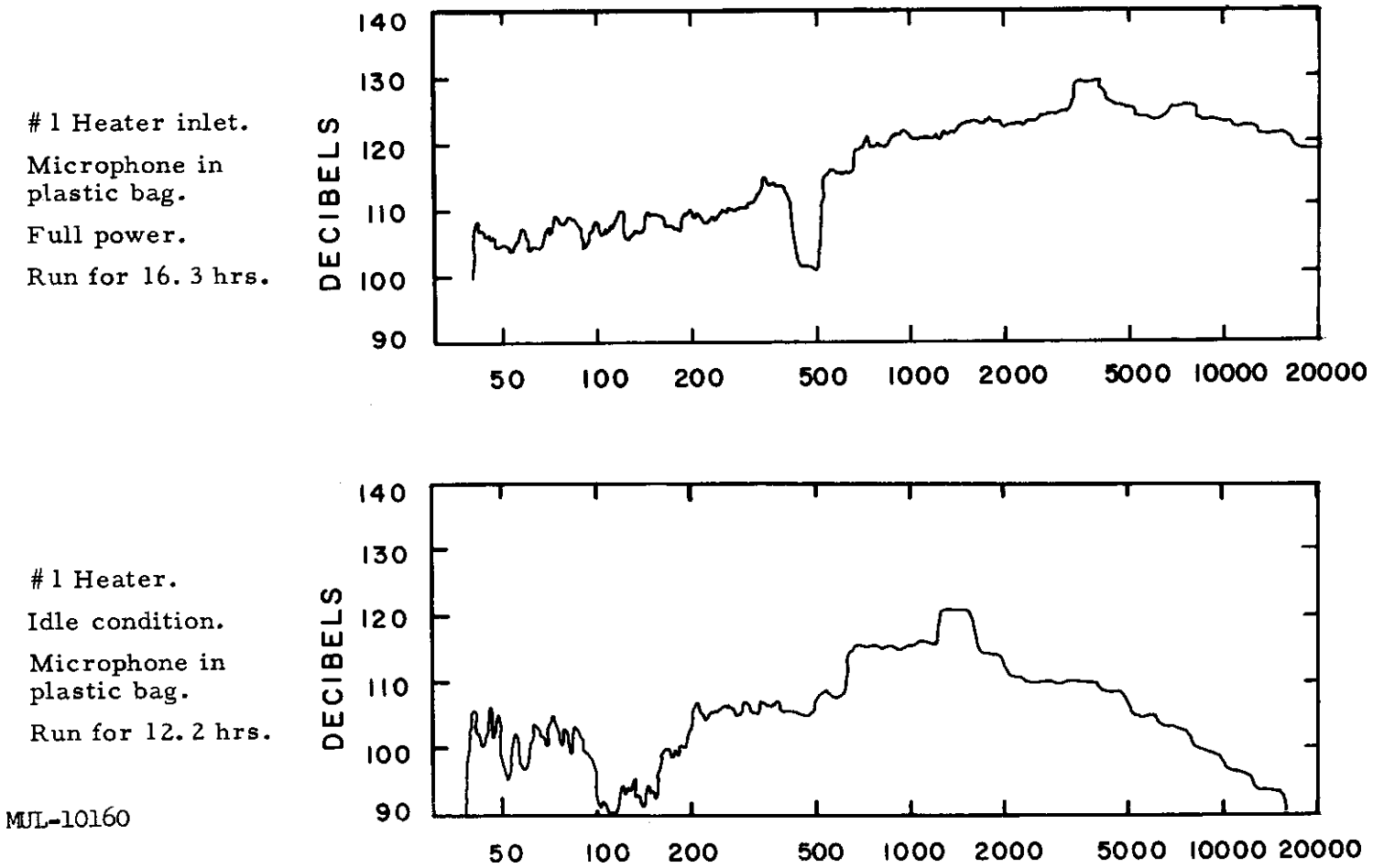

Fig. I-30. Ceramic element fatigue test spectrum analysis.

A full-length core module assembly was fabricated for test evaluation at low, or ambient temperatures. This assembly is designated as the cold flow module, and was evaluated at the Marquardt Research Field Laboratory.

One of the most significant results of the test is the value of the tube friction coefficient. Two exit nozzle configurations were employed to give two different tube exit Mach numbers. The data is plotted on Fig. I-31 and shows little difference with exit Mach numbers. It is obvious from this data that the tubes are anything but comparable to smooth pipes, exceeding smooth pipe values by a factor of 2.5.

Table I-9. Zyglo Results on 20-Tube Sample After Test Completion

Tube	Results	Quality
1 to 15	Uncracked	Acceptable
16	4 small longitudinal cracks	Acceptable
17	4 small longitudinal cracks, 1/16"	Acceptable
18	2 transverse cracks, 1/16"	Marginally acceptable
19	1 transverse crack, 1/16"	Acceptable
20	1 end crack	Acceptable

Inspection of Prototype Cantilever Shroud – Tory II-A1

Following the load-deflection tests at temperature and the hydrostatic test the shroud was delivered for a post-mortem inspection by nondestructive methods. Conventional radiographic, penetrant, and resonance ultrasonic methods were used. Also a proprietary oil was tried as a method to locate spot-weld nuggets that were not holding.

The conventional methods revealed three cracks up to 1.5 in. long in the base metal. The majority of the spot welds were cracked also. The seam welds were reasonably good though there was some minor cracking and some porosity. Resonance ultrasound showed the sheet to be uniform within 0.002 in. which is well within tolerance for sheet stock.

There is one important question regarding an array of spot welds that is not answered by any of the existing methods of inspection. Are all of the weld nuggets fused to the two sections? The only method that appeared feasible was to detect the existence of heat sinks resulting from good welds, and

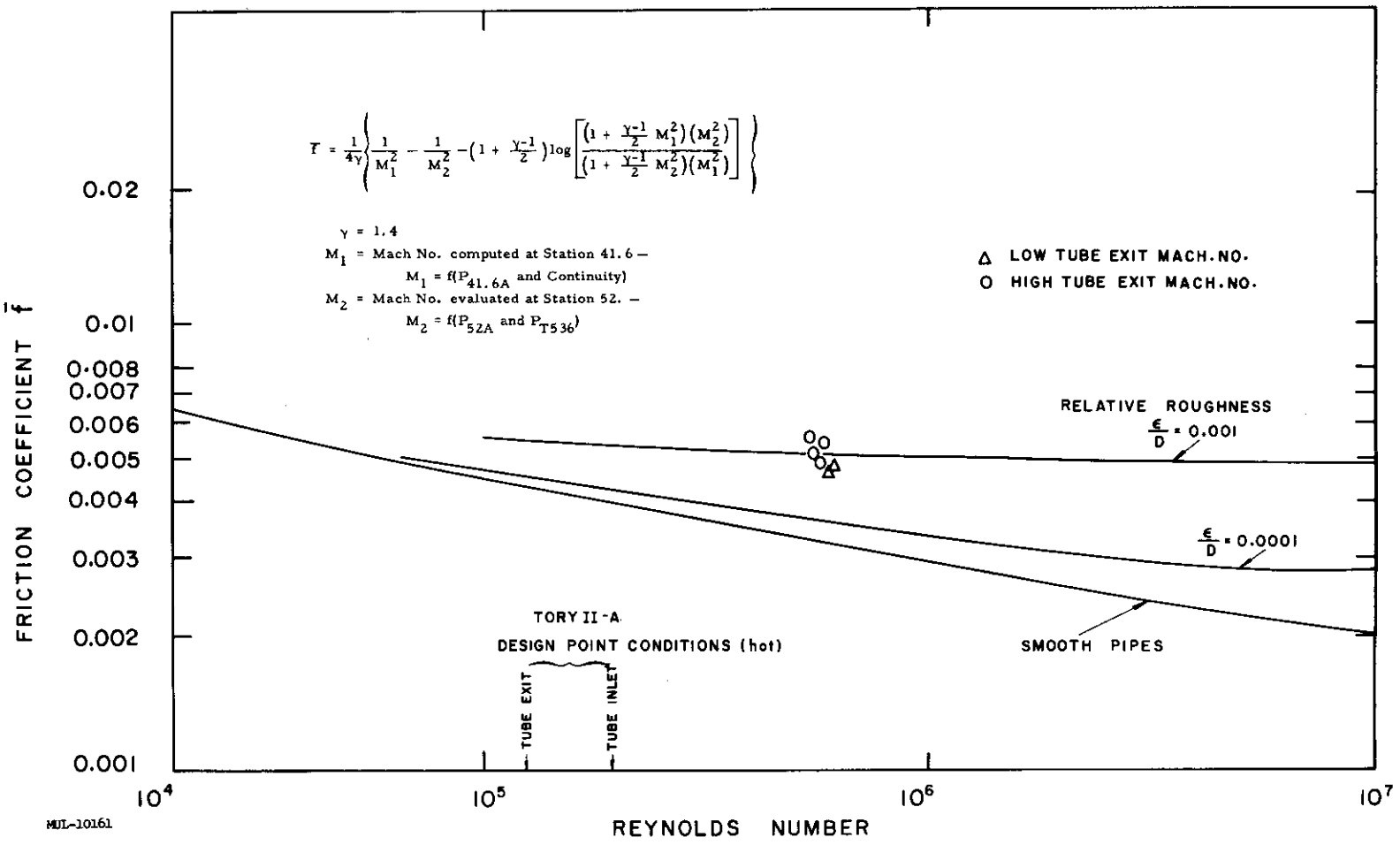

Fig. I-31. Tory II-A cold flow module friction factors.

conversely the absence of such sinks if the nugget is not bonded to both sections. An oil that has a sharp change in surface tension as a function of temperature was used so that if a thermal gradient is established in the plane of the surface being inspected the oil flows to the cool end of the gradient. When a thin coating of this oil is applied to the surface to be inspected, and that surface is heated in a transient manner, the oil collects over the good spot welds and flows away from the spot welds which are not bonded to the back layer. Application of this inspection method to the shroud revealed that about half of the plug welds were unbonded. This was confirmed by quasi-destructive methods. All of the resistance spot welds on the inner sheet appeared to be bonded.

Sections were marked for samples to confirm the findings of the several tests and to furnish tensile test specimens to evaluate weld efficiency. Resistance spot welds are being employed in the fabrication of the Tory II-A1 shroud.

Tory II-A Vibration Mockup

An attempt to simulate the core dynamic components has been made. The system, responsive to lateral driving forces contained the following components:

(1) Ten solid rods 0.19 in. diam connected by aluminum slots dogbone fashion, and containing hexagonal steatite tubes.

(2) Springs connecting the end of the rod assembly with the simulated shroud.

(3) A thin-wall cylinder (shroud).

(4) Corrugated snubbers between the shroud and a heavy outer container.

The model in Fig. I-32 was vibrated at various driving forces from 6 to 300 cycles per second. Results of this test at 2 g is shown in Fig. I-33.

Short Module Damping Evaluation

A short module, 12 in. in length, was fabricated utilizing components simulating the Tory II-A parts in material and size (i.e., beryllia tubes and dogbones, (outmoded) molybdenum tie rods and inconel springs). This test item was subjected to a vibration test to determine the inherent damping characteristics of the design.

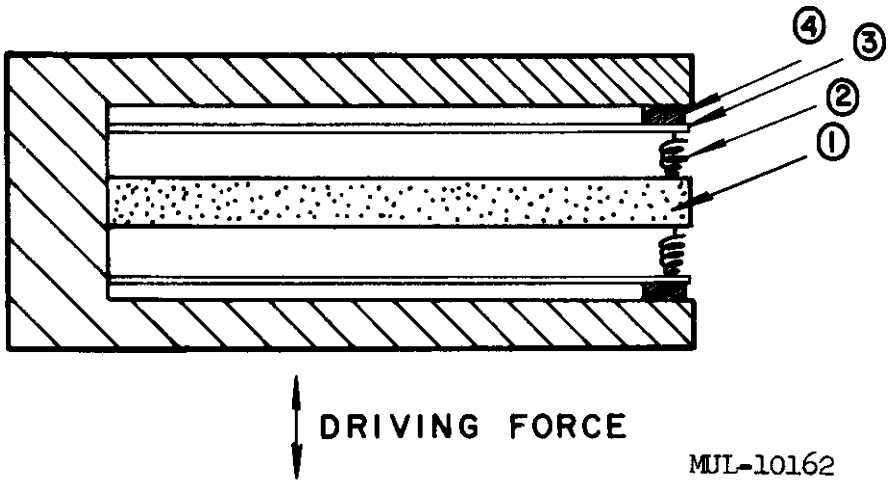

Fig. I-32. The model of the Tory II-A vibration mockup. (See text for numbered components.)

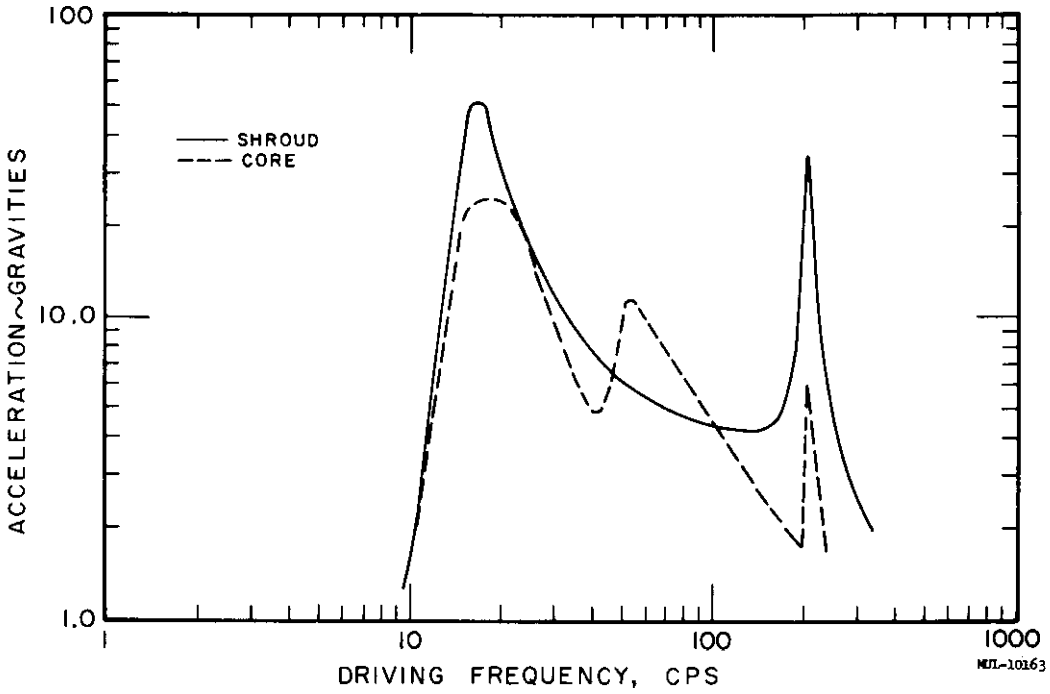

Fig. I-33. Core mockup vibration at 2 g driving force.

The arrangement and geometry of the fuel bearing elements and their housing potentially appeared to have an appreciable damping factor. It was therefore decided to evaluate the damping characteristic of this design. Two test items were employed. The "short module" simulated a core module as described above and as shown in Fig. I-29. A simple solid replacement for the short module known as the "dummy module" was fabricated to evaluate the tare damping of the system. The dummy module is shown on Fig. I-34. The test rig consists of a cantilevered beam which has provisions for varying the length of the beam, and for deflecting and releasing the unsupported end. The beam is mounted in a vertical position and is shown pictorially in Fig. I-35. The short or dummy module was mounted on the free end of the cantilevered beam and the entire assembly was clamped to a rigid I-beam imbedded in a concrete wall of the test building. The initial position utilized one clamp device placed at the top end of the cantilevered beam and determined the minimum frequency of the system. The unsupported end was deflected by tightening the nut on the release arm. After obtaining the proper deflection, the cantilevered beam was released by downward motion of the release arm. After the system came to rest, the second clamp was placed under the first and the test procedure repeated. The lower clamp was moved downward in 6-in. increments for each run.

The natural frequency of the test assembly for various lengths of the beam is shown on Fig. I-36 as calculated by two independent theoretical methods assuming a uniformly loaded cantilevered beam with a concentrated mass at the end. The divergence of the superimposed test data from the calculations at the higher frequencies is due to the inexact assumption of a concentrated mass at the end, when the modules were actually attached at two longitudinal points as shown by Fig. I-35. This assumption is valid at the low frequencies when the beam length is long, but becomes increasingly erroneous as the length is shortened.

The test data indicates that the short module has two basic types of damping, Coulomb or dry frictional, and viscous damping. The Coulomb damping is predominant during the initial portion followed by the viscous damping.

The corresponding run with the dummy module indicated only viscous damping of a very small magnitude. The data from these two runs are reduced and are plotted on Figs. I-37 and I-38. Calculation of the damping

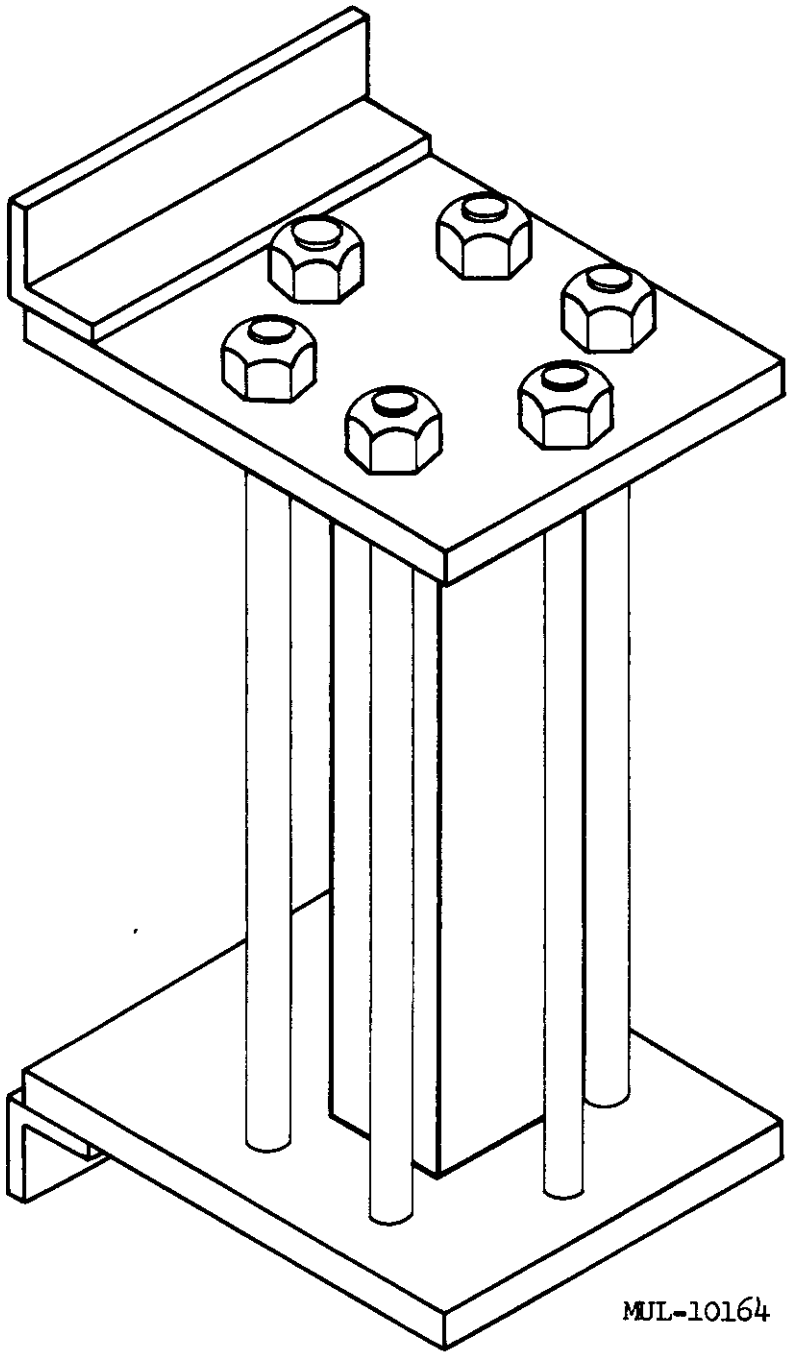

Fig. I-34. Dummy module assembly No. 2.

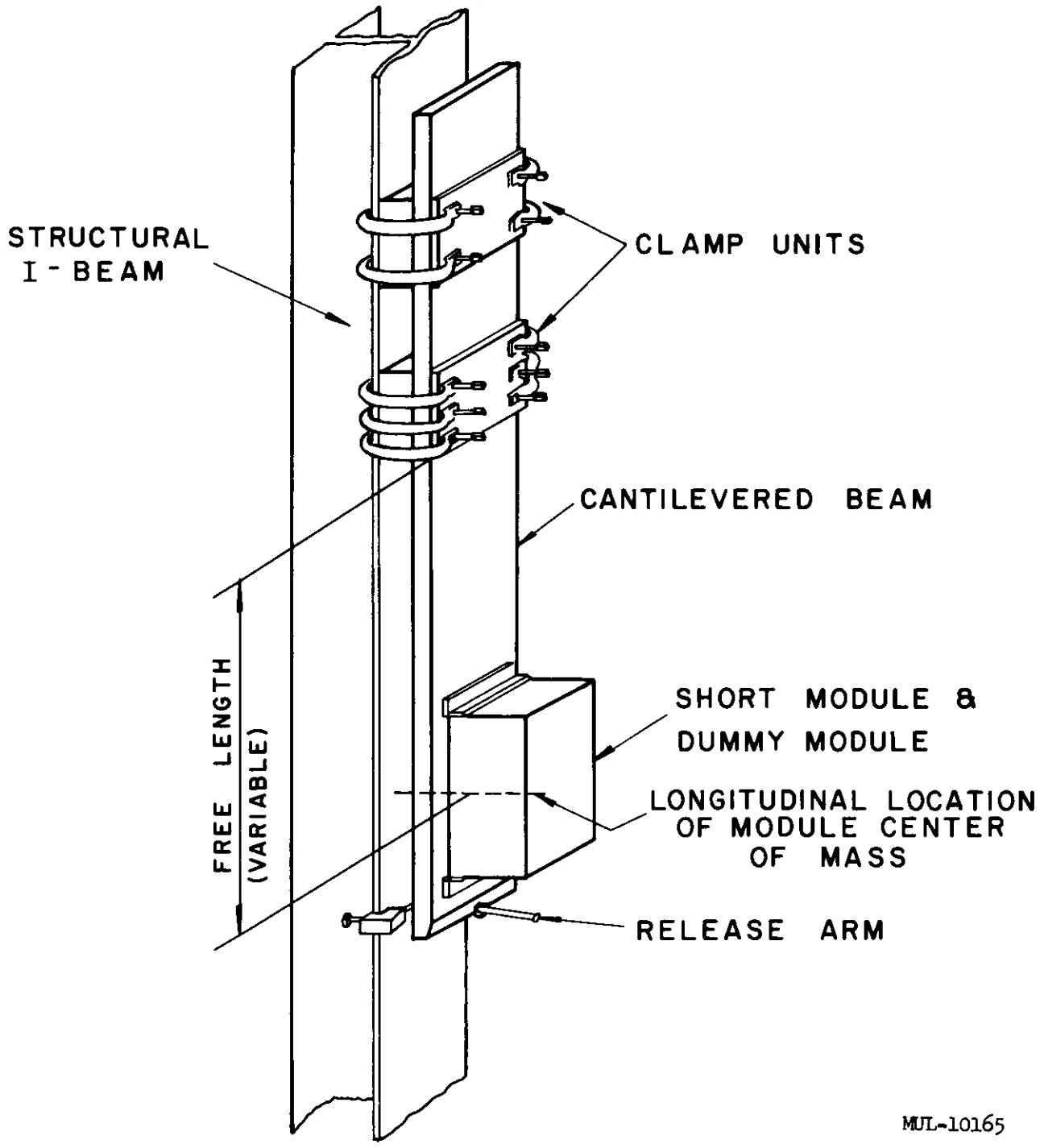

NOT TO SCALE

Fig. I-35. Short module damping evaluation.

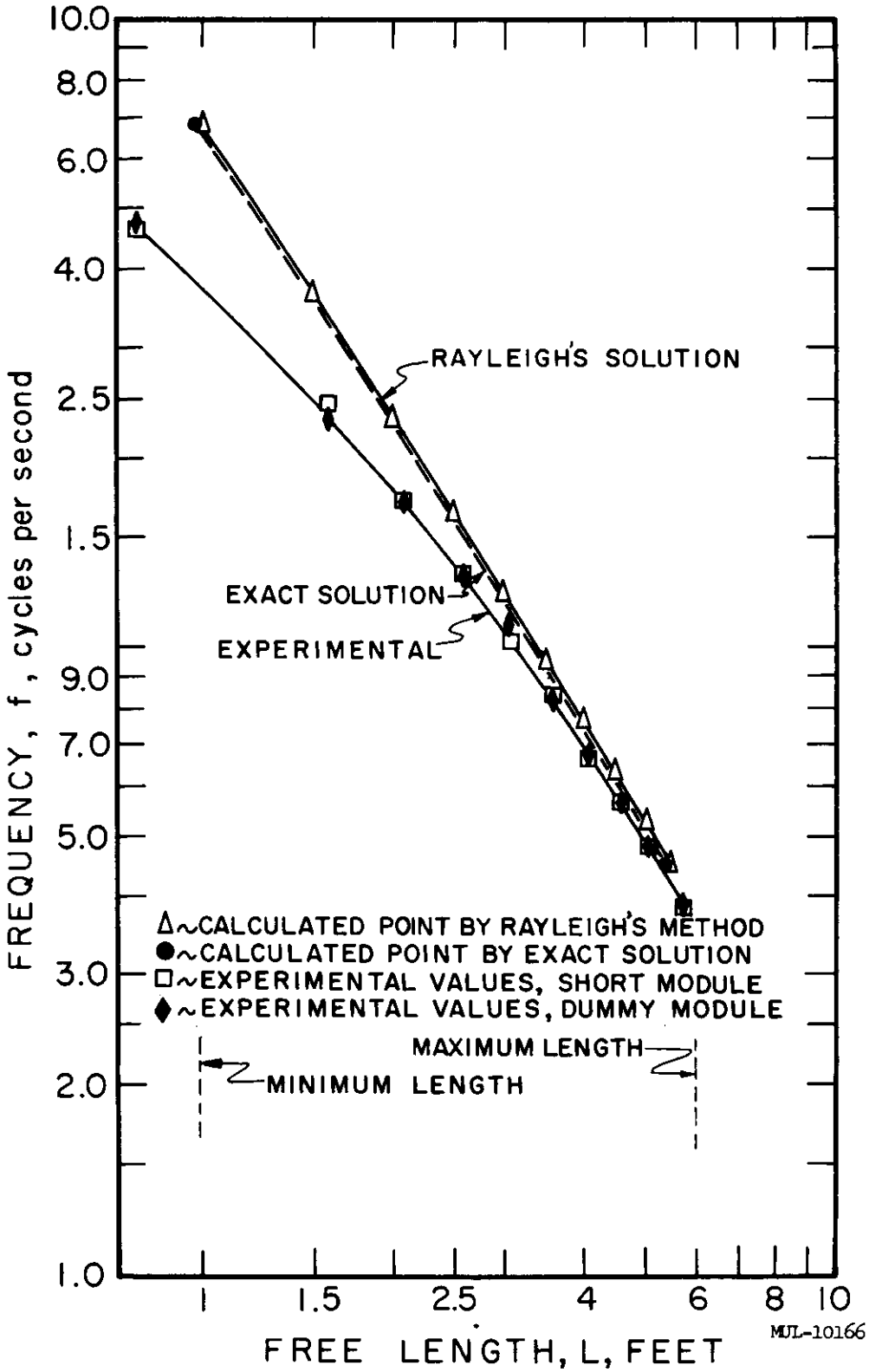

Fig. I-36. Natural frequency of a uniformly loaded cantilevered beam with a concentrated mass at the end.

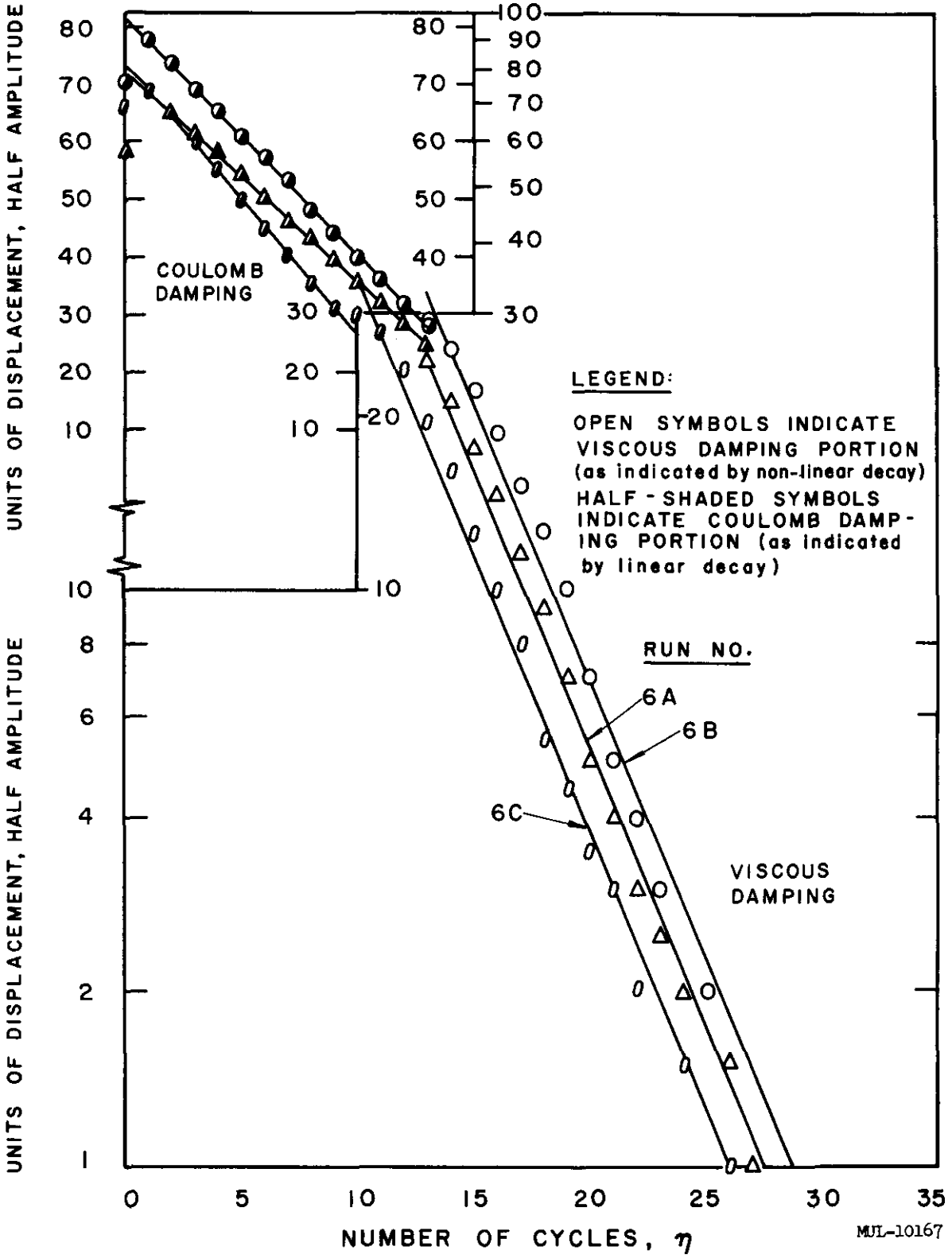

Fig. I-37. Short module amplitude decay run 6 (f ≈ 10 cps).

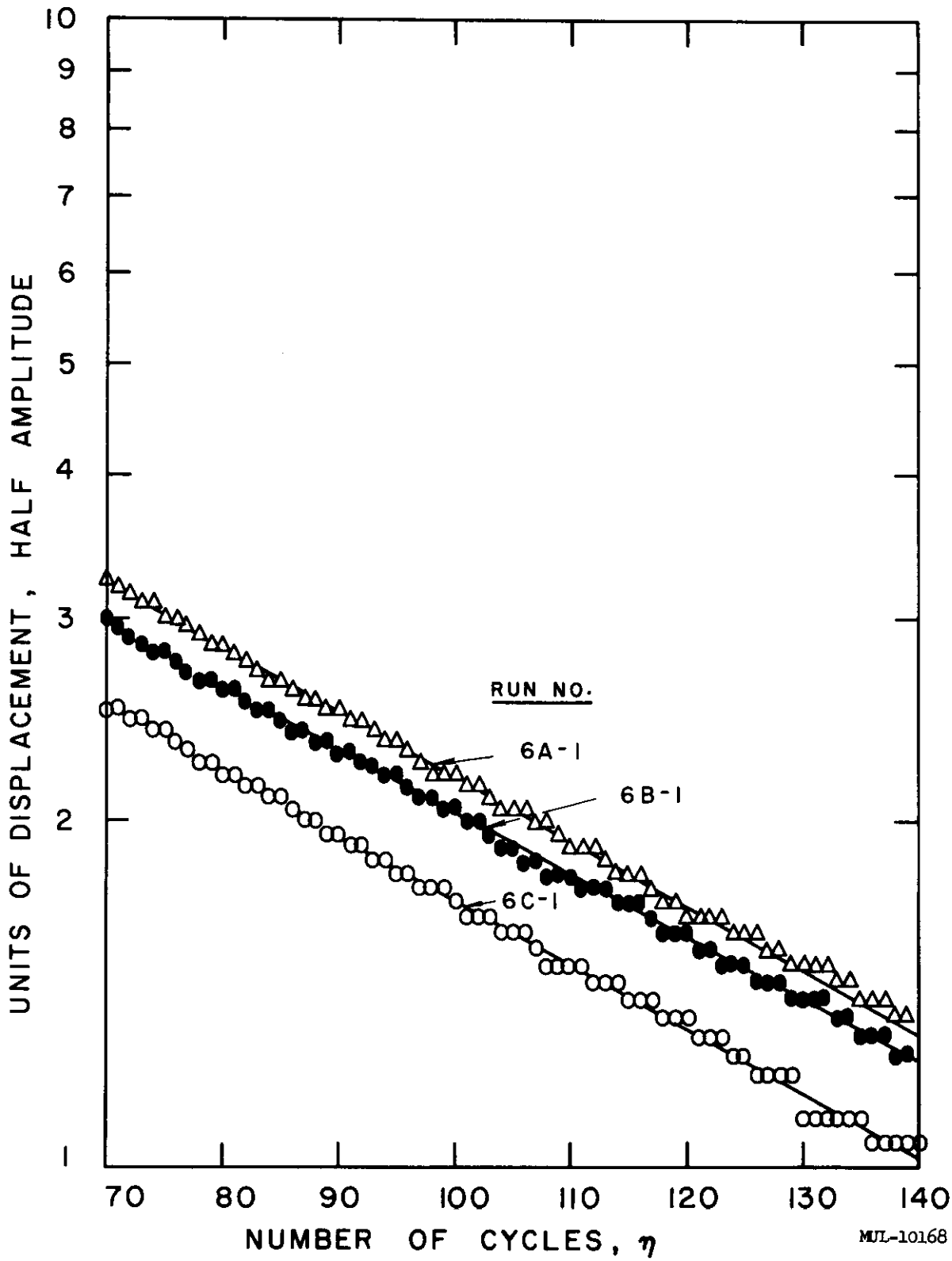

Fig. I-38. Dummy module amplitude decay run 6 (f ≈ 10 cps).

factors is in progress. Of noteworthy interest, however, is the division of Coulomb and viscous damping. Taking the amplitude decay from the initial displacement to 2% of the initial displacement as 100% reduction, Coulomb damping accounts for approximately 2/3 of the energy absorption as presented in Fig. I-39. This is determined by the point at which the decay curve changes from linear to nonlinear (e.g., point A in Fig. I-40). The limit of 2% initial displacement is the limitation of the instrumentation accuracy. Another correlation of the damping division can be made against frequency and time as shown in Fig. I-41.

After completion of the test, the short module was disassembled and all components inspected. Twenty-one of the 988 tube elements had chipped ends. The location of the chipped tubes is shown on the damage map of Fig. I-42. The enclosure had been contaminated with 0.18 micrograms of beryllia dust per cubic meter.

Test Cars

Car No. 1. Assembly of the first car continued through the middle of May. On May 14, after the completion of controls testing, the first reflector was ready for the cold criticality tests. The car, its support stands, carriages, electrical and water cooling system components were shipped to NTS on May 16. Minor modifications of Air Duct Sections were accomplished during April and May. NTS reassembly of the first car is in progress at this time. Figure I-43 shows the completed car at Livermore.

Car No. 2. The second car and second reflector arrived at Livermore on May 13.

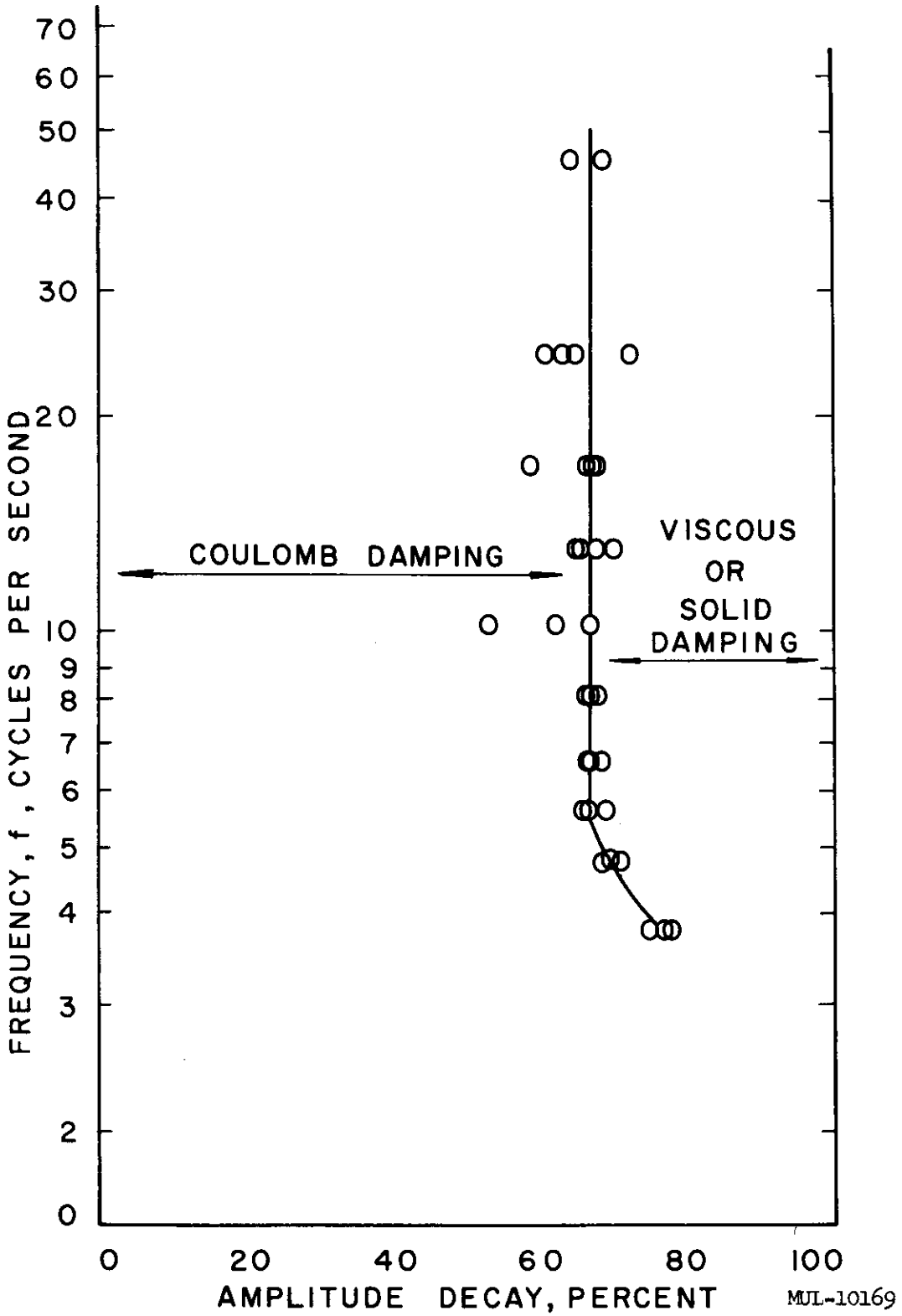

Fig. I-39. Division of energy dissipation from initial displacement to 2% of initial displacement, short module assembly.

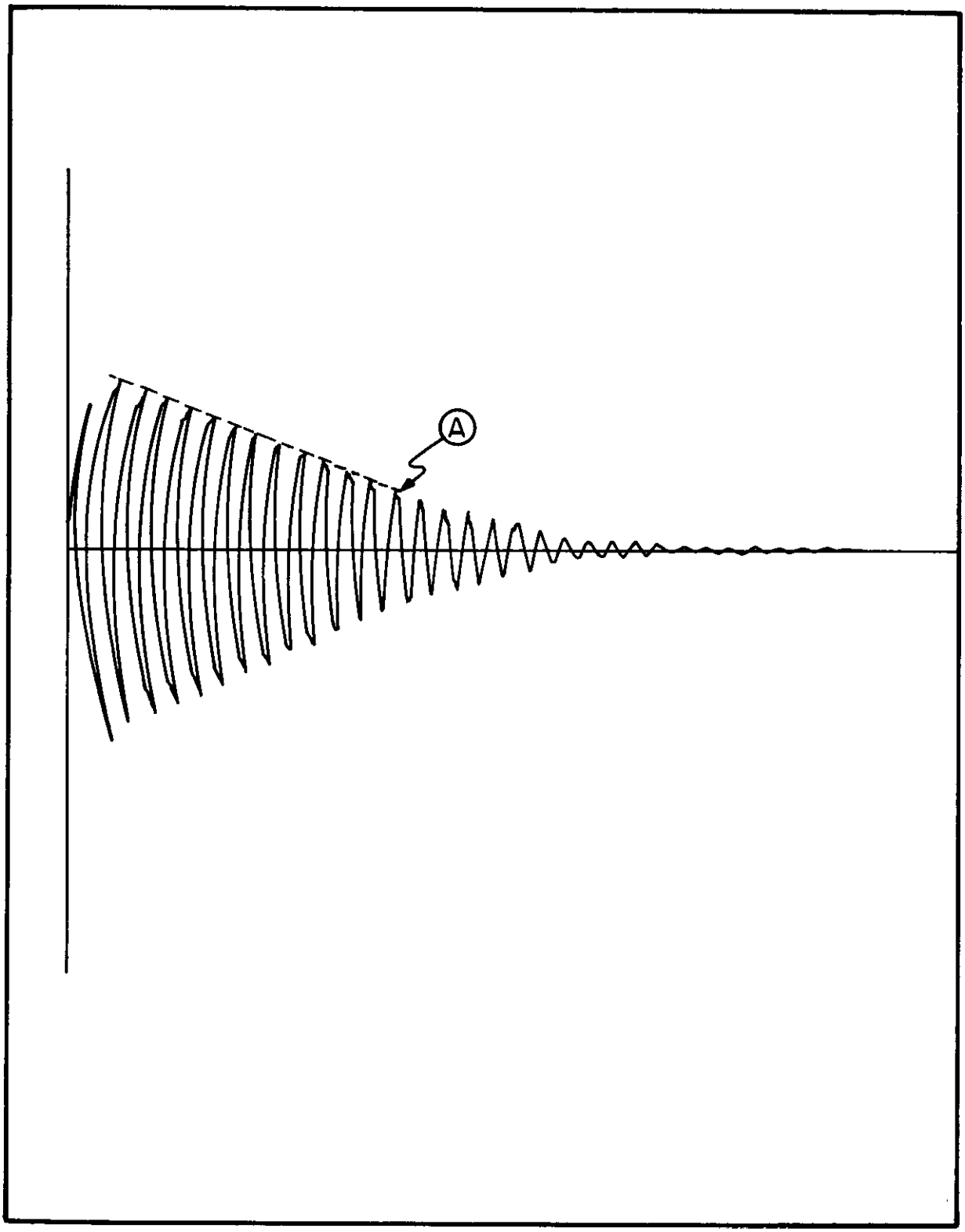

MUL-10170

Fig. I-40. Typical short module damping characteristics.

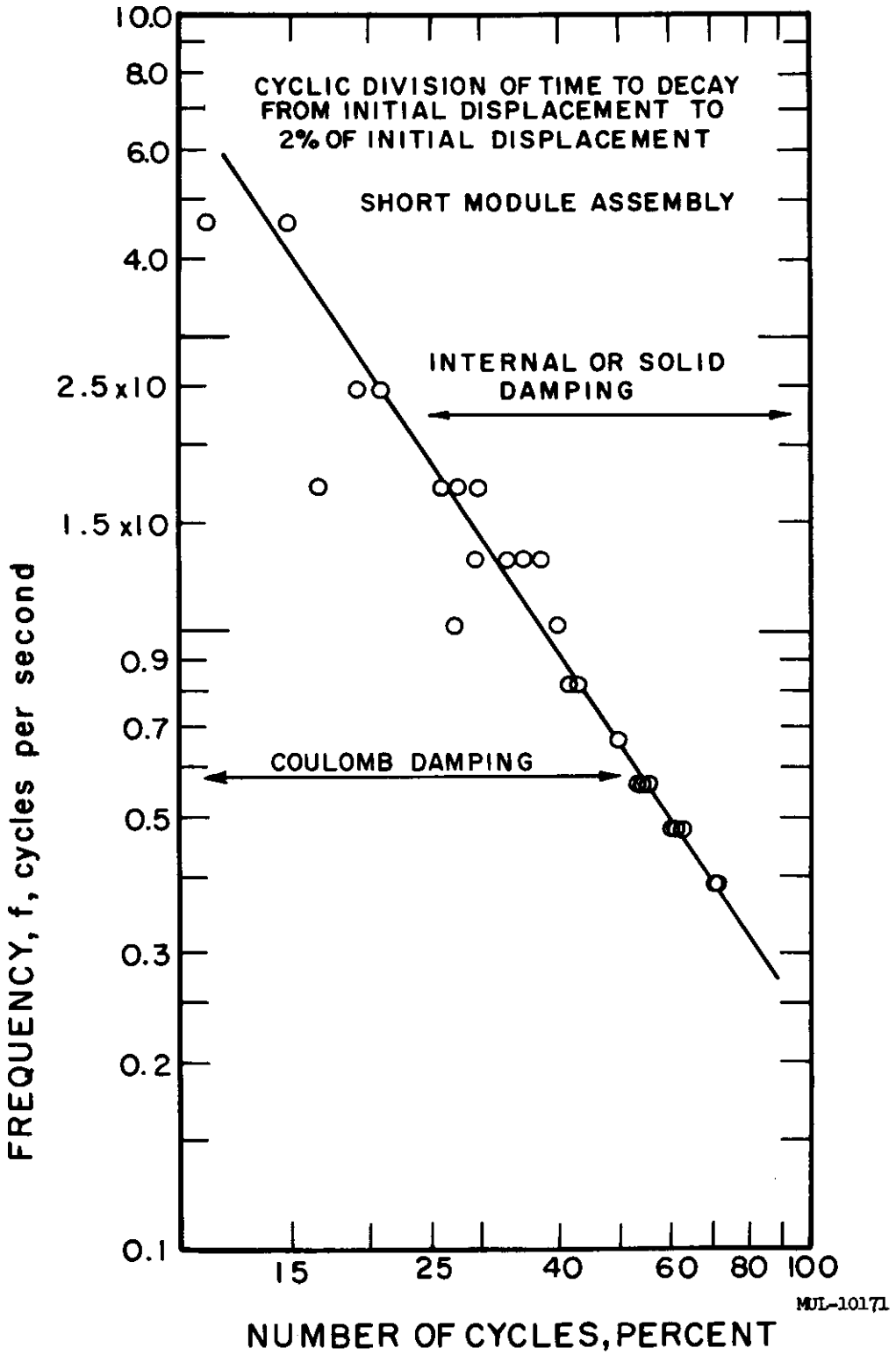

Fig. I-41. Cyclic division of time to decay from initial displacement to 2% of initial displacement, short module assembly.

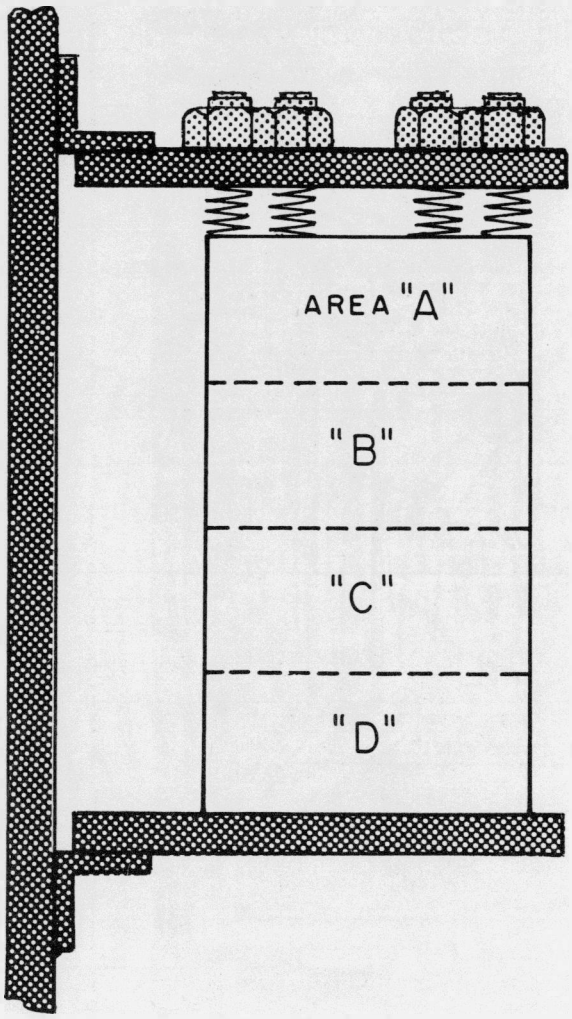

DAMAGE LOCATION	
AREA	No. OF TUBES
A	6
B	3
C	3
D	9

TUBE DAMAGE	
TUBE LENGTH	No. OF TUBES
1 1/2 "	9
2"	2
2 1/2"	5
4"	6

MUL-10172

Fig. I-42. Damage map of chipped tubes, short module assembly.

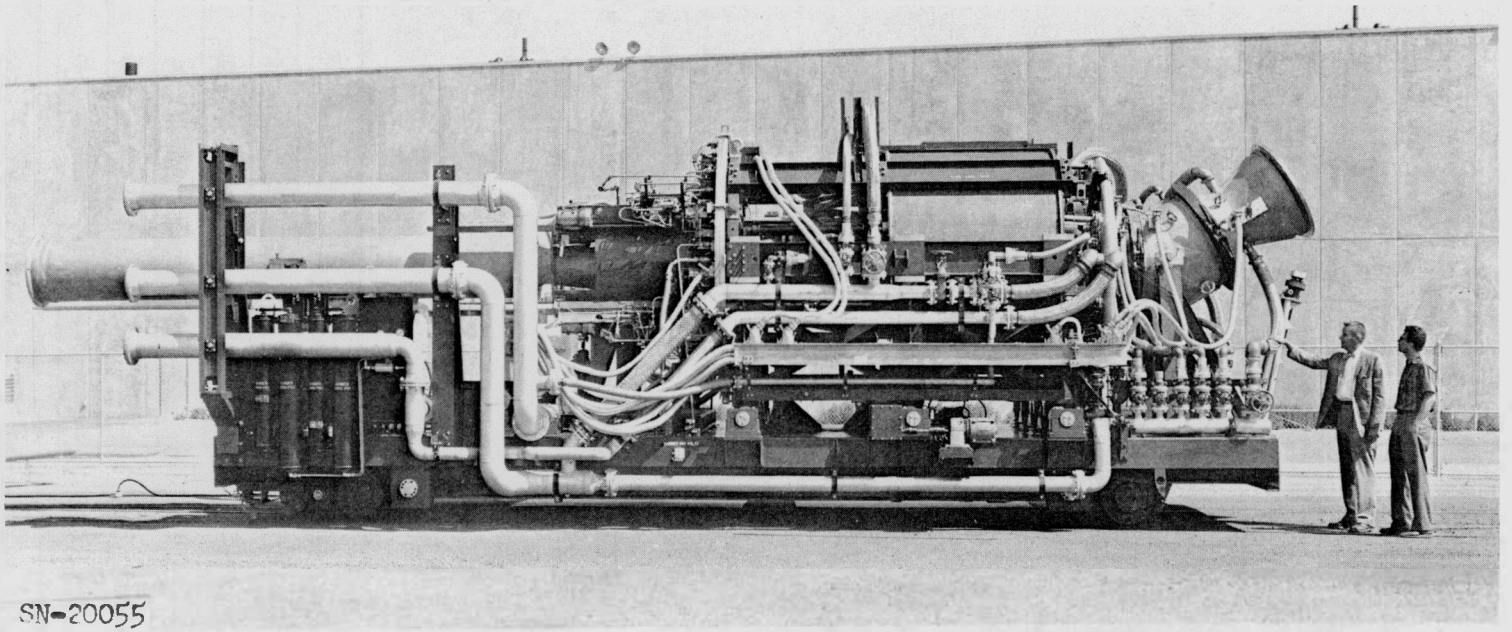

Fig. I-43. Tory II-A test car.

CHAPTER II. MATERIALS DEVELOPMENT AND PILOT PLANT ACTIVITIES

SECTION I. PROCESS AND MATERIALS DEVELOPMENT

I. CERAMICS

A. Materials Studies

1. Preparation and Properties of Pure BeO

The density vs time at temperature data are complete for 35-0 and 35-2 BeO samples isostatically pressed and fired at 1750°C in flowing hydrogen for periods up to 47.5 hours. The 35-0 oxide was prepared by calcining $BeSO_4 \cdot 4H_2O$ for 4 hours at 1000°C in air. The 35-2 BeO was made by calcining (as above) $Be(OH)_2$ precipitated by bubbling NH_3 into the sulfate solution. The times and densities were:

Time at 1750°C in H_2, hrs	35-2 % Theo. Density	35-2 Average	35-0 % Theo. Density	35-0 Average
4	95.3, 95.3, 95.0	95.2	98.5, 98.0, 98.4	98.3
8	96.3, 96.2, 96.2	96.2	98.5, 98.3, 98.5	98.4
12	96.1, 96.2, 96.4	96.2	98.6, 98.6, 98.6	98.6
16	96.5, 96.2, 96.7	96.5	98.8, 98.7, 98.4	98.6
20	96.5, 96.8, 96.7	96.6	99.0, 98.5, 98.6	98.7
24	96.6, 96.7, 96.5	96.6	98.5, 98.4, 99.0, 98.7	98.7
47.5	----------	----	98.7, 98.6, 98.9	98.7

For the two kinds of BeO represented here, maximum densities attainable under our conditions are reached in 20 hours or less.

Preliminary petrographic examination of 35-2 shows that between 4 and 24 hours firing, the small grain material, which is interspersed among the larger grains, grows from ca. 10 to 25 μ in diameter during the sintering. The larger grains maintain a diameter of ca. 50 μ.

2. Fuel Retention and Stability: $BeO-UO_2$

a. General

A noteworthy occurrence during the past quarter has been the observation that fuel loss of $BeO-UO_2$ in air could be reduced markedly by

"annealing" the hydrogen-sintered fuel elements in vacuum at temperatures above the previous sintering temperature. Details are reported below.

b. Effect of Vacuum Reheating

Samples of 0, 5, 10, and 15 w/o UO_2 in BeO were annealed in vacuum at a temperature of 1885°C for a period of one hour. The samples all exhibited a weight decrease as follows:

Lot No.	No. of Samples	% UO_2	Average % Weight Loss
V-3-4	3	0	0.623
V-24	4	5	0.773
V-26	6	10	0.906
V-38	8	15	0.766

Samples from lots V-24 and -26 were analyzed for % UO_2 before and after the vacuum annealing. The data indicate a small UO_2 volatilization loss during annealing, as follows:

Lot No.	% UO_2
V-24 (Control)	5.39
V-24	5.30
V-26 (Control)	10.77
V-26	10.58

One sample each from lots V-3-4, V-24 and V-26 were loss tested in air at 1525°C for a total lapsed time of 452 hours. The data are given in Table II-1.

Table II-1

Lot No.	% UO_2	Vacuum Annealed Wt, grams	Weight (grams) After Heating in Air at 1525°C 4 hrs	10 hrs	40 hrs	116 hrs	452 hrs
V-3-4	0	2.0804	2.0804	2.0803	2.0800	2.0795	2.0792
		% wt loss	0	---	0.02	0.04	0.06
V-24	5.30	2.5566	2.5564	2.5564	2.5559	2.5527	2.5486
		% wt loss	0.008	0.008	0.027	0.152	0.313
		% fuel loss	0.15	0.15	0.51	2.87	5.90
V-26	10.58	2.7283	2.7281	2.7283	2.7281	2.7245	2.5759
		% wt loss	0.007	0	0.007	0.139	5.586
		% fuel loss	0.066	0	0.066	1.31	*52.78

The sample from lots V-24 and V-26 were analyzed after the 452-hour test for % UO_2. The data are as follows:

Lot No.	% UO_2 (Chem. Analysis)	% UO_2 (Determined from Weight Loss)
V-24	4.85	4.99
V-26	5.16	5.02

* This effect due to furnace failure. See text.

In an attempt to determine the effect of the time and temperature of vacuum annealing on the fuel loss, samples from lot V-16 containing 5 w/o UO_2 in BeO were annealed for various times and temperatures. The samples all exhibited a weight decrease (Table II-2). It was interesting to note that all of the samples gained up to 1% in density except those heated for 20 minutes at 1885°C. Samples from the various runs were loss tested in air at 1525°C. The results are tabulated in Table II-2.

The failure which occurred to the sample from lot V-26 (Table II-1) (10 w/o UO_2) appeared to be due to a power failure which permitted the furnace to cool slowly to a temperature below red heat. It is felt that this is related to the volume of material that undergoes the $U_4O_9 \rightarrow U_3O_8$ transformation.

The weight loss which occurs on vacuum annealing is chiefly vaporization of BeO, since repeated vacuum heatings of unfueled BeO samples at 1885°C give essentially a constant rate of weight loss with time. This rate is about the same as that measured for BeO-UO_2.

Table II-2

No. of Samples	2	2	2	2	3
Vacuum Anneal Temp (°C)	1885	1885	1885	1780	1675
Anneal Time (min)	20	40	60	60	60
Average % Weight Loss	0.58	0.37	0.56	0.16	0.06
Density (g/cc)					
Original	3.07	3.051	3.050	3.07	3.07
After Anneal	3.07	3.060	3.053	3.09	3.09
w/o Loss in Air*					
4 hr at 1525°C	0.36	0.03	0.01	0.01	0.04
20 hr " "	--	0.04	0.03	0.05	--
~100 hr " " **	--	0.173	0.145	0.201	--

* To determine % fuel loss, multiply by 20.

** The time is approximate since furnace failure occurred over the weekend.

Examination of thin sections of the 1885°C vacuum-annealed specimens indicated that there has been a depletion of fuel from the grain boundaries at the surface with subsequent densification of the surface grains. This apparently has affected the rate of oxygen diffusion in that a sample after 117 hours at 1525°C in air was still brown in the center, indicating that the fuel was still UO_2 and not black U_4O_9.

The nature of these experiments is encouraging in that it represents a factor of 4 or better improvement of the fuel retention at 1525°C in air.

c. Effect of Heating in Various Atmospheres

Because improved fuel loss was obtained by treatment at 1885°C in vacuum, heating in other atmospheres was also tried. It was conceivable that the elevated temperature was significant, not the vacuum.

Hydrogen. Several green specimens were sintered in hydrogen to 1925°C with a 6-hour soak at temperature. Fuel losses were measured at 1525°C, 1650°C and 1800°C for 4 hours in 5 liters/min dry air flow. See below.

	Average Density g/cc	% Fuel Loss, 4 Hours at 1525°C	1650°C	1800°C
(V-18) 1725°/5 hours	3.2252	1.36 (average)	1.97 (average)	---
(V-19) 1925°/6 hours	3.2439	1.1/1.4/1.3	3.5/2.8/2.3	42.3/37.4/43.1

Evidently firing in hydrogen at high temperatures does not improve fuel retention properties.

In another set of tests, the normal sintered BeO-UO_2 tubes (i.e., 1725°C/5 hours) were heated in H_2 at 1800°C for 30 minutes, which gas was then swept out by He. Finally, dry air was passed over the sample at 1800°C for 4 hours. Losses were high, viz., 50-72% fuel loss, in contrast with the helium tests reported below.

Helium and Argon. The rationalization that UO_2 is the more stable phase at high temperatures led to fuel loss testing in air at 1800°C, after bringing a specimen to temperature in helium.

In the first experiment, a 10% UO_2 tube was heated to 1800°C in helium and kept at that temperature for about 1/2 hour. The furnace atmosphere was then changed to air at 1800°C and the specimen held for 4 hours. The fuel loss was remarkably low (1%). Subsequent tests were also made in pure helium to check weight loss due to this treatment. Other tests were made in helium and argon, but evidently air leaked into the furnace during the inert gas treatment, and invalidated the results.

Test	% Weight Loss	% Fuel Loss	Remarks
1. He 1800°C	0.04/0.04	----	Specimen not oxidized after test.
2. He 1800°C, Air 1800°C 4 Hours	0.094/0.098	1.0	----
3. He 1800°C	0.199*	----	Specimen oxidized. Evidently leaky furnace.
4. A 1800°C	0.171/0.160*	----	"
5. A 1800°C, Air 1800°C 4 Hours	6.4/6.2*	63*	"

* These data are invalid because air leaked into the furnace during the inert gas treatment, as evidenced by oxidized appearance (black).

The tube from test #2 in the above tabulation was subsequently tested at 1525°C for 4 hours. No change in weight was observed. After another 20 hours, the fuel loss was 0.46%, which is also a low figure.

In another set of parallel experiments, sintered BeO-10% UO_2 tubes were heated in helium and then in air to follow urania loss behavior.

In the initial experiment at 1650°C, weight losses in air of two helium-fired samples were one-fifth of those of control samples tested in air only (Fig. II-1). The weight losses of these samples in air continued at this low rate for 28 hours and then increased to rates comparable to those of the control samples.

In further experiments (Fig. II-2) the reduction of weight loss in air was verified and the time and temperature of heating in helium were varied from 2 to 16 hours and 1525 to 1650°C to briefly explore effects on the reduction of loss and the duration of low weight loss when subsequently tested in air.

In general the longer times at the higher temperatures showed greater subsequent suppression of urania loss. However, air leaked into the inert atmospheres of the furnaces, and so quantitative conclusions are not warranted. Future work will concentrate on higher temperature inert gas treatment.

d. Effect of Cooling

Evidence indicates that fuel loss may be seriously affected if a fueled sample is cooled through the U_3O_8 range after high temperature testing. Thus experiments were carried out under controlled conditions of cooling from 1525°C. Specimens were cooled to 600, 900, and 1200°C respectively, and at rates of 5, 10, and 30°C per minute. Also varied were the factors of the time at 1525° before cooling; time at cooled temperature; and effect of thermal cycling. In the last case, a sample was placed in a furnace at 1525°C for 5 minutes to reach temperature, withdrawn to cool, then placed in again.

The following Table II-3 gives a condensation of the data accumulated to date. Tests were run on high density 10 w/o V-26 tubes, which had been sintered at 1750°C for 6 hours in H_2. An air flow of 5 liters/min was used in all experiments.

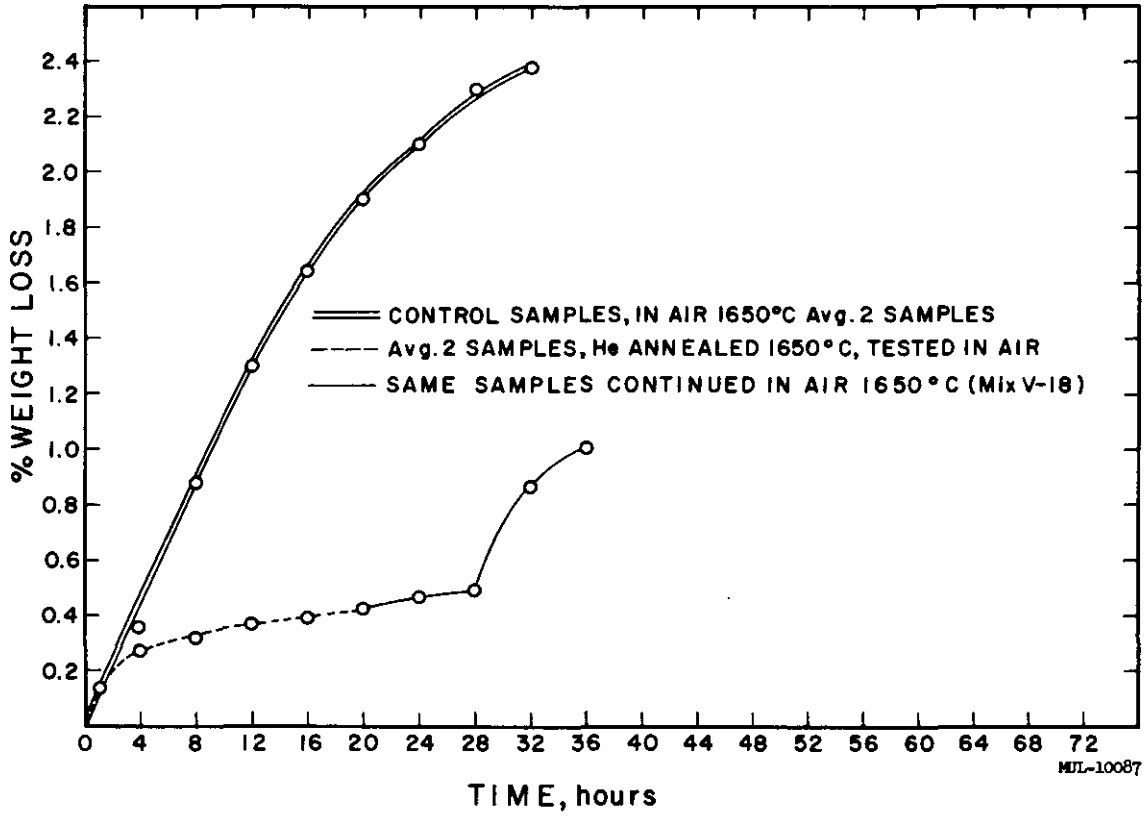

Fig. II-1. Weight loss vs time.

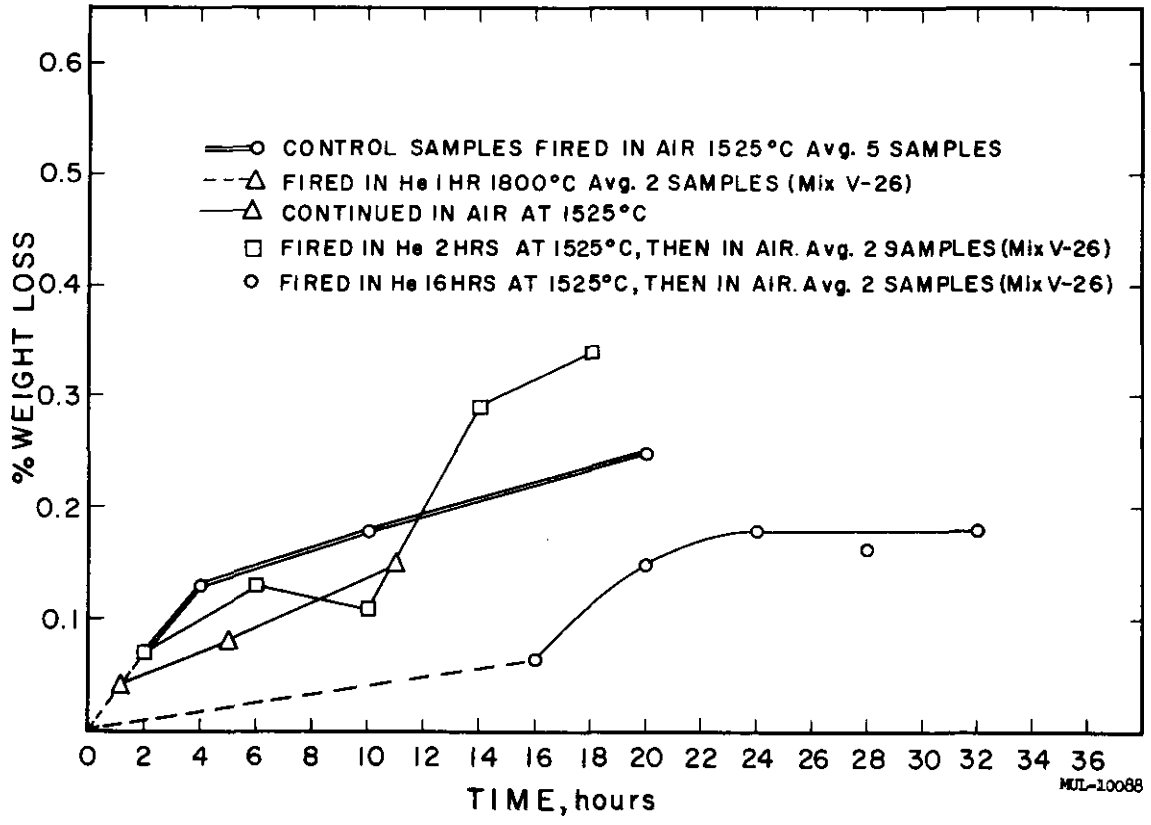

Fig. II-2. Weight change vs time. 1650° temperature, dry moving air (5 liters/min).

Table II-3

Item	Rate of Cooling (per min)	Cool Temp & Time held at Cool Temp	Time at 1525°C Before Cool Off (Hours)	% Fuel Loss
1	30°C	900°C – 1 hr	1	1.53/1.82
2	30°C	900°C – 1 "	4	2.15/1.67
3	30°C	900°C – 1 "	16	5.24/5.24
4	30°C	900°C – 5 min	16	3.29/6.39
5	10°C	900°C – 1 hr	16	6.80/5.20
6	5°C	900°C – 1 "	16	7.85/7.43
7	30°C	600°C – 1 "	16	7.70/7.47
8	30°C	1200°C – 1 "	16	6.00/6.29
9	10°C	1200°C – 1 "	16	7.58/8.35
10	5°C	1200°C – 1 "	16	5.98/7.02

	Air Quenches 5 min at 1525°C rapidly quenched (15 times)	Same Treatment Plus 4 Hours at 1525°C	16 Hours at 1525°C; Single air quench; 4 Hours at 1525°C	16 Hours at 1525°C; Single air quench; 1 Hour at 1525°C; Cooled at 30°/min to 900°C; held 1 Hour; back to 1525°C for 3 Hours
% Fuel Loss:	0.97	1.48/1.61	1.97	4.10

From the above tables, the following conclusions may be drawn:

1. The longer the material is at 1525°C (conversion of UO_2 to U_4O_9), the greater the effect of cooling to the U_3O_8 range. (Items 1, 2 and 3, Table II-3). This is consistent with relatively rapid conversion of U_4O_9 to U_3O_8 and ready volatilization of the uranium as UO_3 after ready transformation from U_3O_8. This may be a mechanical instead of a chemical effect, since the slight shrinkage of UO_2 to U_4O_9 might permit access of O_2 to the urania or easier paths for mass transfer of UO_3 through the BeO.

2. The time the specimen is at the lower temperature seems unimportant (Items 3 & 4). The rate of cooling, or the total time in the U_3O_8 range, appears to have a modest effect (Items 3, 5 and 6).

3. The temperature to which the material is cooled may also be pertinent, (Items 3, 7 & 8) although this in effect could be the length of time in the U_3O_8 range. The data show ambiguous, but minor effects.

4. Multiple (15) air quenches were carried out by inserting a sample into a 1525°C air furnace, allowing it to stand for 5 minutes, then removing it. The insertion and removal take a few minutes each to prevent severe shock. The fuel loss was about 1%. However, this treatment followed by 4-hour air loss testing at 1525°C shows no enhanced loss at the latter temperature. Thus, thermal cycling of a virgin fuel element does not per se increase loss appreciably.

5. Also note that a 16-hour loss test followed by an air quench and a final 4-hour loss testing period at 1525°C does not show enhanced loss. Thus again the air quench had little effect.

6. However, a similar treatment in combination with relatively slow cooling (30°C/min) to 900°C did augment fuel loss by a factor of 2.

e. Effect of Thermal Cycling

5 w/o and 10 w/o thermal cycled tubes which had been through 15 slow cycles of 1250°F to 2500°F (reported in report No. 2, UCRL-5829) were loss tested at 1525°C for 4 and 10 hours. Results are seen in Table II-4. The losses are about 2-1/2 times that of the usual fuel losses without thermal cycling. This result is consistent with the results mentioned in the experiments on cooling. Note that these were slow cycles of several hours each as opposed to the air quench tests referred to in a previous section.

Table II-4

w/o UO_2	% Fuel Loss (temp. 1525°C)	
	4 Hours	10 Hours
	5.72	17.02
10	3.88	13.17
	6.30	16.59
	6.40	13.64
5	4.62	13.67
	5.28	9.68

f. Effect of Surface Grinding

Previously we reported enhanced fuel loss of ground tubes and reduction in this loss effected by annealing in hydrogen. More extensive tests were carried out this quarter. Specifically, tube surfaces were ground on a lathe. Some were loss tested, and others annealed in hydrogen for various times, then air loss tested. All tubes contained 10% UO_2. The following data include previous tests as well as the new tests. It is evident that some, but not a marked, improvement is effected by hydrogen anneal. It is also evident that the smoother surfaces created in these tests resulted in somewhat lower fuel loss.

	% Fuel Loss	
	4 Hours 1525°C	4 Hours 1650°C
Previous Tests:		
Surface ground	---	9.7/9.6/9.3
Annealed 1 hour at 1725°C in H_2	---	5.3/5.1/6.0
Present Tests:		
Surface ground	2.2/2.5	6.5/7.4
Annealed 2 hours at 1725°C in H_2	2.1/1.4	5.8/4.4
Annealed 4 hours at 1725°C in H_2	1.3/1.2	4.5/5.6
Comparison Results:		
Virgin tubes (unground)	1.2/1.4	1.8/2.7

3. System $BeO-UO_2$

a. Phase Diagram: Be-U-O

There is need for a more thorough knowledge of the phases present in this system in air at temperatures above 1500°C. Specifically, we would like to know if U_4O_9 or UO_2 is stable in air up to the melting point and if there is a significant amount of BeO solid solution in UO_{2+x}.

Powder samples were wrapped in rhodium foil to allow for exposure to air but retard loss due to urania volatilization. The furnace was heated to constant temperature and then the sample was introduced. After about one-half hour the sample was quenched into water.

A pure sample of U_3O_8 was heated and quenched in this manner at 1500°C in air. The x-ray results showed a lattice parameter of $A_o = 5.437$, equal to that reported for U_4O_9.

Samples of 90 w/o BeO and 10 w/o UO_{2+x} were quenched at 1525°C and 1800°C. There are indications that both an orthorhombic and a cubic fluorite phase are present. An orthorhombic phase is contrary to what would be expected in view of the results from the urania quench tests.

4. BeO Coatings

Work on a zircon coating has been discontinued because of its tendency to spall. This is expected in view of its low expansion coefficient as compared with BeO.

An effort is being made to develop a zirconia (stabilized) coating for BeO. Figure II-3 shows the thermal expansion of zirconia stabilized with 5% CaO (commercial product called Zircoa-B). Zircon is also shown in Fig. II-3. 5 w/o SiO_2 was added to Zircoa in an effort to lower zirconia's expansion coefficient to that of BeO. According to the ZrO_2-SiO_2 phase diagram 5 w/o SiO_2 will go into solid solution with zirconia. The coating is essentially a ZrO_2 solid solution with 5 w/o CaO and 5 w/o SiO_2.

A platinum coating for $BeO \cdot UO_2$ tubes was tried to inhibit BeO loss at high temperatures in high humidity air. Tubes were coated with 17 mils of Pt by a wash technique. The tubes were then run at 1525°C for 4 hours in air saturated at 100°F. The coating did not protect the tubes. There was an appreciable weight loss and the platinum appeared to spall off. X-ray diffraction showed no expansion of the Pt lattice.

5. System Be-B

An oxidation test was performed in air on a fused sample of BeB_6. The sample prior to test exhibited a metallic lustre and seemed to be very dense though irregular in shape. Hardness prior to test was (HKN-100) = 2267 ± 30.

The test conditions and results were:

	Temperature	Time at Temperature	% Weight Gain
Test I	1380°C	22 hours	2.8
Test II	1200°C	24 "	
	1400°C	24 "	
	1500°C	24 "	4.2
		Total Weight Gain:	7.0

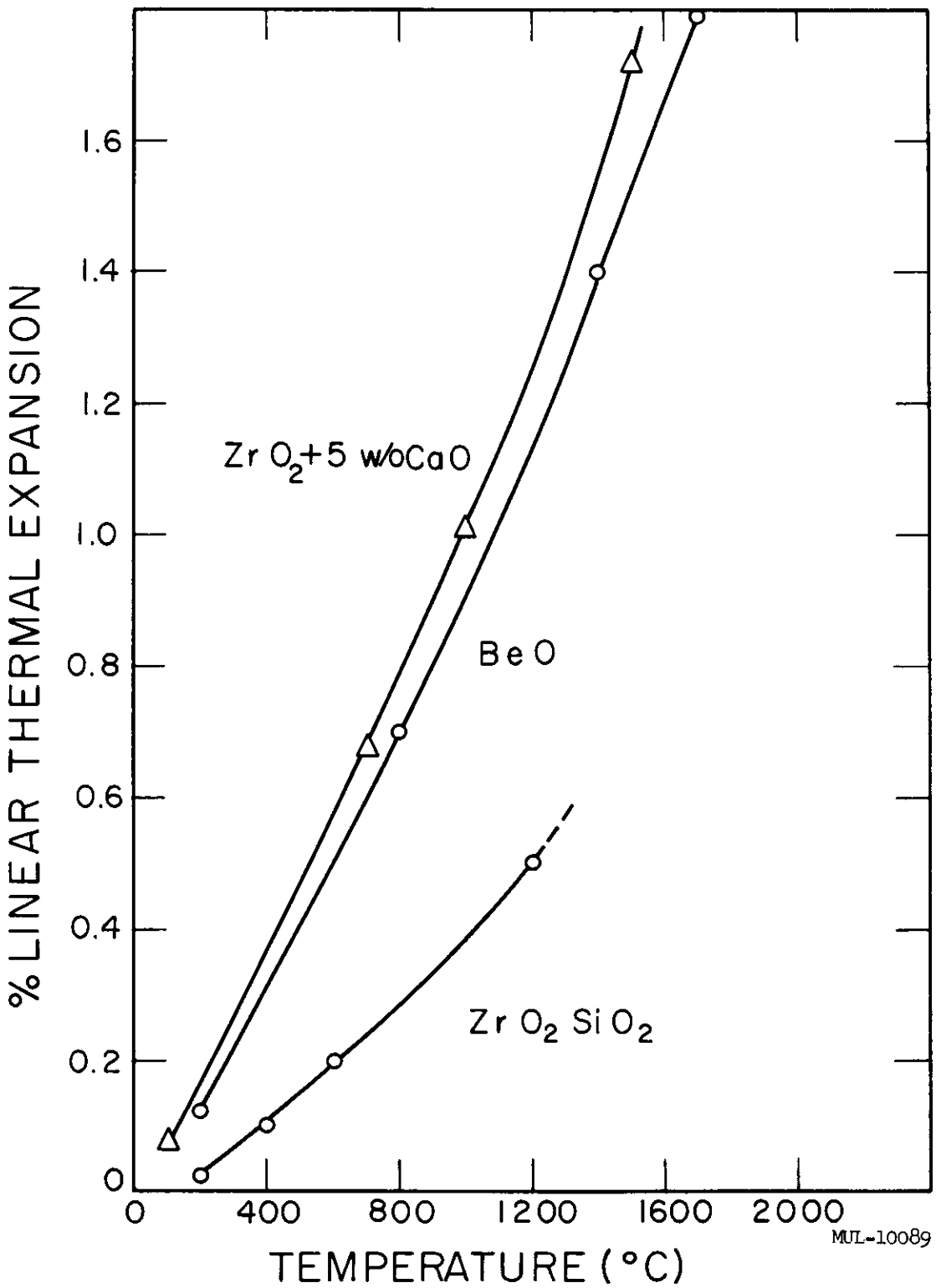

Fig. II-3. Percent expansion vs temperature.

In order to relate this small weight increase to amount of BeB_6 actually reacted, the most likely reaction which can occur is

$$BeB_6 + 5\,O_2 \rightarrow 3\,B_2O_3 + BeO$$

The vapor pressure of B_2O_3 is relatively high at 1500°C ($\sim 10^{-3}$ atmos). One would expect total loss of any B_2O_3 formed but this would result in a net loss whereas a net gain was experienced. X-ray analysis of reaction product indicated only $BeO + BeB_6$. If no loss of B_2O_3 is assumed, the 7.0% weight gain resolves into a 3.5% BeB_6 reacted. This is a low oxidation rate for a boride.

Final metallographic and microhardness examination indicated:

1. A very thin reaction layer existed at the surface which appeared to be BeO. It was difficult to establish whether or not this reaction product was continuous or discontinuous.

2. No measurable change in microhardness was found from edge grains to center grains. Edge grains: (HKN-100) = 2113 ± 140
Center grains: (HKN-100) = 2268 ± 120

B. Fabrication Development and Production

1. Fuel Element Fabrication Facility

The procedure for producing Pluto reactor fuel elements is as follows:

Beryllium oxide powder is added to a solution of uranyl nitrate. The uranium is precipitated using ammonium hydroxide and the solids are filtered and dried. A weighed batch of the dried material is mixed with a measured amount of water and binder. The mix is aged, extruded to shape, cut to length and dried. The dried tubes are heated in air to 1500°F to remove the binder, then fired to 1775°C in a hydrogen atmosphere to final density.

Over 450 batches of about 1700 grams each have been precipitated during the past 3 months. About 300 of these have been extruded. Approximately 20,000 tubes have been fired in the large kiln and 700 in the smaller modified kiln.

C. Mechanical Properties – Compressive Creep

The Table II-5 and associated creep curves Figs. II-4 and II-5 summarize the results of four tests on pure extruded BeO. Comparisons of these particular results should be made cautiously as the specimens had a variety of production histories.

However, the relatively large creep strains in a ceramic material at these temperatures and stresses are significant. In addition, specimen densities in the tests made at 2400°F are low in comparison with material now being produced. Future investigations are planned to explore creep at high stresses and relatively low temperatures on high density material.

Table II-5

Specimen	Density, %Theo.	Temp., °F	Stress, psi	Total Strain, %	Time, Hrs	Secondary Creep Rate in./in./hr×10^{-4}	Remarks
7×115-3	98.3	2800	1500	1.12	138	0.74	Test discontinued
7×115-4	97.8	2845	1500	0.61	26	1.41	Heating element failure
4E137-2	90.7	2400	3000	1.87	125	1.32	Power failure
4E137-3	94.3	2400	6000	2.50	125	1.96	Power failure

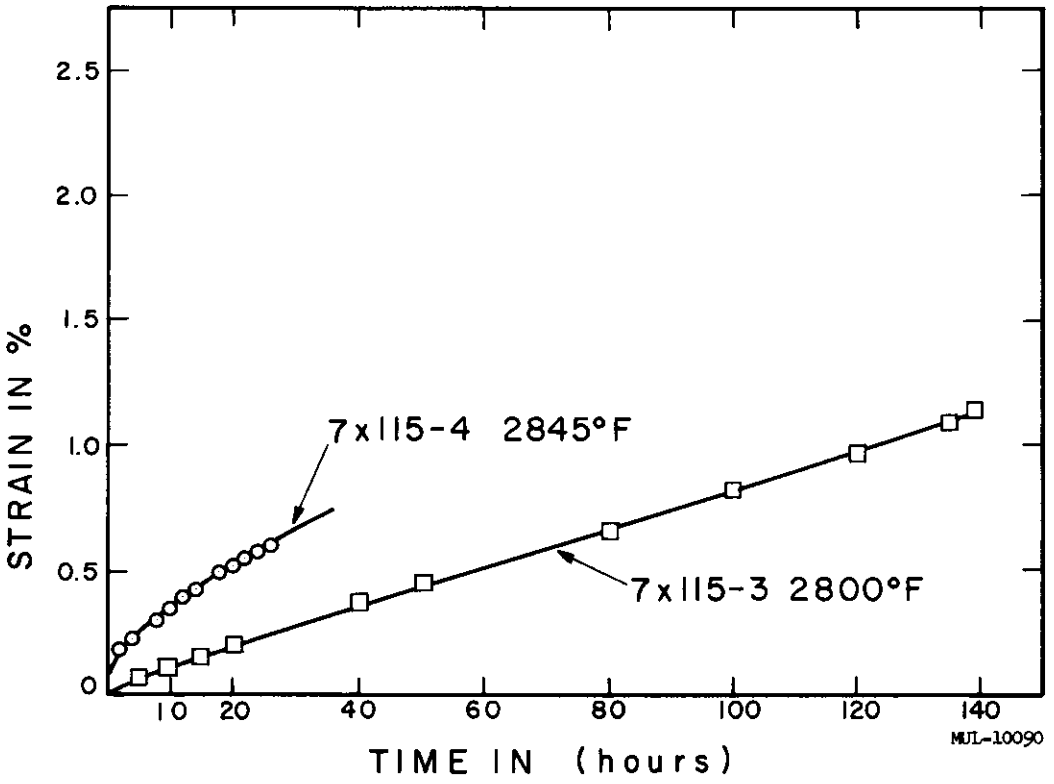

Fig. II-4. BeO compressive creep, 1500 psi.

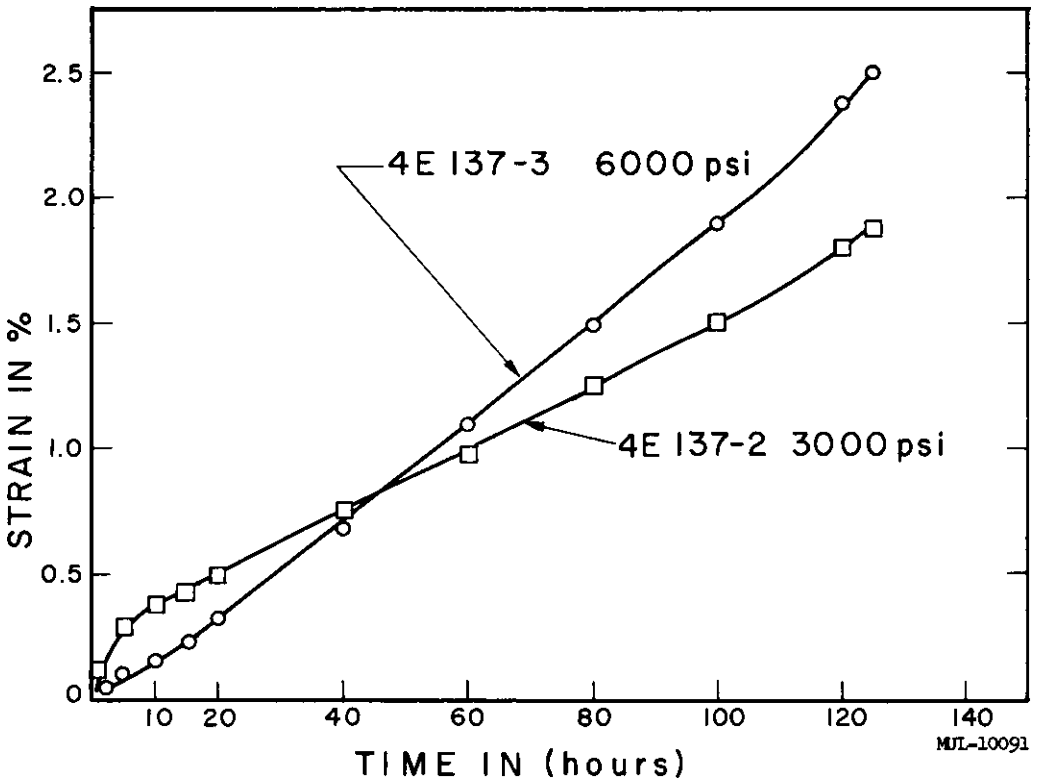

Fig. II-5. BeO compressive creep, 2400°F.

SECTION II. GENERAL CHEMISTRY

ELECTRON MICROSCOPY

Characterization of Powdered BeO

The examination of six samples of BeO powders calcined at 1000°C has been finished. Of these samples, one was calcined directly from $BeSO_4 \cdot 4H_2O$, three were calcined from $Be(OH)_2$ containing varying amounts of residual sulfate, and two were foreign-made and the starting material is unknown. Photographs from the electron microscope have provided the following information:

1. The most common particle length for BeO powder from the sulfate is approximately 0.1 to 0.3 microns, while that for the hydroxide-derived powder is 0.06 to 0.08 microns.

2. Many of the particles made from sulfate are elongated hexagons which are half as wide as they are long. The hydroxide-derived particles are more nearly round.

3. These differences in size and shape permit the identification of particles which have been formed from the sulfate impurity in $Be(OH)_2$. However, a sulfate particle count does not provide a semi-quantitative sulfate analysis, because the sulfate is not evenly distributed in the hydroxide.

4. Particle size and shape cannot be correlated with sinterability.

MATERIALS DEVELOPMENT

Transition Metal Aluminides

To establish an approximate phase diagram for the Nb-Al system, samples of various compositions, pressed into 1/4 in. o.d. pellets approximately 1/2 in. high, were heated in a graphite tube furnace. As the furnace was slowly raised in temperature, the temperature at which the pellets first began to melt and the temperature at which the pellets had completely melted were measured with a micro-optical pyrometer. The pellets were placed on Ta sheet which was in turn placed on a graphite block in the furnace. The Ta sheet prevented reaction of the samples with the graphite, and the graphite block provided a good blackbody for observing temperatures. Samples for the pellets were prepared as described in the previous quarterly report (UCRL-5925, p. 126).

Preliminary results show that $NbAl_3$ decomposes peritectically at 1600°C. Samples of this composition are completely molten at 1725°C. Nb_2Al melts at 1925°C and Nb_3Al at 2040°C. Whether or not these compounds have congruent or incongruent melting points has not yet been determined.

A number of new sample preparations and reheatings has been made in the Ta-Al system. In addition to Ta_2Al and $TaAl_3$ a new compound has been found at a composition of $TaAl_{1.7}$. There is also evidence to suggest the existence of another compound in the composition region $TaAl_{1.0-1.5}$. Phase identification was by means of x-ray diffraction.

The compound Ta_2Al was observed as a single phase with a continuously varying structure over the composition region Ta_3Al to Ta_2Al. It was also observed that Al dissolves in Ta resulting in a small contraction of the Ta lattice.

Oxidation Testing of Niobium Base Alloys

Several Nb base alloys were received from a supplier and were subjected to oxidation resistance tests in still air at elevated temperatures. The composition of the alloys are given in Table II-6.

Small pieces of the alloys were cut from the ingot and placed in a Al_2O_3 crucible suspended from the pan of an analytical balance into a constant temperature furnace. The weight of the piece could thus be recorded as often as desired without cooling and reheating the specimen. Oxidation rate curves for the alloys were first obtained at 1013°C and 1104°C, and then the most oxidation resistant alloys were tested at 1190°C. The results of these tests are given in Figs. II-6, II-7, and II-8.

The depth of penetration was determined by measuring the piece before heating and again subsequent to testing. In general, measured penetration agreed well with that calculated from the weight-gain data. In most cases the oxide coat spalled off upon cooling; in those cases where it did not it was removed mechanically before measuring.

The alloys designated as 283, 78 and 292 all exhibit oxidation resistance greatly superior to the 90-10 Ta-W alloy. All three also appear to follow a parabolic rate law. If the oxidation resistance of these alloys proves insufficient for use without coating, they sould certainly be considered the most logical candidates for coating.

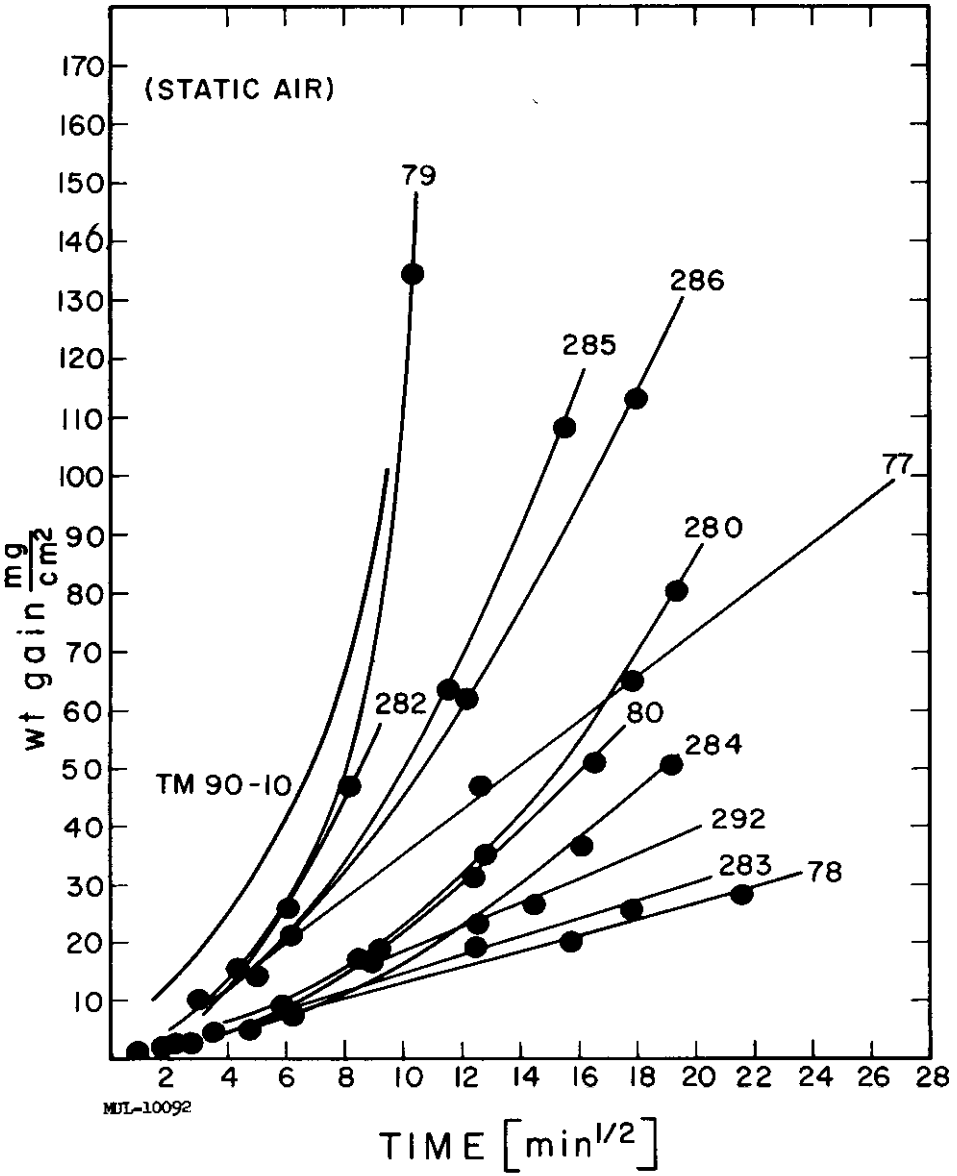

Fig. II-6. Oxidation rates of Nb base alloys at 1013°C.

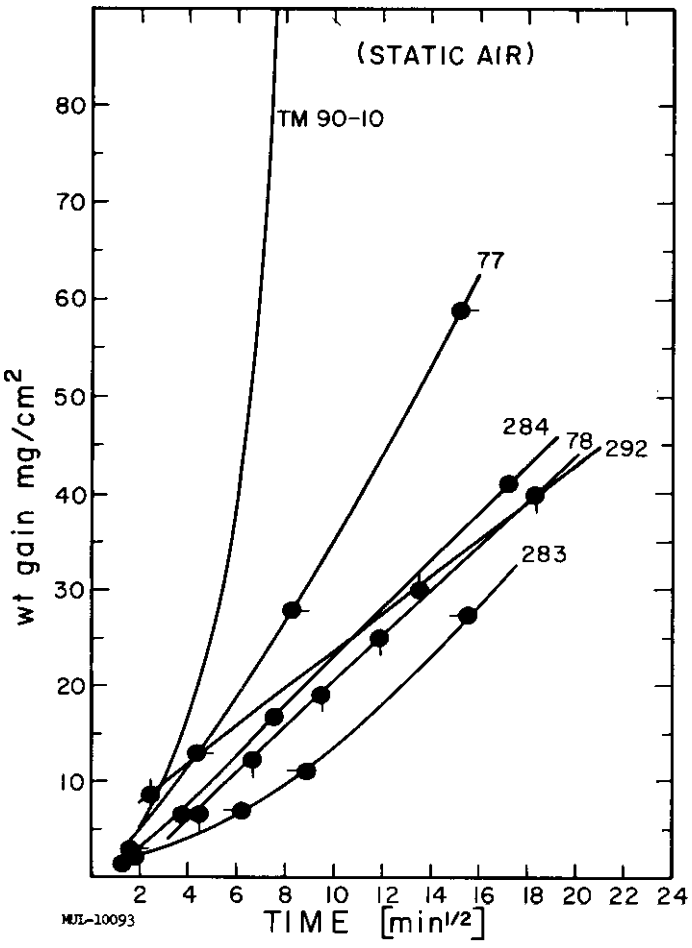

Fig. II-7. Oxidation rates for Nb base alloys at 1104°C.

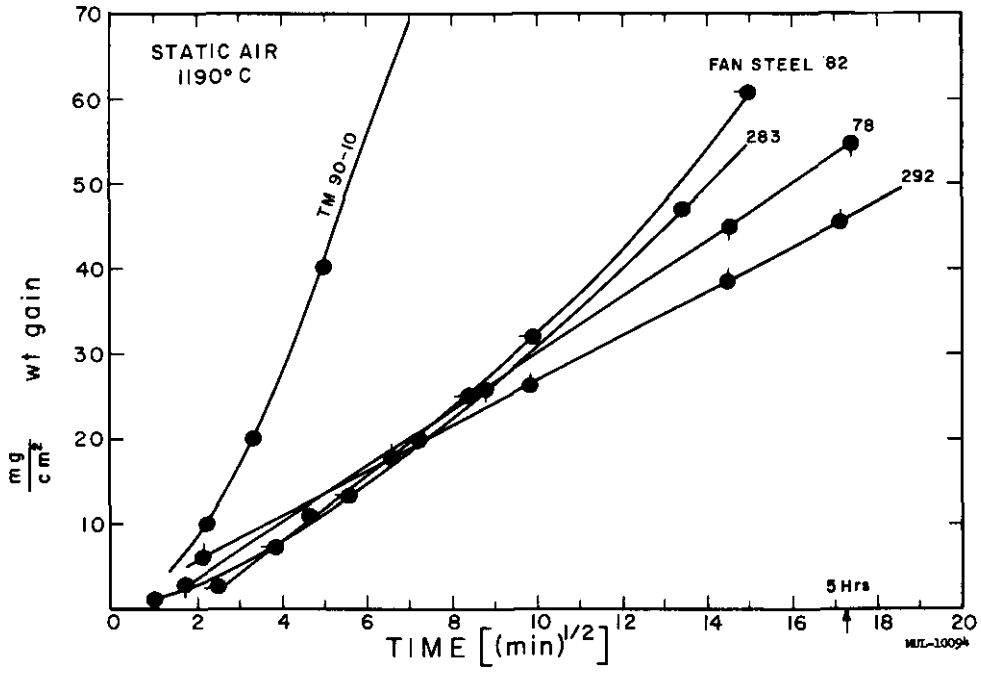

Fig. II-8. Oxidation rate curve for Nb base alloys and fansteel 82.

Table II-6. Weight Percent Compositions of Niobium Base Alloys

Alloy Number	Nb	Ta	W	Mo	Co*	Zr
1	--	90	10	--	--	--
77	85	10			5	--
78	80	10	--	10	--	--
79	85	--	10	--	5	--
80	87	--	10	2	--	1
280	87	--	10	2	--	1
282	85	--	--	10	5	--
283	85	5	5	--	5	--
284	80	5	10	5	--	--
285	40	46	10	3	--	1
286	40	50	10	--	--	--
292	60	30	10	--	--	--
298	60	30	10	--	--	--

* Reports indicate that most of the Co is lost during vacuum melting of the alloy.

MUL-10104

Oxidation Resistance of Cr

Fused lumps of Cr supplied were abraded to rectangular solids and tested for oxidation resistance in still air using the thermobalance. The oxidation in mg/cm^2 is given in Fig. II-9. Oxidation proceeds according to a parabolic rate law in the temperature range of this investigation. By plotting log (rate constant) versus 1/T (see Fig. II-10), an activation energy of 36.0 kcal/mole is obtained for the oxidation process.

Oxidation Resistance of Y Metal

A specimen of Y was cut out of a 99.99% purity fused ingot. The weight change when exposed to still air was measured with a thermobalance. The oxidation was found to follow a linear rate law at 1200°C (see Fig. II-11). Approximately 0.030 in. of oxidation resulted after 2 hours at this temperature.

Studies on Scandium Metal

Scandium is an element whose chemical and physical properties have received little attention. Recent work has shown that it is a high melting metal (m.p. ~1570°C) of low density (ρ = 2.995 g/cm^3).[1]

To learn more about the properties of Sc, 50 grams of arc-melted ingots, 1/2 in. to 1 in. diam were procured. Spectrographic analysis gave a purity of 99.99%. The following measurements were made during the quarter:

1. Melting Point of Sc. The melting point of Sc was measured in a V-shaped Ta foil heater in a vacuum of 3×10^{-6} mm Hg. Melting was observed at an apparent temperature of 1460 ± 30°C as read on the Ta surface. The correction for the low emissivity of the Ta surface and the absorption of the windows was 142°C. The melting point of Sc is thus 1602 ± 30°C.

2. Hardness of Sc. The hardness of Sc measured by a Rockwell "F" hardness tester (60-kg load, 1/16 in. ball) gave a value of 42. A Barcol Impressor measured a hardness of 70. These values converted to the Knoop (500-g load) scale give a hardness of 70 ± 6.

---

[1] Herrmann, K.W., Daane, A.H., and Spedding, F.H., "Some Physical-Metallurgical Properties of Scandium, Yttrium and the Rare Earth Metals", ISC-702, 1955; Data Sheet, Research Chemicals Division of Nuclear Corporation of America.

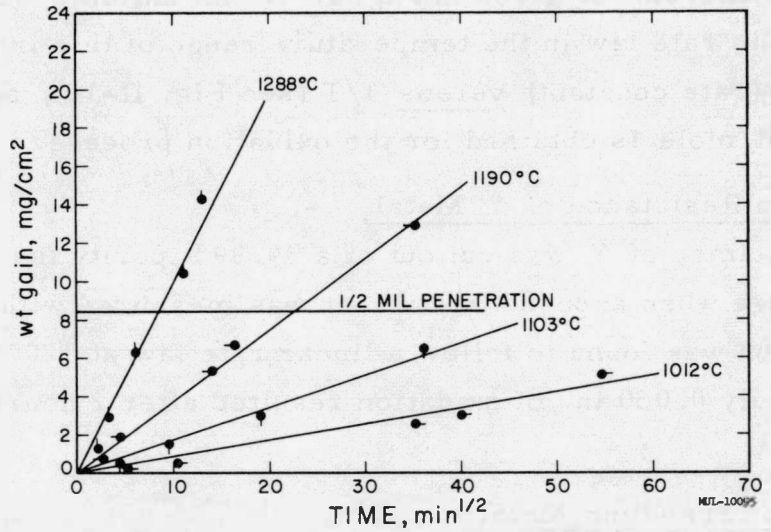

Fig. II-9. Oxidation rate curves for Cr.

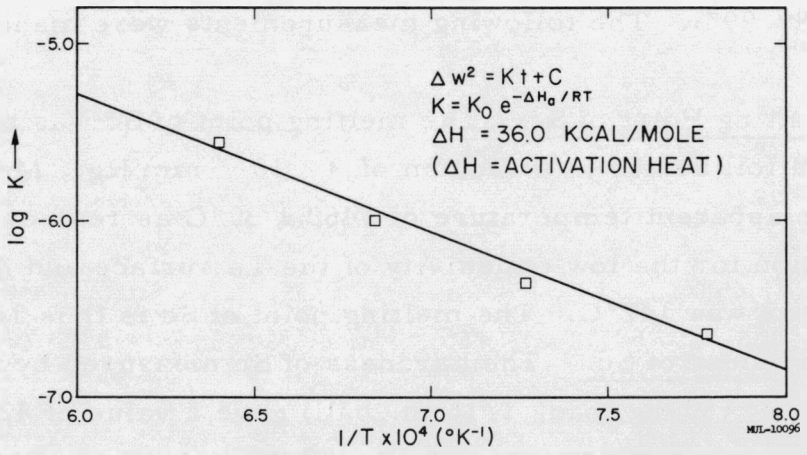

Fig. II-10. Log k vs 1/T for Cr metal.

3. Ductility of Sc. One of the ingots as received was swaged down to a 0.3-in.-diam rod after only one intermediate annealing at 1200°C. This rod was used to measure the thermal diffusivity of Sc, which is given later in Table II-11.

4. Vapor Pressure of Sc. An all-Ta Knudsen cell and heater assembly was constructed and thoroughly outgassed at 2000°C. Measurements of the temperature profile of the cell showed gradients to be less than 5-10°C, Sc metal chips of 99.995% purity were introduced into the cell and the rate of weight loss determined at various temperatures. The residual pressure in the system was maintained at $\sim 5 \times 10^{-7}$ mm Hg during the measurements. A knife-edged hole of 0.06905 cm^2 area was used. The results are summarized in Table II-7. The Knudsen relation was used to calculate vapor pressures by assuming equilibrium in the cell and monatomic Sc to be the sole vaporizing species. The vapor pressure observed for the first heating is high as a result of sample outgassing. Omitting this point, the rest of the data yield the approximate relation $\log p_{(atm)} = \frac{-1.935 \times 10^{-4}}{T} + 6.63$. The heat of sublimation of Sc, ΔH°_{1600} is calculated as 88.5 kcal/mole from the slope of the log P versus 1/T curve.

Table II-7. Vapor Pressure of Scandium at Several Temperatures

Order of Heating	Temperature, °K	Time, min	Wt loss, grams	Pressure, atm
1	1561	111	0.00955	2.8×10^{-6}
2	1802	46.0	0.10365	7.8×10^{-5}
3	1800	20.5	0.04531	7.6×10^{-5}
4	1532	70.5	0.00207	9.4×10^{-7}
5	1591	93.3	0.00822	2.9×10^{-6}
6	1586	91.4	0.00745	2.6×10^{-6}
7	1482	635	0.00762	3.8×10^{-7}

5. Oxidation Rate of Sc. Chips of Sc of approximately 1 cm^2 surface area were cut from an arc-melted ingot with a chisel. The pieces were oxidized without further treatment by exposing them to static air at various temperatures and recording the weight changes by means of a thermobalance. The results are summarized in Fig. II-12.

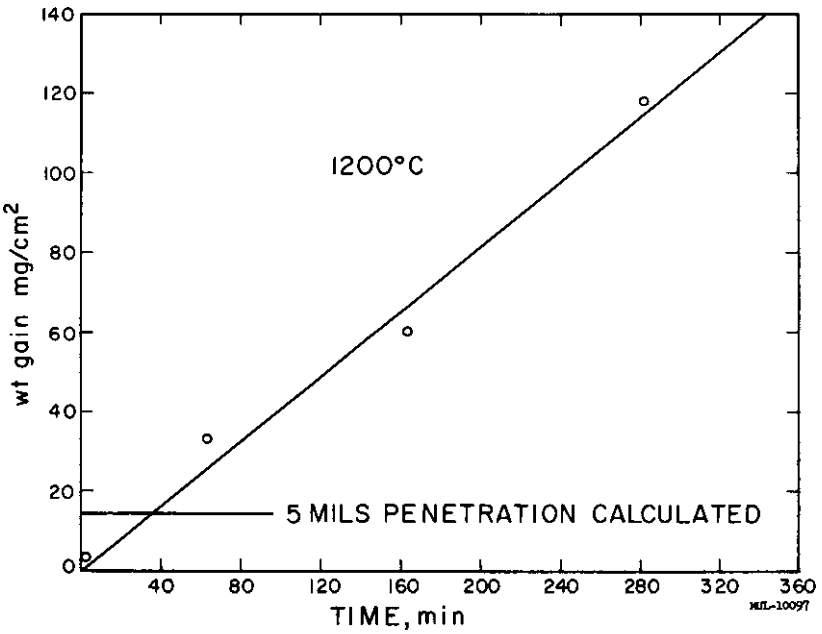

Fig. II-11. Oxidation rate curve (yttrium metal).

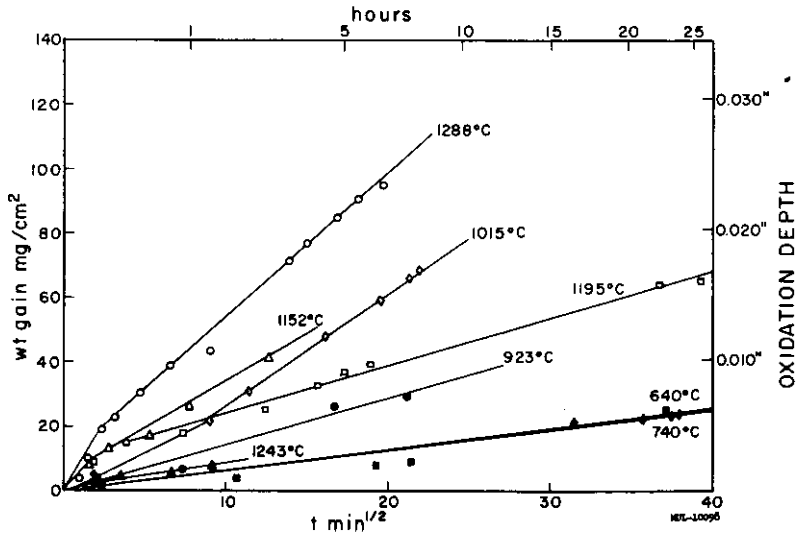

Fig. II-12. Oxidation rate of scandium metal.

It is noted that oxidation proceeds according to a parabolic rate law. The oxidation rate increases with increasing temperature to about 1000°C. A decreasing rate is then noted to about 1250°C. At 1300°C the oxidation rate again increases with increasing temperature. The reason for this strange behavior is not known. Additional studies with better specimens are planned. The oxidation rate of Sc at 1300°C corresponds to a surface penetration of 0.022 in. in 5 hours.

Summary of Studies on Sc. The property measurements on Sc reveal a material that is ductile, high melting, of low density and of outstanding oxidation resistance. Although the mechanical strength is probably low, it is likely that the material can be strengthened by both solution and dispersion hardening agents. If a sufficient quantity of the material were available, it is possible the material could be quite useful, especially in applications where high temperatures and oxidizing conditions prevail, e.g., rocket nozzles and nose cones, airfoil leading edges, etc. A comparison of the properties of several light-weight metals with those of Sc is as follows:

	Al	Be	Ti	Sc
Melting Point, °C	659	1283	1677	1600
Density, g/cm^3	2.70	1.85	4.51	3.00
Thermal Diffusivity				
100°C, $\frac{cal}{cm\text{-}sec\text{-}°C}$	0.90	0.45	0.10	0.12
Hardness				
(Knoop, 500-g load)	30	130	90	70
Oxidation Resistance in Air Temperature for:				
0.010 in. in 10 hrs	>m.p.	800°C	900	1200
0.010 in. in 100 hrs	>m.p.	700	800	700

Preparation of $NbCr_2$

Several hundred grams of the intermetallic $NbCr_2$ were prepared and formed into a sample ingot. It was hoped that this compound would have some of the oxidation resistance of chromium, and in addition be stronger than

either Nb or Cr at elevated temperatures. $NbCr_2$ is reported to melt congruently at ~1710°C.[1]

The compound was prepared by reaction of the powdered elements in a Ta crucible at ~1650°C for 30 minutes at 1/2 atm Ar. The sintered mass was crushed and resintered again at ~1650°C for an additional 30 minutes.

Solid specimens of the compound were prepared by melting and casting in an Al_2O_3 mold. Melting was done under 1/2 atm Ar to suppress Al volatilization. The resulting ingot was quite sound, with only a few small voids, all on the outer surface. Samples were cut from the ingot using an SiC wheel. The compound is hard and very brittle at room temperatures.

An oxidation test on the compound was run at 1150°C in still air. The results are given in Fig. II-13. The sample was heated 6 hours, then removed from the furnace, and the coating removed. Upon being reintroduced into the furnace, the rate of attack was found to be approximately the same as the initial rate.

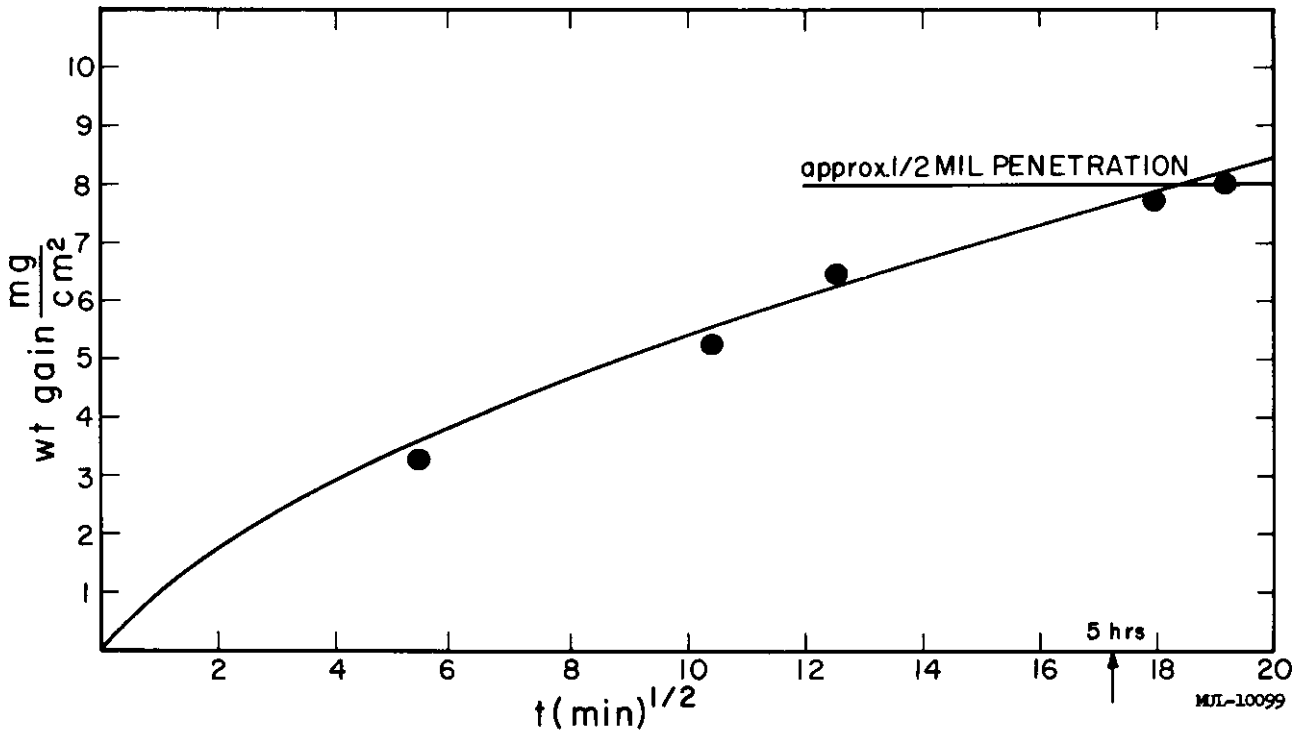

Fig. II-13. Oxidation rate of $NbCr_2$ at 1150°C in static air.

[1] Hansen, M. and Anderko, K., "Constitution of Binary Alloys", McGraw-Hill Book Company, New York, N.Y., 1958, p. 541.

In view of the rather poor oxidation resistance, it does not appear that $NbCr_2$ is a promising material for use in the Tory II-C reactor. Further work on the properties will be done, however.

Aluminide Coatings on 90% Ta-10% W Alloy

The performance of six more aluminide coated pieces of 90Ta-10W alloy is presented in Figs. II-14 and II-15. The method of applying the coat is described in previous reports. Coats of 1-2 mils aluminide (10-20 mg Al/cm^2) were applied and the pieces tested in gently moving air or O_2 at 1250°C. Testing was discontinued at the first visible sign of a flaw.

From the data the following facts are apparent: There is little difference in the rate of attack whether in air or oxygen. During the initial heating the weight gain varies widely from piece to piece, due to the difference in the amount of free Al left on the surface by the coating process. After the free Al has oxidized, the attack proceeds according to a parabolic rate law, at a rate comparable to the rate of attack on pure $TaAl_3$. Flaws appear in the coat – usually at edges or corners – at times much shorter than would be expected from the average coating thickness and the rate of oxidation of the coat. Whether failure occurs from a "thin spot" or defect in the coat, or from the inward diffusion of Al is not known.

The coatings are said to have failed when the first visible attack is noted. It should be emphasized that the appearance of the first flaw does not really represent failure in a mechanical sense. In no case was a flaw observed which was sufficiently severe to threaten the integrity of a structural piece. Testing beyond the point at which flaws first appear was not done, however, since it was felt that the rate at which the flaw "worsens" will be highly dependent upon the environment. Thus still air tests are of little use when the intended application involves high velocity air flow.

No further laboratory scale work on this alloy is contemplated. It is felt that the uncoated material is itself not sufficiently oxidation resistant, and since more resistant alloys are becoming available, it is wise to concentrate on coating only such alloys which are themselves quite resistant. A most important characteristic of a coated piece is that any flaw which develops in the coat should not lead rapidly to a catastrophic failure in the piece, that is, coats should be to some extent "self-healing". It has been observed that pure Ta is catastrophically attacked as soon as the coating fails; the resulting oxidation actually "lifts" the coat from the surface around

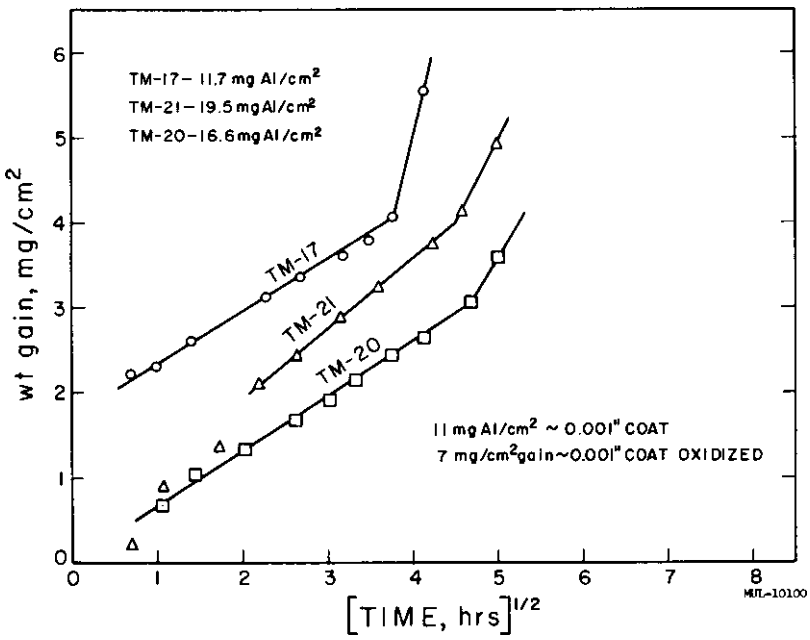

Fig. II-14. Oxidation rate of aluminide coated alloy, 90% Ta-10% W, 1250 ± 5°C (gently flowing O_2).

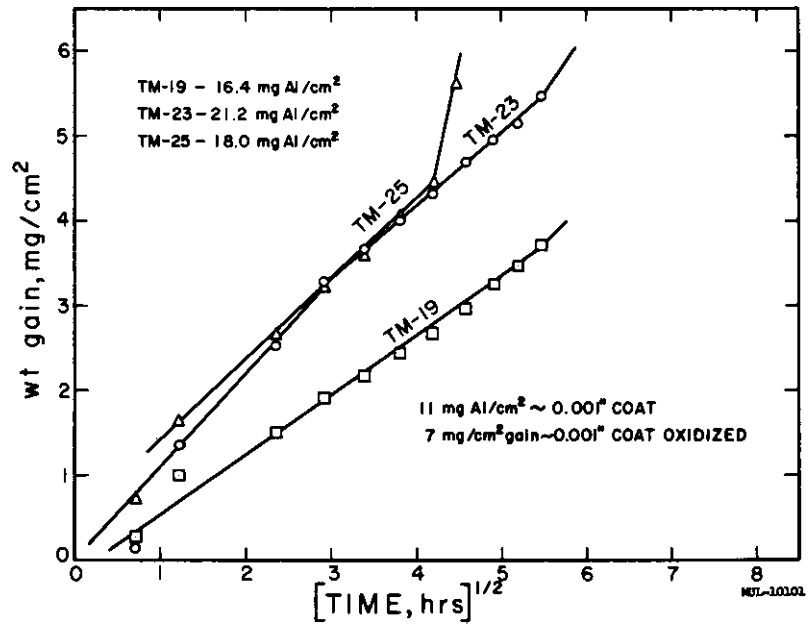

Fig. II-15. Oxidation rate of aluminide coated alloy, 90% Ta-10% W, 1250 ± 5°C (gently flowing air).

the initial flaw, and failure spreads rapidly. The 90-10 Ta-W alloy is much less drastically affected than pure Ta, but flaws are observed to worsen steadily once attack has started.

It seems reasonable that the most oxidation resistant base material should be the one which receives the preference on coating development. Further coating studies will therefore be concentrated on the most oxidation resistant of the Nb or Ta base alloys.

Aluminide Coatings on Fansteel 82

One of the few Nb base alloys available in quantity is Fansteel 82, an alloy containing 66 wt% Nb, 33% Ta and 0.75% Zr. Although the high temperature oxidation resistance of the uncoated material is not particularly good, it is of interest to see if aluminide coatings would offer sufficient protection to be useful. For this purpose four specimens were coated by the usual melt-and-flow method which has been described in previous reports.

The application of the coatings to this alloy seemed to be exceptionally simple. The coatings were smooth, adherent, and in general flaw free. Four specimens so coated were exposed to gently moving air at 1250°C for periods of 13, 10, 6 and 4 hours, then examined, with the following results:

82-1. A simple block-shape coated with 23.1 mg Al/cm^2. After 13 hours of testing in air the piece had gained 5.7 mg/cm^2. Although attack was localized at several points, the failure at these points could not be said to be drastic; in fact the mechanical integrity of the piece was judged to be unimpaired.

82-2. A plate 0.53 cm thick containing two 0.53-cm-diam holes. The coating was again very easily applied, and the inside surfaces of the holes were completely coated. The coating thickness was only 7.9 mg Al/cm^2. After 10 hours testing the sample had gained 3.4 mg/cm^2. Again most of the weight gain was localized at a few points. The coat had in no sense failed, however, and the Nb beneath the coat had not been embrittled by oxygen penetration.

82-3. A plate 0.63 cm thick, containing five 0.49-cm-diam holes drilled through. The coating again went on very smoothly, covering the entire surface without flaws. The thickness of the coat was 11.5 mg/cm^2, or ~0.001 in. After 6 hours at 1250°C in air the piece had gained only 0.94 mg/cm^2. No points of attack were visible. The metal beneath the coat was unattacked.

82-4. A plate 0.63 cm thick, containing 9 holes of 0.35-cm-diam drilled through. The coat again went on very smoothly, and totaled 7 mg Al/cm^2. After 4 hours at 1250°C the piece was virtually unchanged in appearance.

In conclusion, it seems that for short time applications, the use of pure aluminide coatings on FS-82 is quite feasible. It would certainly be necessary, however, to test such coatings thoroughly in rapidly moving air. In addition, the capability of producing numbers of large, intricately shaped pieces of predictable behavior can only be established by a detailed development program.

More important than the somewhat limited success of the coats on FS-82 is the emergence of the fact that a Nb-Ta alloy has proven to be quite compatible with the aluminide coat. Since such alloys with greater oxidation resistance than FS-82 are currently being developed, it is to be hoped that coating the most oxidation resistant of the new alloys will prove possible.

Platinum Coatings on Molybdenum

Studies have continued on the use of Pt as a possible coating material for Mo. The method used to apply the coats is to first bring Pt foil into intimate physical contact with a smooth, clean Mo surface by pressing in a molding die. Subsequent to this, the mechanically clad piece is placed on a three-point Ta stand and heated carefully in vacuo to the fusion point of Pt.

It has been found that discs so coated with 0.001-in. Pt foil are not completely protected when heated in air at 1200°C, although the coat appears to be continuous. The most likely explanation for failure is that excessive grain growth takes place in the Pt skin, both during the application of the coat and in subsequent testing. Oxidation at the grain boundaries then results.

To see if successive coats would cover the flaws, the procedure of application was modified to apply several successive coats. Coats applied in this manner were considerably better than those applied in a one-step operation. It was found that the attack on the pieces could be represented by the equation:

$$\Delta w = kt^{3/2}$$

where Δw is % wt lost or $\frac{(\text{wt loss} \times 100)}{\text{initial wt}}$, k is a constant, and t is time in minutes.

In Table II-8 are given the values of k for one-step and two-step applications of foil.

Table II-8. Rate of Attack on Pt-Coated Mo, Tested in Air at 1200°C

Sample	k	Comments on Coating	Comments on Testing
Mo-49	5.1×10^{-3}	Single layer of 0.001" foil	Pinholes on all surfaces
Mo-51	1.6×10^{-3}	Four successive coats of 0.0025" foil	Pinholes on all surfaces
Mo-53	9×10^{-2}	Single layer of 0.001" foil. Diffused in 19 hr at 1600°C	Badly attacked on one surface
Mo-55	9.2×10^{-7}	Same as Mo-53; Two coats applied	Initial attack followed linear rate law, then went over to $t^{3/2}$ law

The data indicate the two-coat, long-diffusion-time process to be superior to the one-step procedure. At present difficulties are being encountered at the points where the piece rests on the Ta support. Al_2O_3 will be used in future experiments.

Water Vapor Resistant Coatings on BeO

The work reported here is in continuation of a program to develop coatings to protect BeO against attack by water vapor at high temperatures. Al_2O_3 was tried as the coating material on unfueled, thin-walled BeO tubes with a surface to volume ratio of about 21 cm^{-1}. Tests were conducted at 1490-1508°C in water vapor diluted with air to a partial pressure of 0.45-0.5 atm. The test times were between 1.75 and 2.0 hr, and the flow rate about 350 liters/hr. In Table II-9, which gives numerical results, R is the ratio of the loss rate of a coated sample to that of an uncoated check sample tested simultaneously.

The coatings looked mechanically strong and dense, with low porosity except at thick spots formed during the dip-coating step. However, they gave little protection to the BeO; the lowest R value is 0.81, quite close to those reported last quarter for $Si\text{-}ZrO_2$ and $MgO\text{-}ZrO_2$ coatings on unfueled samples. The appearance of samples after test suggests that the coating was not strongly bonded to the BeO. It is planned to try the effect of longer

firing times and higher temperatures, since these would be expected to increase the extent of reaction between the BeO and the Al_2O_3.

Table II-9. Water Vapor Attack on Al_2O_3 Coated BeO

	Firing Conditions			Results of Testing		
Sample	Time, min	Temp, °C	Pressure	Wt loss, g	Loss Rate, %/hr	Ratio R
92-10	93	1804	1 atm	0.0145	1.06	0.81
92-7	24	1800	0.1 micron	0.0176	1.17	0.93
92-9	40	1816	0.1 micron	0.0188	1.43	0.89

Beryllide Sintering Studies

Specimens of Nb_2Be_{17}, $NbBe_{12}$, Ta_2Be_{17} and $TaBe_{12}$ were compacted by isostatically pressing -200 mesh powders at 20,000 psi. Densities were approximately 70% of theoretical and green strength was good. The specimens were sintered by heating under argon in Ta crucibles. The following heating conditions were used:

For Nb_2Be_{17}, 1 hour at 1630°C produced a density of 99% theoretical. Fifteen minutes at 1600°C resulted in a density of 94% theoretical. For $NbBe_{12}$ it was necessary to exceed the peritectic temperature to promote sintering. Heating for a short time to 1675°C produced a specimen that appeared to be dense, although density measurements have not yet been made. For Ta_2Be_{17}, an attempt to densify the material at 1650°C was unsuccessful. At about 1700°C, the crucible was attacked and melting resulted. For $TaBe_{12}$, 30 minutes at 1670°C produced a specimen that was 85% of theoretical density.

Oxidation Resistance of $MoSi_2$

It has been observed that $MoSi_2$ loses its oxidation resistance when subjected to prolonged sintering. A likely reason for this would be that the $MoSi_2$ phase becomes depleted in Si due to loss by vaporization; the Si-poor phase is then attacked.

To check this hypothesis, pellets of $MoSi_2$ were pressed and sintered under various conditions of temperature, time and atmosphere. A small portion of each pellet was then analyzed by x-ray diffraction, the remainder tested in air at elevated temperatures.

The results show that when Si was lost from the pellets, the pellet most depleted in Si had the poorest oxidation resistance. Pellets which had lost no Si were unaffected when tested in air.

It is therefore mandatory in any process which is to protect Mo from oxidation through the formation of a $MoSi_2$ coat, that sufficient Si remain on the surface to form Si-rich $MoSi_2$.

Thermal Diffusivity Measurements

In the previous quarterly report, a method was described for measuring thermal diffusivities. In the method one end of a sample rod is brought into contact with an isothermal heat source and the temperature rise at the opposite end is measured as a function of time. The heat flow equation describing the temperature rise at the cold end of the specimen for the case where radiation losses are negligible is:

$$\frac{T - T_i}{T_h - T_i} = 1 \frac{-4}{\pi} \sum_{n=0}^{n=\infty} \frac{(-1)^n}{2n+1} \exp\left[(2n+1)^2 \left(-\frac{\alpha \pi^2 t}{4L^2}\right)\right]$$

where T = temperature at cold end as function of time, °K

T_i = initial sample temperature, °K

T_h = heat source temperature, °K

α = thermal diffusivity in cm^2/sec

t = time in seconds

L = sample length in cm

In practice it is found that the heat flow equation works well for good thermal conductors such as Cu and Al. For poorer conductors, however, radiation removes a significant amount of the available heat and the "level off" temperature at the cold end lies below the heat source temperature. An exact mathematical solution to correct for radiation losses is believed to be impossible. Therefore, in order to correct for radiation, it is assumed that the shape of the temperature-time curve is independent of "level off" temperature. Hence, the time required to reach a certain fraction of "level off" should be indicative of the thermal diffusivity. Fixing a value of $(T - T_i)/(T_h - T_i)$ in turn fixes the exponent in the heat flow equation so that $\alpha t/L^2$ is constant. This relationship was checked for several metals of known purity and thermal diffusivity, and the data are presented in Table II-10. The heat source was set at 240°C and the initial sample temperature

at 40°C for these measurements. The time required for the temperature at the cold end to rise from 10 to 50 percent of "level off" was designated as Δt. A plot of known values of α versus $1/\Delta t$ gives the required straight-line relationship (Fig. II-16). This curve may now be used as a standard for obtaining α's from Δt's for other materials.

An additional difficulty noted in these measurements was a localized cooling of the heat source surface when the sample initially made contact. This was especially noticeable in the case of Al, and was present to a lesser degree for W and Mo. The difficulty was overcome by reducing sample diameters to 0.5 cm or less.

Thermal diffusivity measurements were run on various materials at an average specimen temperature of ~145°C. The data are presented in Table II-11. It is noteworthy that for high-purity Fe, Ni and Cu, the thermal diffusivities are considerably higher than those reported previously for lower purity materials.

Measurements were also run on a 90% theoretical density Al_2O_3 as a function of temperature. The results are given in Fig. II-17. The temperature coefficient of thermal diffusivity is in agreement with literature values, although the absolute values differ.[1]

[1] Campbell, I.E., High Temperature Technology, p. 51, Wiley, N.Y., 1956.

Table II-10. Thermal Diffusivity Standards at ~145°C

Material	Purity	K	C_p	ρ	Δt	1/Δt	α	L	d	W
Zr	Iodide Process Crystal Bar	0.048	0.0703	6.49	54.9	0.01821	0.105	3.39	0.95	6.1088
Fe	Armco	0.155	0.1179	8.22	35.40	0.0283	0.168	3.62	0.62	8.9641
Ni	"A" Nickel	0.188	0.1171	8.825	28.05	0.03562	0.182	3.81	0.40	4.1189
Ta	99.9%	0.126	0.0348	16.68	24.82	0.04025	0.217	3.48	0.92	41.5201
Mo	99.9%	0.355	0.0645	10.05	9.66	0.1034	0.548	3.41	0.46	6.2237
W	99.9%	0.364	0.0328	19.2	8.87	0.1129	0.575	3.26	0.49	10.6713
Al	99.99%	0.540	0.2289	2.71	5.82	0.1722	0.870	3.47	0.60	2.9130

Definition of symbols:
K = Thermal conductivity, cal/cm-sec-°C = $\alpha C_p \rho$
C_p = Heat capacity, cal/g-°C
ρ = Measured density, g/cm^3
Δt = time (sec) to go from 10 to 50 percent of temperature interval between initial and "level off" temperatures
α = Thermal diffusivity, cm^2/sec
L = sample length, cm
d = sample diameter, cm
W = sample weight, g

Table II-11. Thermal Diffusivities at ~145°C

Material	Purity %	K	C_p	ρ	Δt	1/Δt	α	L	d	W
Sc	99.99	0.0485	0.1369	3.008	46.4	0.02154	0.118	3.50	0.95	7.4816
Y	99.9	0.06025	0.0692	4.44	32.8	0.0359	0.196	3.42	0.91	4.44
Ti	99.9	0.07075	0.1337	5.17	53.25	0.01878	0.1025	3.44	0.80	8.942
V	99.7	0.0485	0.1232	7.84	57.7	0.01734	0.096	3.22	0.75	7.84
Nb	99.5	0.104	0.0617	8.54	27.9	0.0359	0.197	3.40	0.90	21.054
Fe	99.999	0.375	0.1179	7.86	12.64	0.0790	0.405	3.58	0.501	5.568
Ni	99.999	0.242	0.1171	8.87	23.55	0.0425	0.233	3.58	0.502	6.292
Cu	99.999	0.901	0.0949	8.94	4.75	0.2104	1.076	3.80	0.396	4.213
Al_2O_3	99.8	0.0630	0.2350	3.56	72.0	0.01389	0.0753	3.30	0.92	8.715
$NbAl_3$	97	0.04725	0.1413	3.713	60.2	0.01662	0.0925	3.55	1.22	3.713
$NbBe_9$	99	0.1225	0.2643	4.31	51.9	0.01929	0.1075	2.44	0.85	4.31
$MoSi_2$	99	0.1130	0.1105	5.50	29.89	0.03347	0.186	3.50	0.52	5.50

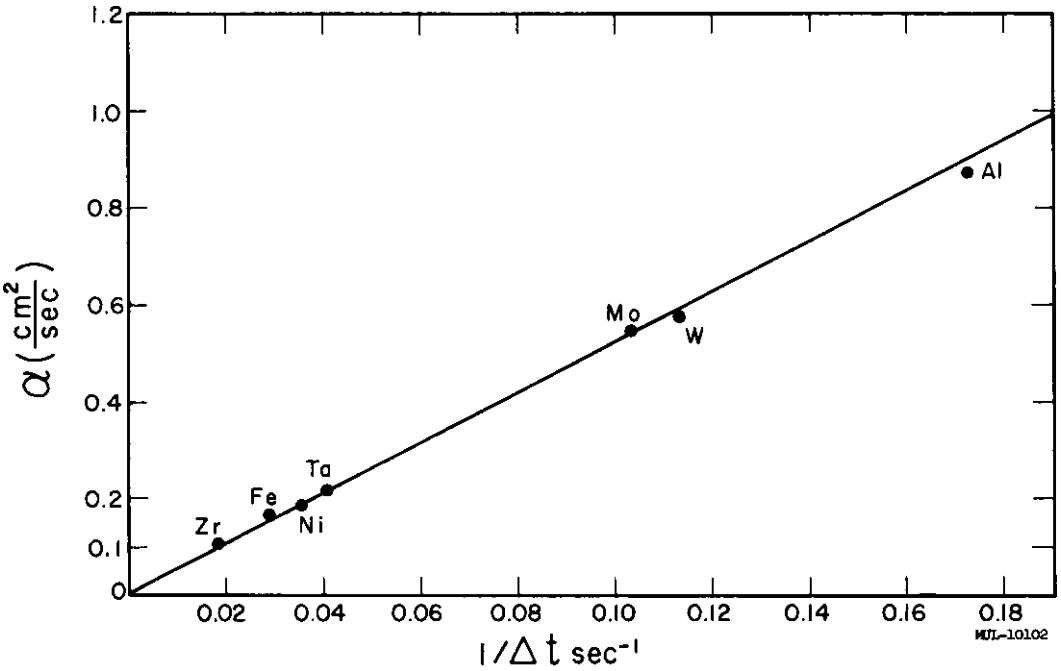

Fig. II-16. Thermal diffusivity vs $1/\Delta t$.

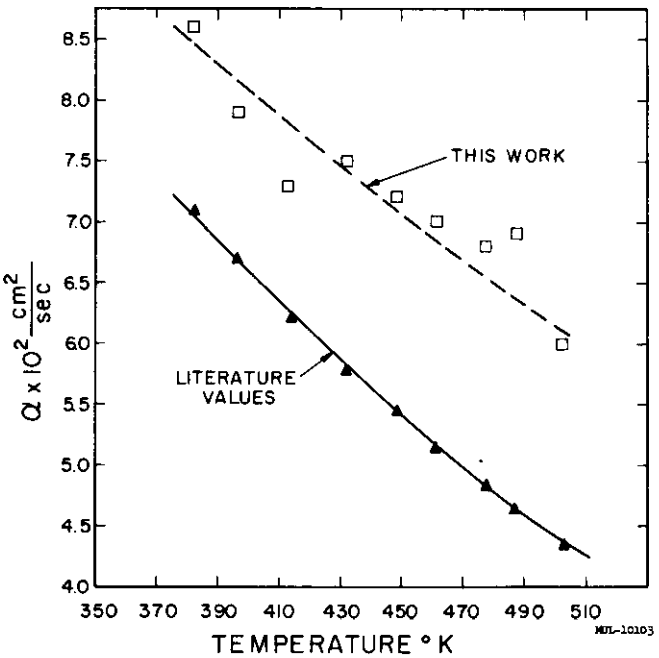

Fig. II-17. Variation of thermal diffusivity of Al_2O_3 with temperature.

RADIOCHEMISTRY

Fission Product Escape from Pluto-Type Fuel Elements

The escape of fission products from Pluto-type fuel elements is being studied further. The data appearing in the tables below were obtained from cylindrical tubes of 90% BeO-10% UO_2, at least 99.5% theoretical density, 2.54 cm long, 0.86 cm o.d., 0.60 cm i.d.

Table II-12. Fractional Losses in 5-1/2 Hours

Nuclide Measured	Temperature in °C				
	1500	1450	1400	1300	1225
Y^{91}	3×10^{-6}	----	----	----	----
Zr^{95}	5×10^{-6}	----	----	----	----
Mo^{99}	0.16	0.040	0.027	0.0014	6.6×10^{-4}
Te^{132}	0.040	0.033	0.014	0.0018	0.0013
I^{131}	0.034	0.022	0.012	0.001	6×10^{-4}
$Cs^{136,7}$	0.020	0.020	0.014	0.004	0.002
Ba^{140}	8×10^{-6}	6×10^{-6}	4×10^{-6}	8×10^{-6}	3×10^{-6}
$Ce^{141,4}$	1.5×10^{-3}	3.6×10^{-4}	1.4×10^{-4}	5×10^{-5}	3×10^{-5}
Nd^{147}	9×10^{-5}				

Table II-13. Ranges of Fission Fragments in 90% BeO-10% UO_2

Nuclide	mg/cm^2	Microns
Mo^{99}	3.9	12
Te^{132}	3.2	9.9
I^{131}	3.2	9.9
Cs^{136}	3.1	8.0
Cs^{137}	3.0	9.3
Ba^{140}	2.9	8.9
Ce^{141}	2.9	8.9
Ce^{144}	2.8	8.6

The escape data are reproducible to only about a factor of two; the discrepancy is most likely due to slight differences in the material as fabricated. The reproducibility of the range data has not been determined yet.

CHAPTER III. TORY II-C

SECTION I. PERFORMANCE CHOICE

The Tory II-C reactor has been defined as a reactor which will propel a missile with a reasonable payload. Even with the present undefined state of the airframe and the many unknowns yet connected with the reactor the choice of a size and performance for the reactor must be made so that the reactor design can proceed and follow through to testing without changes in the major parameters. An adequate margin of safety must be left in the design so that reasonable errors in assumptions will still leave enough thrust for the missile.

IDEAL REACTOR PERFORMANCE

These basic ground rules have been established and were inputs for a base thrust coefficient problem.

1. The maximum missile diameter will occur at the reactor, since to do otherwise is to lose performance. The distance from the reflector outer boundary to the outside of the missile skin will be 1-1/4 in. maximum in the hot condition. Reducing this by 1/2 in. increases the thrust coefficient by 3-1/2%.

2. The reactor critical mass will be 100 kg or less. A further increase in critical mass buys very little in performance and does not warrant the increased cost and increased difficulty of fabricating the fuel elements.

3. The design wall temperature will be 2500°F which implies about 2600°F maximum interior temperature. With the present LRL BeO the material could run at 2800°F without incurring serious loss of fuel. However, water vapor attack would be serious at temperatures above 2500°F. It is expected that means to inhibit water vapor attack will be developed.

Also average conditions of humidity would not seriously disturb the reactor for typical missions. However, for the present time the water vapor problem will be allowed to limit the temperature. An increase in wall temperature of 200°F increases the thrust coefficient 14%.

4. The thrust coefficient will be computed for a design at Mach No. 2.8 at 1000-ft altitude and for an ambient temperature of 100°F. The thrust coefficient is increased by 1.6% per 10°F decrease in ambient temperature. A design at Mach 3.0 increases the thrust coefficient 7%.

5. The BeO moderator will be assumed to be 96% of theoretical density. It is expected that 99+% material will be achieved resulting in a 3% thrust increase.

6. A 20% thrust margin will be allowed for maneuvers and velocity changes. This is not to be confused with a safety factor.

7. The diffuser pressure recovery will be 80% with a 4% bleed with 80% recovery of the bleed. This is reasonable performance for present day diffusers.

8. A nozzle divergence factor of 0.98 and a nozzle velocity coefficient of 0.97 will be used.

9. The core will be 51.2 in. (130 cm) in length with a 7 in. front reflector and a 2 in. rear reflector. The core length has little effect on the thrust coefficient.

10. The reactor exit Mach No. will be 0.5. This has been found to give near optimum thrust coefficients for the reflected system.

11. The external missile drag coefficient will be taken to be 0.140 based on the maximum missile diameter. This drag coefficient is the result of an analysis of the three airframe manufacturers' reports together with an LRL study. With the 20% maneuver allowance the drag coefficient becomes 0.168.

12. The missile will have to fly for 10 hours. However, only 3 hours at the hot day, 1000-ft altitude conditions will be required.

The base thrust coefficient problem used the following inputs:

Pressure recovery	-	80%
Max wall temp	-	2500°F
Core length	-	130 cm with 7" forward and 2" rear reflectors
Radial power	-	Flat
Axial power	-	3/4-1/4 sine in core
Nozzle	-	0.98 divergence, 0.97 vel coeff
Mach No.	-	2.8
Ambient temp	-	100°F (hot day)
Altitude	-	1000 ft
Exit Mach No.	-	0.5

The base thrust coefficient for an "ideal" reactor as a function of porosity is given in Fig. III-1.

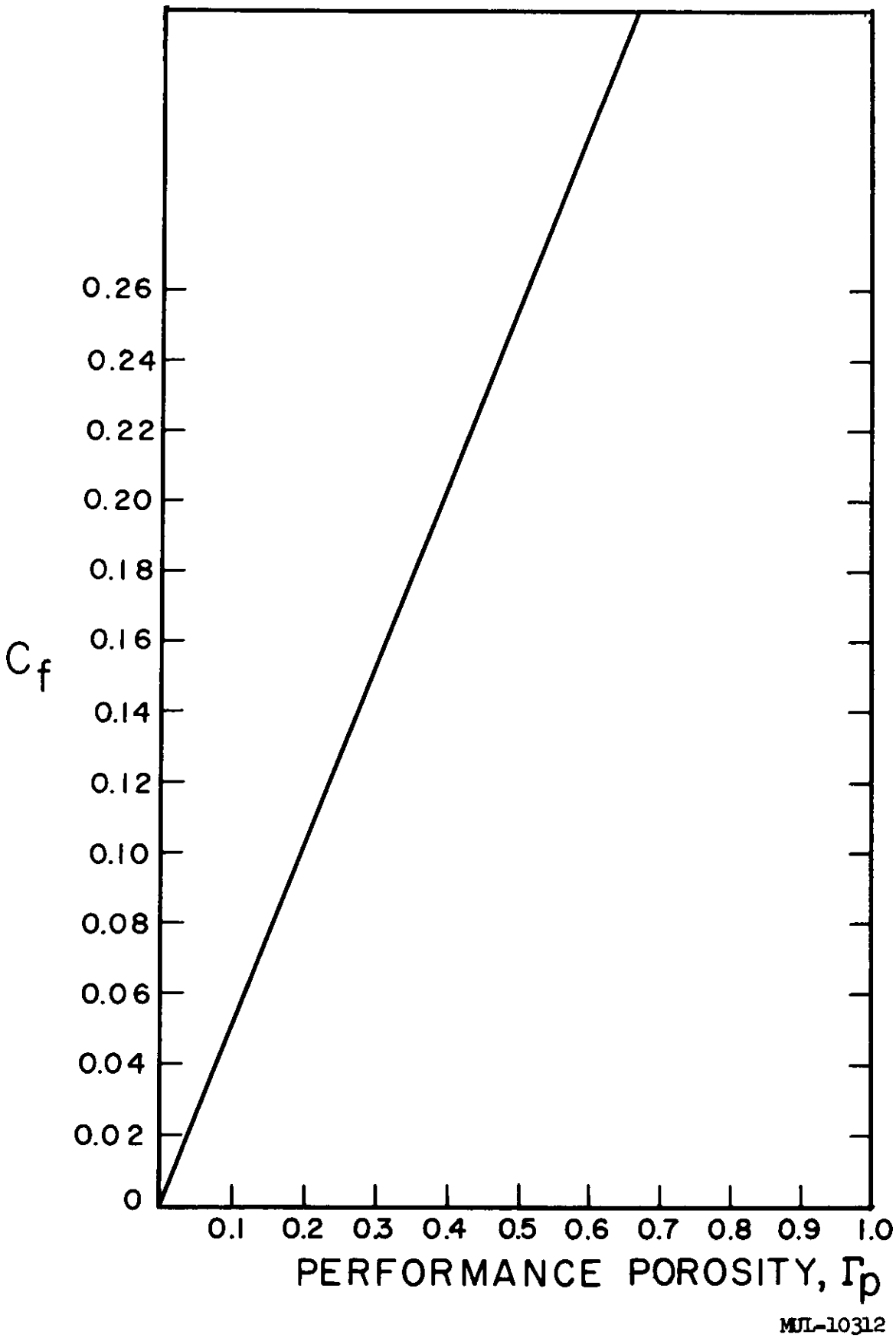

Fig. III-1. Ideal reactor. Base thrust coefficient vs performance porosity.

The following perturbations were made on the base thrust coefficient problem:

	Thrust Coefficient Gain or Loss %	Possible Error	
1. Boundary layer bleed 4% at 80% recovery	- 4.0	+ 0.0	- 1.0
2. Entrance losses 0.4% in pressure (some tapering of entrance assumed)	- 0.7	+ 0.3	- 0.4
3. Misalignment of air flow tubes (7 offsets of 10 mils per passage)	- 3.0	+ 2.0	- 1.0
4. Tube exit losses (1% loss in pressure, some tapering assumed)	- 1.0	+ 0.2	- 1.0
5. Error in friction factor used	0	0	- 4.0
6. Error in entrance heat transfer coefficient	0	+ 1.0	- 0
7. Side reflector cooling (3" reflector, 1.2% reactor power)	0	+ 1.0	- 0
8. Axial power distribution (Flat through first half of reactor)	+ 2.0	0.0	- 2.0
9. Radial power distribution (5% of material area lower than peak by 135°C)	- 1.0	+ 0.5	- 1.0
10. γ-ray heating in front and rear reflectors (0.3% of reactor power deposited)	+ 0.1	+ 0.1	- 0.1
11. Power depression due to rods	- 1.0	+ 0.5	- 0.5
12. Power for electronics and refrigeration (can use boundary layer bleed air)	0	+ 0	- 0.5
Total	- 8.6	+ 5.6	- 11.5

The base thrust coefficient should thus be decreased by 8.6% with the possible errors shown. The errors have been added algebraically which of course is improper and magnifies them considerably. However, they are so poorly known that better treatment is not justified.

The following increases in thrust coefficient will almost surely be achieved and can be considered as part of the safety factor.

1.	86% pressure recovery at 10% bleed	+ 3.6
2.	Mach 3 design	+ 7.0
3.	99% BeO density	+ 3.0
4.	Increase in temperature of 200°F	+ 14.0
5.	Reduction of missile diameter by 1"	+ 3.5
	Total	+ 31.1%

REAL REACTOR PERFORMANCE

The performance of three different Tory II-C reactor designs were considered. These were described in Progress Report No. 2 (UCRL-5829) and will be called here by the names:

1. Dome
2. Integral
3. Tray

These designs have different structural cooling requirements and different structural space losses in the core. The percent core area affected is given below:

	Dome	Integral	Tray
1. Metal area	0	0.34	1.4
2. Incidental void (packing)	1.0	1.0	1.0
3. Control rod void	1.6	1.6	1.6
4. Structural cooling void	0	2.3	4.1
Area lost (percent)	2.6	5.2	8.1

The thrust penalties (in % of thrust coefficient) associated with mechanical design are given below for each reactor:

	Dome	Integral	Tray
1. Structural cooling	0	+ 1.5	+ 3.0
2. Reactor exit losses	- 5.0	0	0
Total	- 5.0	+ 1.5	+ 3.0

In addition, thrust penalties are incurred for a given critical mass by the effect of absorbers. In the criticality calculations the following ground rules were applied generally. Results are given in Table III-1.

1. Radial reflector 3 in. thick of 96% dense BeO with 5% porosity and at core temperature.

2. Core BeO of 96% density. Volume taken by UO_2 is allowed for.

3. All dimensions and criticality calculations are for the reactor at 2600°F.

4. Critical mass is given in kilograms of UO_2 with the uranium in the form of oralloy. Two cases are computed: One for a critical mass of 50 kg, the second for 100 kg.

5. Reactor length is 51 in.

6. The cross sections used for Mo and R-235 are as determined from LRL criticality experiments.

7. No effort to flatten power was made.

8. No end reflectors were used.

9. The BeO was considered homogeneous (i.e., no streaming allowance).

10. The reduction in critical mass by the addition of the end reflectors is offset by the increase in critical mass due to power flattening, control rods streaming and other effects.

Table III-1

D_C	M_C	Γ_{CR}	Γ_F	Γ_P	C_f	C_f'
			Dome			
40	50	53.5	50.9	34.6	See Fig. III-1	0.152
	100	56.0	53.4	36.4		.160
48	50	57.2	54.6	39.4		.171
	100	60.0	57.4	41.5		.181
56	50	59.2	56.6	42.6		.187
	100	62.5	59.9	45.1		.197
64	50	60.3	57.7	45.0		.197
	100	64.2	61.6	48.1		.211
			Integral			
40	50	51.2	46.0	31.3	See Fig. III-1	0.147
	100	54.4	49.2	33.5		.158
48	50	54.2	49.0	35.4		.166
	100	57.5	52.3	37.9		.178

(continued)

Table III-1 (continued)

D_C	M_C	Γ_{CR}	Γ_F	Γ_P	C_f	C_f'
			Integral (continued)			
56	50	55.8	50.6	35.2	See Fig. III-1	0.179
	100	59.8	54.6	41.1		.193
64	50	56.7	51.5	40.2		.189
	100	61.1	55.9	43.4		.204
			Tray			
40	50	46.5	38.4	26.1	See Fig. III-1	0.125
	100	51.9	43.8	29.8		.143
48	50	49.1	41.0	29.6		.141
	100	54.1	46.0	33.2		.159
56	50	50.3	42.2	31.8		.152
	100	56.4	48.3	36.5		.175
64	50	50.6	42.5	33.0		.158
	100	56.4	48.3	37.5		.180

Symbols used:

D_C = Core diameter, inches

M_C = Critical mass, kg of UO_2

$\Gamma_{CR} = \dfrac{\text{Void area in core + area of core heat transfer holes}}{\text{Gross area of core}}$

$\Gamma_F = \dfrac{\text{Area of heat transfer hole}}{\text{Gross area of fuel element}}$

$\Gamma_P = \dfrac{\text{Area of core heat transfer holes}}{\text{Area of core + area of (3" reflector + 1-1/4") annulus}}$

C_f = Ideal reactor thrust coefficient

C_f' = C_f corrected for perturbations in ideal reactor and thrust penalties associated with reactor mechanical design

The thrust coefficient versus the reactor diameter is plotted in Fig. III-2 for a 50-kg critical mass and in Fig. III-3 for a 100-kg critical mass. The Tray design is marginal even for the 100-kg crit, while the Dome and Integral reactors are very similar in performance.

A 54-in.-diam reactor has an excess thrust of 7% for the 100-kg crit which would be an adequate margin with the potential increases of 31.1% in

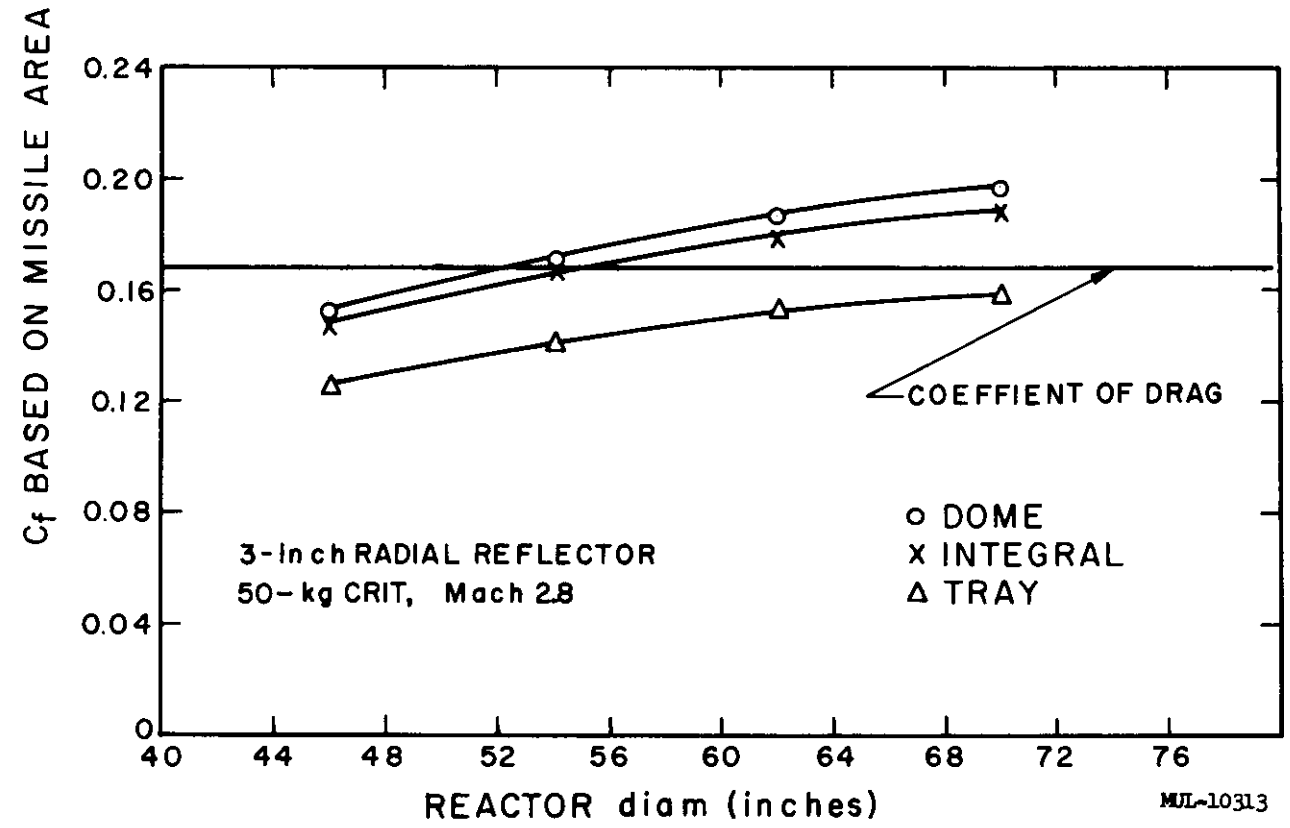

Fig. III-2.

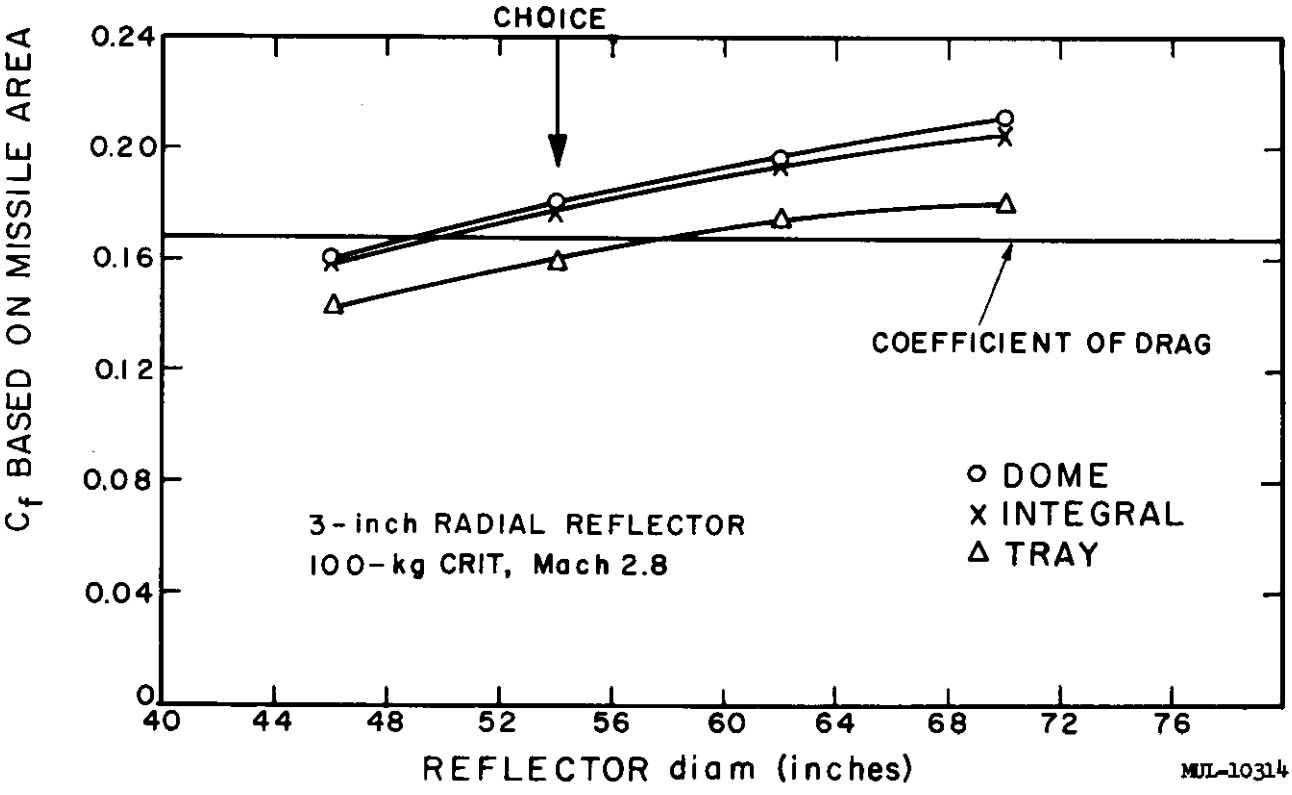

Fig. III-3.

thrust coefficient discussed earlier. By going to 60 in. an increase in thrust coefficient of 7% would result. However, this does not seem to be an adequate gain for the 25% increase in air flow and reactor materials that go along with this size increase. Also, a small missile will have the advantages of reduced booster size and fewer difficulties in making the system mobile. A definite requirement for the missile is that it have an adequate payload compartment. The 56-1/2-in. -diam missile has an adequate payload compartment, and the 54-in. -diam reactor (critical mass 100 kg) will propel the missile; thus the Tory II-C reactor development will be based on a 48-in. core and a 3-in. side reflector.

REACTOR CHOICE

The foregoing considerations of performance and state-of-technology consistent with Pluto Program schedules requires that primary development emphasis be placed on the front supported (Integral) reactor. This reactor will hereafter be referred to as Tory II-C-1. Development of the Dome reactor (hereafter referred to as Tory II-C-2) is being continued on a reduced effort basis. The Tory II-C-2 reactor will provide a backup design and can also accomodate future increased operating requirements.

SECTION II. AERODYNAMIC CHARACTERISTICS

The aerodynamic characteristics and pertinent reactor parameters upon which development of the Tory II-C-1 reactor is proceeding is given in Table III-2. At the design point, the diffuser is operating critical and at Mach 3 the diffuser is operating supercritical.

Optimization of fuel element parameters is based on design-point operation assuming:

a. Fixed nozzle throat area.

b. Expansion ratio variable such that air exhaust pressure always equals atmospheric pressure.

c. Velocity coefficient = 0.97

d. Divergence factor = 0.98

For design-point operation, the effect on the thrust coefficient of varying the fuel element exit Mach number is shown in Fig. III-4.

Figure III-5 presents the results of a first attempt at off-design performance analysis. When the diffuser is operating supercritical, the system is flow limited; hence, the thrust coefficient decreases for Mach numbers greater than 2.8 (hot day, 1000-ft altitude). For Mach numbers less than 2.8, the system becomes pressure limited and performance suffers accordingly. As shown in Fig. III-5, the performance curve for subdesign Mach numbers is incorrect, for losses due to flow spillage have not been included. The net result of this correction reduces the Mach margin. In addition, the drag coefficient, C_D, has been assumed to be constant. In truth, C_D will increase as the flight Mach number is decreased. This in turn will tend to lower the Mach margin.

As shown in Fig. III-5, Mach 3 operation with a 2500°F maximum wall temperature would not be possible with the present configuration (hot day, 1000 ft). Since some of the base parameters cannot yet be firmly fixed, it appears reasonable to assume a Mach limit of 3.0 for the device. The reactor structural limit is now established by this Mach limit. Since a great amount of effort will be expended on structural design of the reactor, an early specification of the structural loading limit is required. The aerodynamic loading of the reactor shall not exceed, under any circumstances, that which is present in the flight conditions listed under critical operation in Table III-2.

Table III-2. Parameters for a Uniform Reactor at 2500°F

	Diffuser Mode	
	Critical	Super-critical
Missile Mach No.	2.8	3.0
Altitude, ft above sea level	1000	1000
Ambient temperature, °F	100	100
Diffuser angle of attack, deg.	0	
Diffuser pressure recovery, %	80	
Bleed fraction, %	4	
Momentum recovery of bleed, %	80	
Supersonic spillage	0	
Maximum fuel element wall temperature, °F	2500	2500
Power distribution	Fig. III-5	
Core diam, in.	48.0	
Reactor diam, in.	54.0	
Missile diam, in.	56.5	
Core length, in.	51.2	
Forward reflector thickness, in.	7.0	
Aft reflector thickness, in.	2.0	
Fuel element porosity, %	52.3	
Side reflector porosity, %	2.6	
Structural cooling void, %	2.3	
Control rod cooling void, %	0.8	
Average volumetric power density, Mw/ft^3 (including end reflector volumes)	9.03	8.95
Maximum volumetric power density, Mw/ft^3	13.73	13.60
Maximum fuel element power density, Mw/ft^3	28.8	28.6
Fuel element hole radius, in.	0.0942	0.0942
Entrance Mach No.	.213	.222
Exit Mach No.	.520	.52
Entrance stagnation temperature, °F	946	1063
Exit stagnation temperature, °F	2221	2236
Entrance stagnation pressure, psia	321	343
Exit stagnation pressure, psia	212	228
Single tube thrust coefficient*	0.267	0.192
Side reflector hole radius, in.	.040	.040
Side reflector average volumetric power density, Mw/ft^3	.3	
Maximum reflector wall temperature, °F	2300	
Reflector exit gas temperature, °F	2263	
Total reactor power, Mw	568	562
Total reactor flow rate, pps (includes 1.1% for reflector cooling, 1.4% for control rod cooling, 4.1% for structure cooling)	1604	1719
Average exit gas temperature °F	2215	2230
Overall reactor porosity, % (including missile skin correction)	37.9	

* For design-point operation the effect on thrust coefficient of varying fuel element exit Mach No. is shown in Fig. III-6.

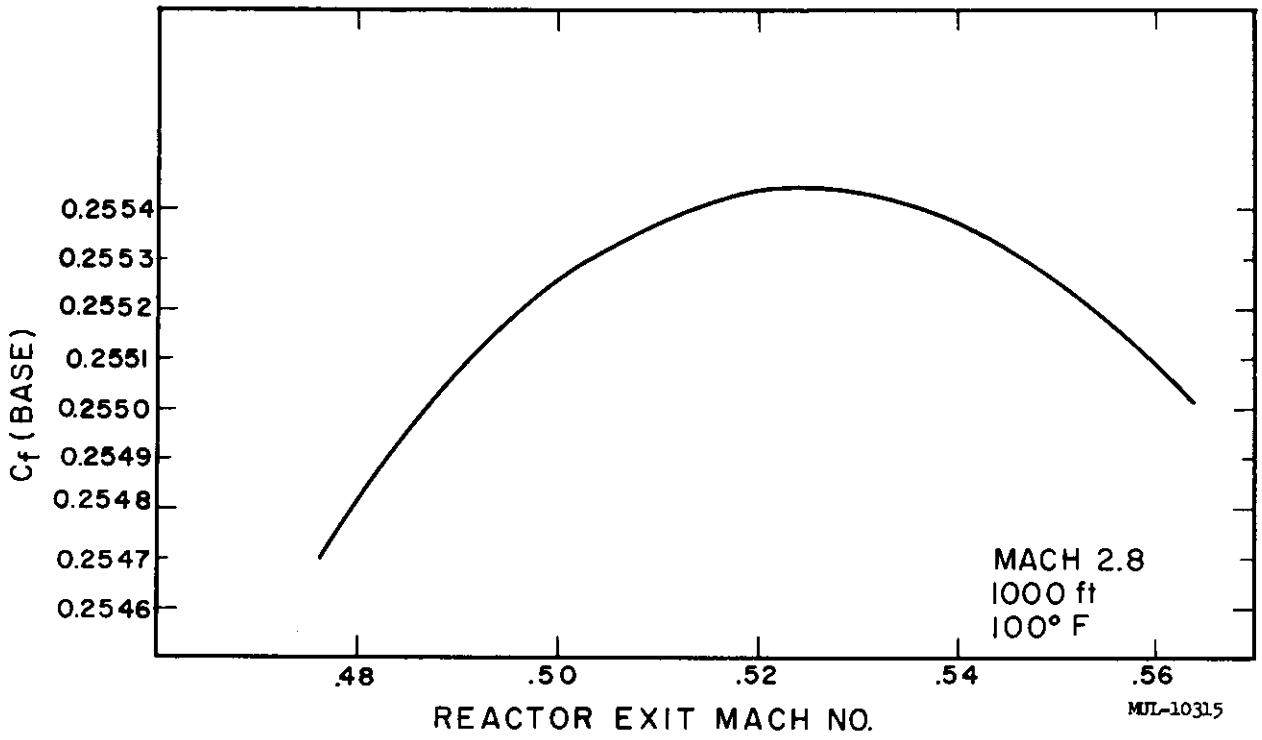

Fig. III-4. Thrust coefficient vs exit Mach No.

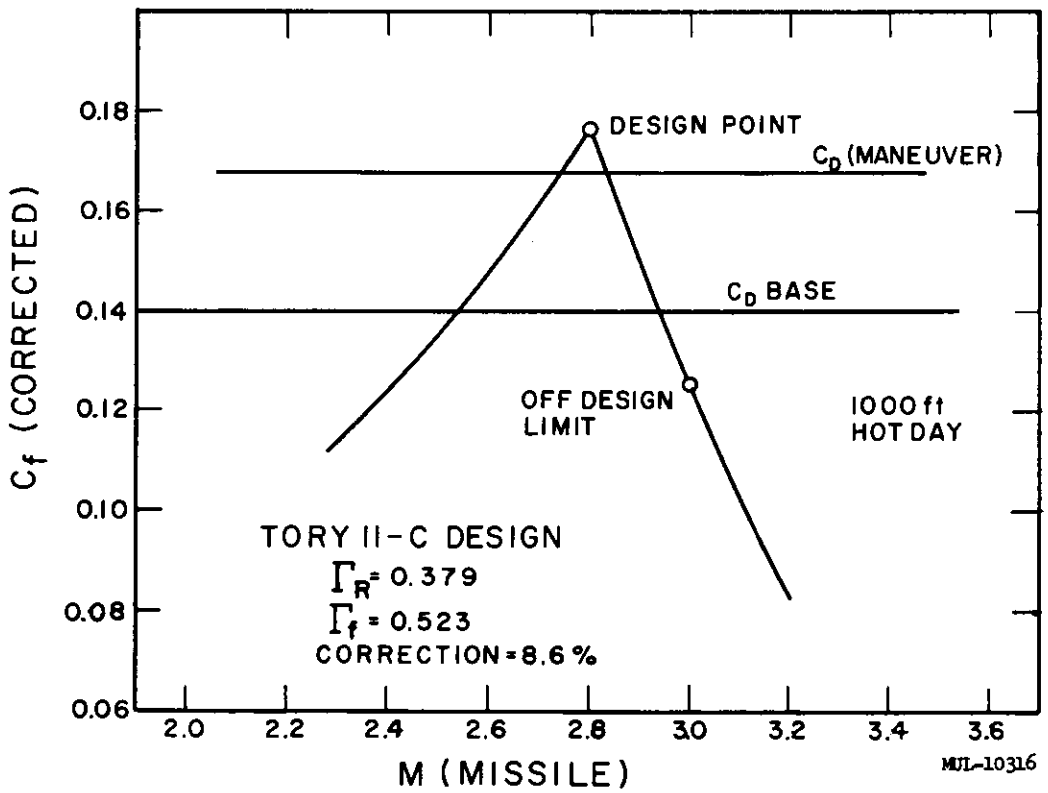

Fig. III-5. Thrust coefficient vs Mach No.

The predicted pressure, temperature, Mach No., and power profile of a typical fuel element is given in Fig. III-6 and Fig. III-7 for critical and supercritical diffuser operation with a $3/4/1/4$ sine power distribution.

The fuel element elastic thermal stress parameter, $\sigma k/E\alpha$, is plotted as a function of axial position in Fig. III-8. The Tory II-A curve is also presented for a comparison. Neither set of curves were corrected for end or shape effects ($\sim$ -16% error).

In the fabrication of fuel elements, some geometrical tolerance must be specified. The effect of fuel element hole size variation on the thrust coefficient is presented in Fig. III-9. The reference area used is the gross area of a single fuel element. In making the perturbation calculation, it was assumed that only one full-length fuel element of the reactor had a flow channel diameter different than that desired.

In computing the axial force acting on the reactor (at supercritical diffuser operation), pressure losses due to expected exit, entrance, and offset conditions must be included. An exit stagnation pressure loss of 1%, an entrance loss of 0.4%, and an offset loss of 1.8% will probably be experienced. Including these effects, the axial thrust loading on the reactor is calculated to be 122.7 psi. This value should be used in reactor design calculations. The total axial force on the 54-in. reactor is expected to be 281,000 pounds. The gross thrust at the design point is about 35,000 pounds.

The axial force level of 122.7 psi is considered nominal. No safety factor has been included. Since the friction factor of the fuel tubes may be higher than presently anticipated, the reactor axial loading may be found to be greater than 122.7 psi by as much as 6%. The flow channels of entrance and exit reactor sections must be carefully tapered to insure the low parasitic losses used in the calculations.

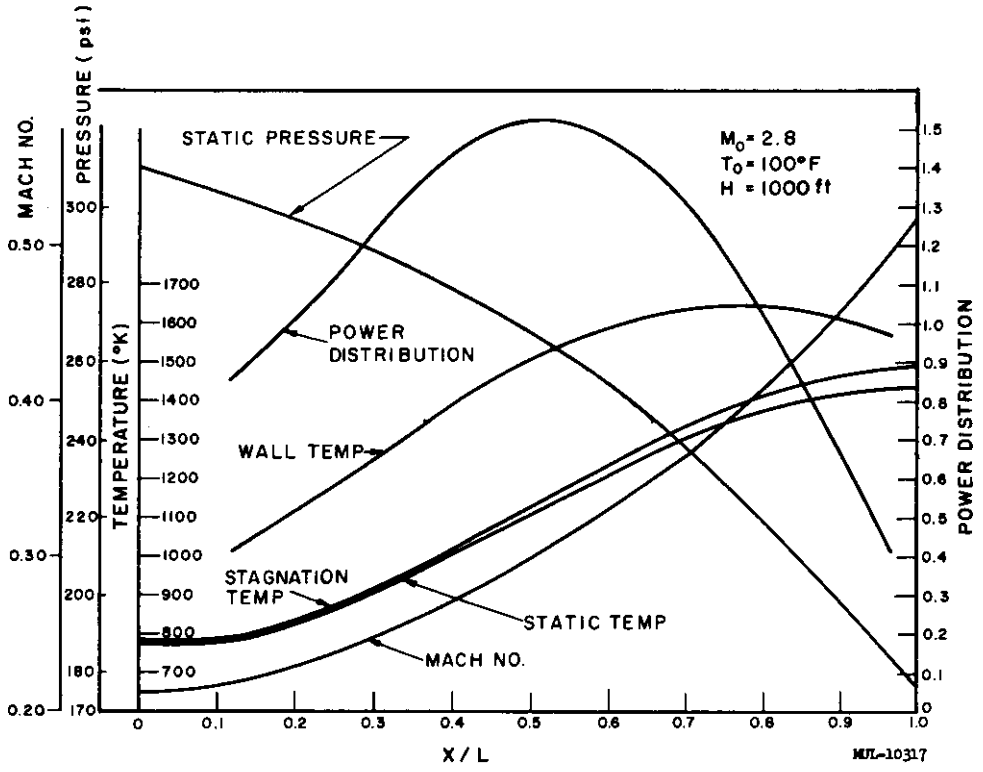

Fig. III-6. Tory II-C, design point.

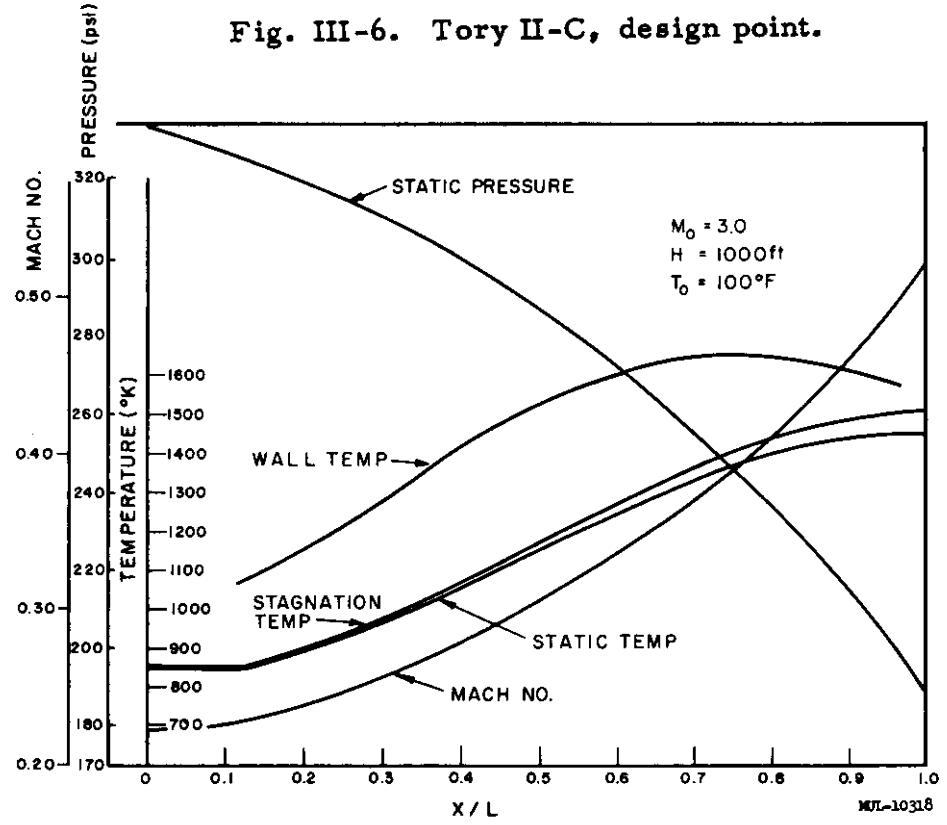

Fig. III-7. Tory II-C, Mach 3.0.

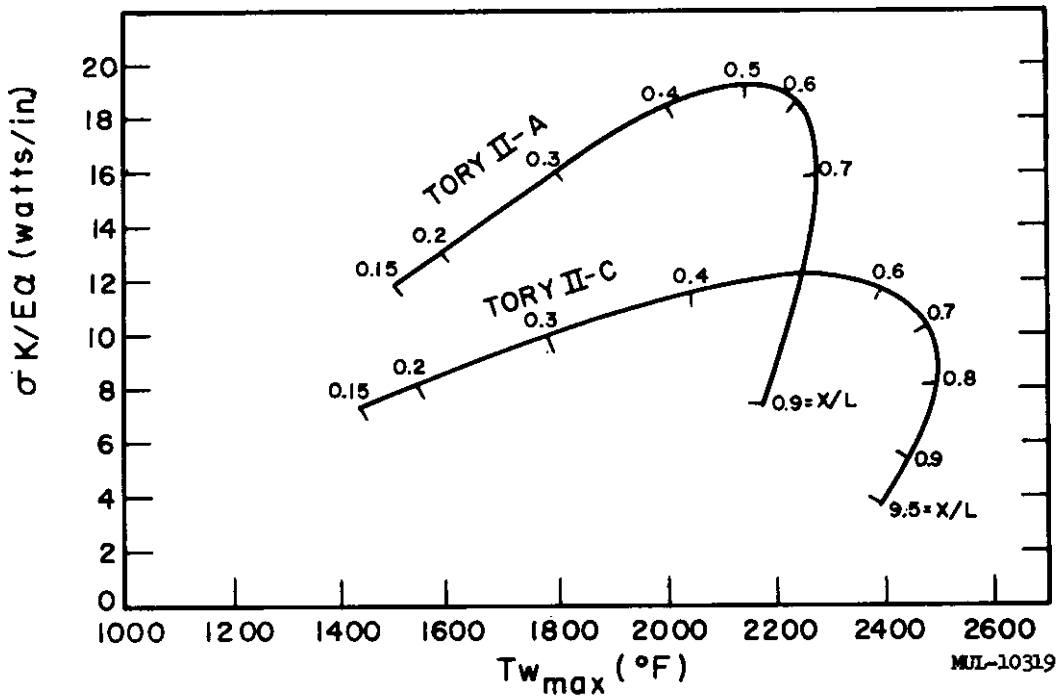

Fig. III-8. Fuel element elastic thermal stress.

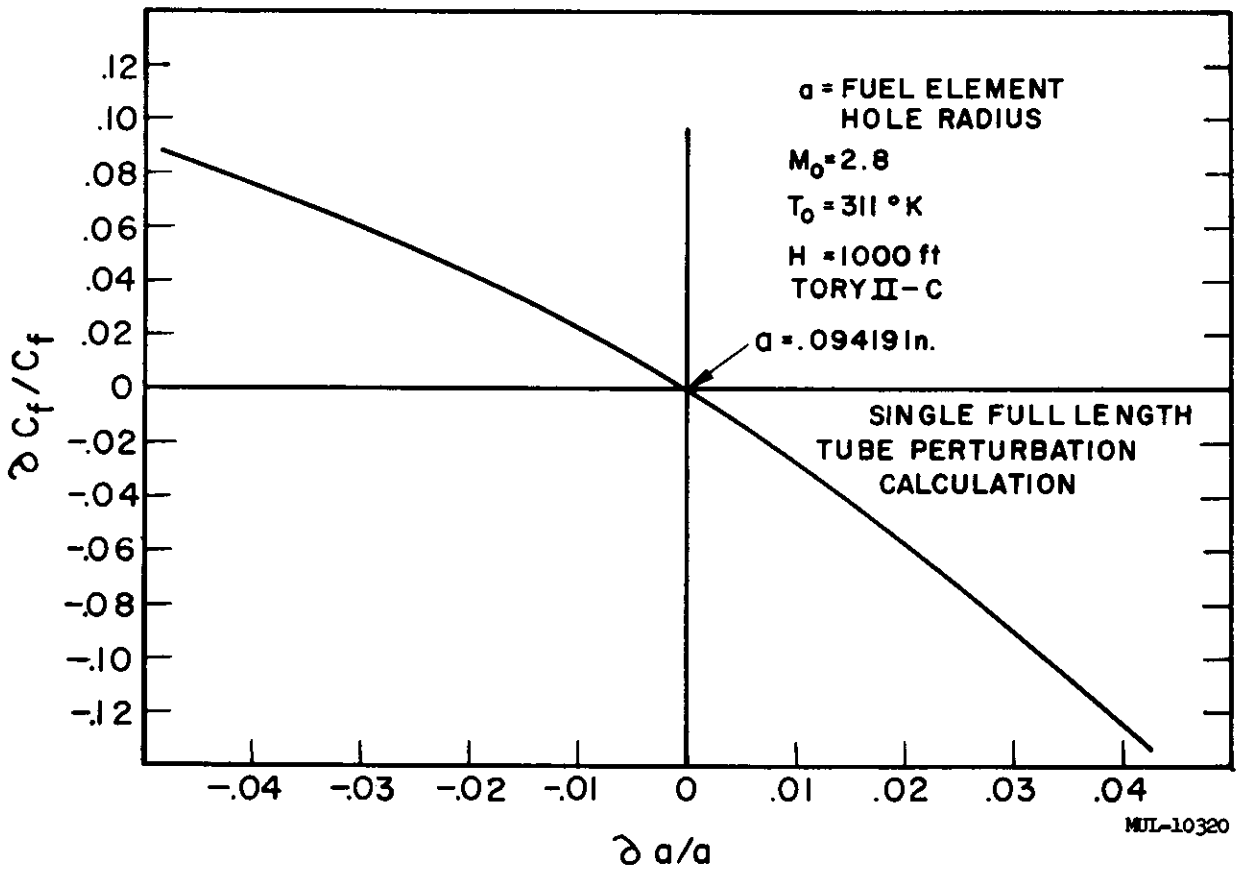

Fig. III-9. Single tube thrust coefficient variation vs fuel element radius variation.

SECTION III. NEUTRONICS

All computation during this period has been made on the following reactor configuration (at 1700°K):

Total length: 60.2 in.

Core diameter: 48 in.

Reflector thickness: 3 in.

UO_2 mass: 50 or 100 kilograms

Reflector porosity: 0.05

Volume fraction of Structural material (molybdenum): 0.00289

The 50-kg reactor is critical with a core porosity of 0.5639.

The 100-kg reactor is critical with a core porosity of 0.5921.

To start the reactor we must go from 300°K to 1700°K. Since we have a negative temperature coefficient of reactivity we must have excess reactivity built into the reactor so that it will remain critical at 1700°K. A number of things affect reactivity: fission product poisoning, initial heating of the reactor, burn-out, fuel diffusion into the air stream, etc. In addition the controls must allow several percent of negative reactivity for shutdown when the reactor is cold.

The change in reactivity during the initial heating is due to density changes ($\Delta\rho$), changes in the thermal spectrum ($\Delta\mu$), changes in the radial dimension (ΔR) and in the axial dimension (ΔA). Here we shall find it convenient to express change in reactivity in terms of percent change in the effective multiplication factor ($\% k_{eff}$). The overall change in reactivity going from 300°K to 1700°K for the Tory II-C reactor is given below along with the itemized breakdown:

For the 50-kg reactor, $\Delta k_{eff} = -6.43\%$

$\Delta\rho = -4.28\%$

$\Delta\mu = -3.84\%$

$\Delta R = +1.16\%$

$\Delta A = +0.53\%$

For the 100-kg reactor, $\Delta k_{eff} = -3.76\%$

$\Delta\rho = -3.96\%$

$\Delta\mu = -1.08\%$

$\Delta R = +1.02\%$

$\Delta A = +0.26\%$

Zenon is the most troublesome fission product poison in reactors and has been considered in Tory II-C after a 10-hour run at 600 megawatts. The zenon present produced a 1% drop in k_{eff}. Fuel loss due to burn-up and out-diffusion are estimated to account for another 0.5% in k_{eff}. About 3% negative reactivity is necessary for shutdown bringing the total Δk_{eff} to 10.9% and 8.26%, respectively. Several methods to control this much reactivity were considered. Since the complete removal of the reflector resulted in a 25% decrease in k_{eff} a control rod system in this region is not feasible (we would need at least 45% of this amount).

A central control rod of 20-mil 60% platinum-40% rhodium on a 2-in. radius produced only a 5% drop in k_{eff}. If a completely "black" absorber is put in the 4-in.-diam region (black from 1 kev down), we obtain a 12.7% change in k_{eff}. Since this is in a region of maximum effectiveness under flat loading the % change in k_{eff} would decrease when we level the radial power profile. With the control rods that are now available it is considered that this configuration cannot give us the needed 12% in k_{eff}.

A two-dimensional problem was run which calculated the effectiveness of six 1-1/4-in. diam "black" (from 1 kev down) rods located 4-1/2 in. in from the outer boundary of the core. Still using flat loading this configuration produced a change of 18.8% in k_{eff}. With fuel varied so as to produce a flat power profile this figure is expected to increase considerably.

SECTION IV. NUCLEAR CONTROLS

During the reporting period, close to 100% of the controls development is represented by the effort being carried on by a subcontractor. The development program aims for a 1200°F electro-pneumatic-mechanical control system. LRL's major role has been the outlining of realistic specifications for the supplier to work toward and direction of their efforts to insure compatibility with the overall reactor system.

Effective March 21, 1960, the scope of the supplier, Phase V efforts (electro-pneumatic actuator development) was changed. Previously the objective of Phase V was development of a 20-in. stroke actuation system to run as high as 750°F with no vibration or g-loading environment specified. The design specifications now require instead a 40-in. stroke actuator to run over 2×10^4 cycles at 1200°F, with vibration environment and continuous axial g-loading specified. The detail design specifications for Phase V (amended) are shown in Table III-3. A schematic outline of the actuator assembly is shown in Fig. III-10.

The target date for completion of Phase V acceptance tests at the supplier is January 15, 1961, with delivery of the rebuilt subsystem at LRL by March 15, 1961. The supplier has laid out a detailed schedule for completion of each phase of the component and subassembly work.

Progress on Phase V to date is briefly summarized below:

1. Pneumatic actuator
   a. Bearing and lubrication study. Detailed specifications have been formulated.
   b. Pneumatic motor. Preliminary and final design complete.
   c. Transmission and housing. Detail design complete. Specifications established.
   d. Room temperature motor. Design, fabrication, complete. Evaluation underway.
2. Servo valve
   Design, material selection complete. Fabrication underway.
3. Transducer
   Specifications established. Design and fabrication complete. Test underway.
4. Electronics
   Specifications established. Design complete and procurement underway.

Table III-3. High Temperature Electropneumatic Servo Design Specification

1.	System gas supply pressure (min)	1000 psig
2.	Actuator gas supply pressure	1000 psig (operable through 90-1000 psig)
3.	Maximum steady state flow per actuator	Less than 50 scfm at 1000 psig
	Maximum flow allowable per actuator	300 scfm at 1000 psig
4.	System filtration	10 micron
5.	Connections mechanical electrical	Conventional type: make recommendations for high temperature quick disconnects; LRL assumes responsibility for development of high temperature quick disconnect.
6.	Ambient temperature range Fluid temperature range	Room temperature to 1200°F Room temperature 1060°F High temperature test condition 1200°F ambient 1060°F fluid
7.	Stroke	40 inches
8.	Dynamic response The closed loop frequency response at ± 0.02-in. amplitude with zero-g loading and zero average speed at any position of the output member shall have less than 90° phase shift at:	15 cps at 1000 psig 10 cps at 360 psig 3 cps at 90 psig
9.	Controls	Individual electrical, 0 to ± 10 volts d-c (rod center position at zero volts) Positive volts represent positive reactivity (rod is withdrawn)
10.	Basic mechanism	Actuator with linear output
11.	Disposal of actuator discharge	Manifolded to atmosphere
	Ambient pressure and exhaust environment for design consideration	P_s / P_e / P_a (psig) 1000 / 0 / 0-300 360 / 0 / 0-300

(continued)

Table III-3 (continued)

12.	Life tests (minimum requirements)	
	Room temperature tests at 1000 psig	10^4 cycles at 1 cps with 8" p-p amplitude 10^4 cycles at 10 cps with 2" p-p amplitude 100 full displacement steps in each direction 100 scrams
	High temperature tests 1200°F ambient 1060°F gas 1000 psig	10^4 cycles at 1 cps with 8" p-p amplitude 10^4 cycles at 10 cps with 1" p-p amplitude 50 full stroke steps in each direction 50 scrams
	Superimpose slow ramp on cyclic tests	
13.	Saturation velocity (vernier rod)	Greater than 60 in./sec at 1000 psig
14.	Acceleration at zero velocity with zero-g acceleration and vibration environment	Greater than 10g at 1000 psig
15.	Position transducer and read-out	Electrical instrument: must be capable of operation throughout the temperature range from room temperature to 1200°F; excitation frequency to be equal to or greater than 1000 cps; not a multiple of 60 or 400 cps; transducer to be folded or integral part of actuator with objective to minimize overall length
16.	Gas supply, regulating and shut off valves	Furnished by LRL
17.	Space envelope of actuator assembly	Minimum cross sectional area perpendicular to direction of linear motion See Fig. III-10 for load and actuator configuration in a typical application
18.	Actuator overall length	Less than 3 stroke lengths excluding control rod and connecting members
19.	Center spacing between actuators	Not specified (5 in. maximum preferred)
20.	Actuator weight	Minimum consistent with airborne practices
21.	Location of electronic equipment	100 ft transmission cable to actuator

(continued)

Table III-3 (continued)

22.	Servo amplifiers	Industrial quality, room temperature, negligible radiation, transistors may be used, operational amplifier capability required
23.	Position resolution	± 0.02 in. to be determined with a sine or triangular wave input signal at 0.1 cps
24.	Linearity	± 5 percent of stroke over temperature range of operation
25.	Fail-safe insertion characteristics	40 in. in a maximum of 0.25 sec at 1000 psig supply and zero-g
26.	Vibration environment and acceleration	6g, 3 axes, 0-3000 cps, 6g continuous tending to pull rod out of core at 1000 psig supply and room temperature
27.	Control rod and support	Furnished by LRL
28.	Power media for testing	Nitrogen and air
29.	Power media for design	Air
30.	Weight of control rod	20 pounds
31.	Allowable control rod assembly friction force	25 pound starting and sliding friction
32.	Cooling system	Ambient (Ram) Air
33.	Transient response	Equal to or less than 12 percent of demanded step or 0.1 in., whichever is greater
34.	System stiffness	Capable of holding 20-pound load within resolution with continuous 6g axial load at 1000 psig
35.	Servo valve	Electropneumatic servo valve capable of operating throughout temperature range from room temperature to 1200°F, and mechanically biased to insert rod in case of electrical input power failure
36.	Full stroke displacement time under servo control	Less than 0.75 sec
37.	Vibration tests	To be determined, also method and responsibility to be determined
38.	Relative stability over range of temperature and pressures (closed loop under conditions of Item 8)	Gain margin equal to or greater than 6 db; phase margin equal to or greater than 50°

(continued)

39.	Integrated radiation dosage	10^8 rads total 5×10^7 rad fast neutrons 3×10^7 rad thermal neutrons 2×10^7 rad gammas
40.	Rod lock mechanism	Fail safe locks rod in scram position (fully inserted) until supply pressure is available
41.	Number of thermal cycles (room temperature to 1200°F)	30 minimum; actuator should fulfill all of the above specifications before and after thermal cycling
42.	Time period for thermal cycle	5 minutes room temperature to 1200°F
43.	Power source	120V, 60 cps, 1-phase 480V, 60 cps, 3-phase 400 cps, 120V, 1-phase

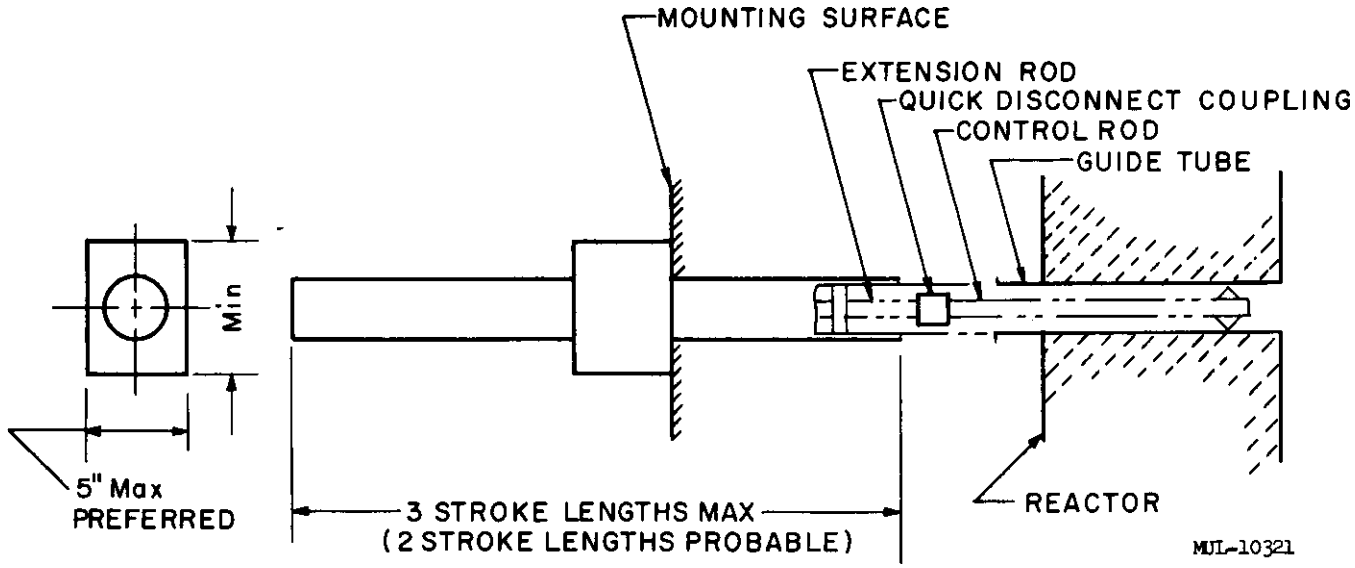

Fig. III-10. Space envelope of actuator assembly and typical coupling to load.

SECTION V. ENGINEERING – REACTOR DESIGN

A. TORY II-C-1 REACTOR

Unit Cell Studies

Analysis has centered on choice of a unit cell in all sizes and configurations. Larger unit cells than the one considered previously result in lower "tension" metal temperature. In this way the metal temperature may be reduced sufficiently to permit use of non-refractory alloys. If an oxidation resistant material is used, arguments favoring solid vs hollow tension members disappear. Unperturbed cooling of the metal can be more certainly assured using hollow tension members. The most effective method of obtaining a temperature drop between hot fuel elements and a tension tube is to allow only radiative heat transfer. This also results in low degraded fractional areas in the unit cell by limiting introduction of extraneous (insulating) materials.

Figure III-11 shows the general arrangement of an attractive basic unit cell. The unit cell consists of 213 fuel elements grouped in a hexagonal array approximately 4 in. across flats. The complete reactor will contain approximately 175 unit cells. Peripheral unit cells will consist of a partial basic unit cell and will contain unfueled BeO elements in a 3-in.-deep peripheral region. This choice of unit cell size is consistent with the capacity of existing high-temperature blowdown test facilities. Development testing on a unit cell basis can thus proceed using full-scale reactor parts.

Tension members of Hastelloy R-235 are being considered to carry the reactor pressure drop load. Experience with this alloy in the Tory II-A core has shown it to have adequate strength for this application at temperatures to 1650°F. Maximum tension tube wall temperature is below 1600°F.

Separation between surrounding hot fuel elements and the colder tension tube is provided by ceramic washers. These washers are hexagonal in shape and exactly replace twelve fuel elements. The washers are unfueled BeO. Neutronic heating in the washers keeps their outer perimeter at a temperature near that of surrounding fuel elements. Heat deposited in the insulating washers is radiated to the tension tubes.

The pressure drop load on the fuel elements is transferred to the tension rod through two BeO plates and a refractory metal alloy base block. Holes in the first BeO plate are sized to collect the flow from three fuel elements. Holes in the second BeO plate are sized in turn to collect the flow

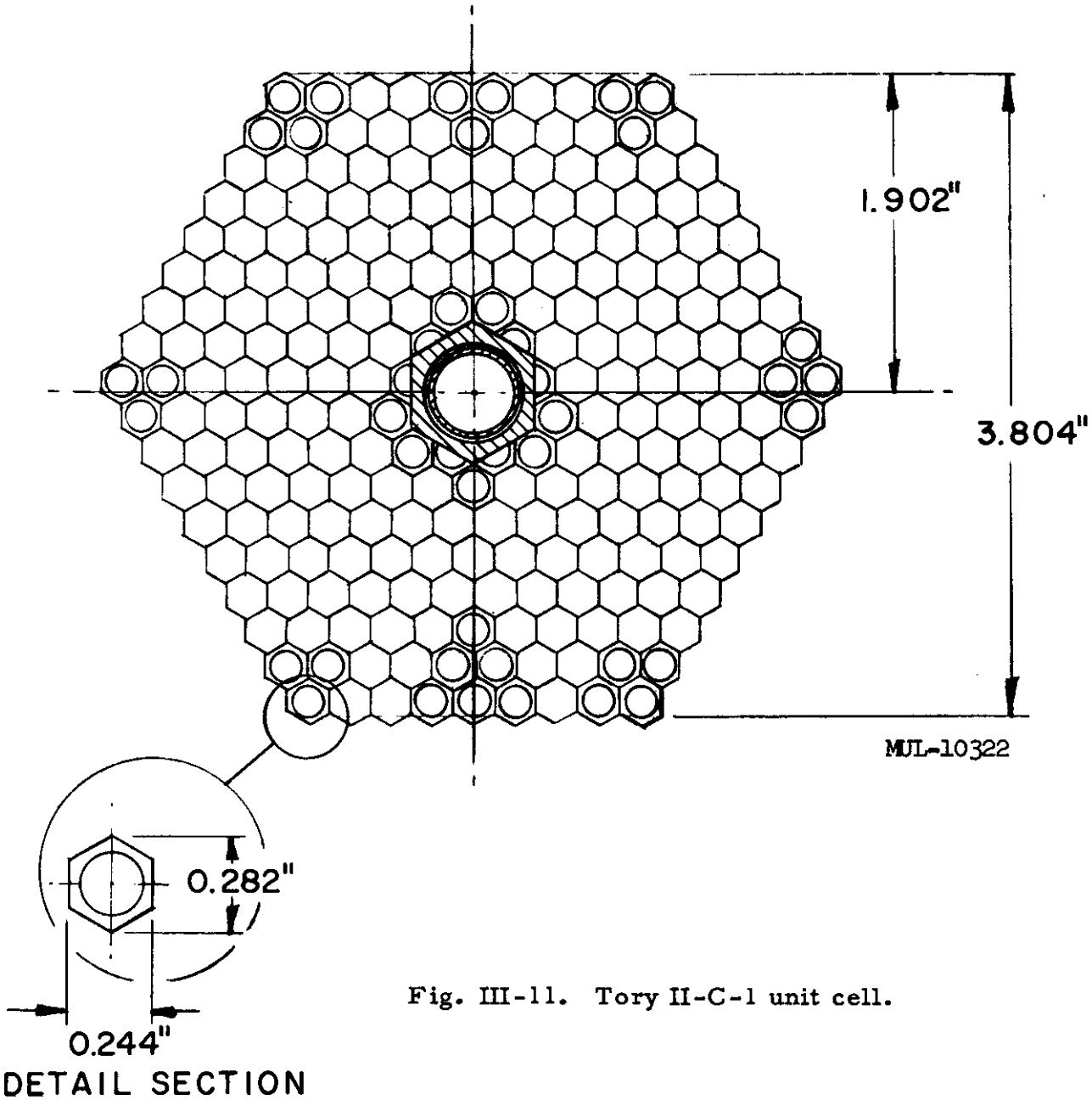

Fig. III-11. Tory II-C-1 unit cell.

from three holes in the first BeO plate (total flow from nine fuel elements). Holes in the base block are sized to match those in the second BeO plate. The arrangement of holes used here is advantageous in these ways; misalignment effects of fuel elements with holes in the load transfer blocks are minimized, fabrication of the BeO plates and the base block is simplified, and reliability of the oxidation protection coating on the base block is improved. Load is transferred from the base block to the tension tube through an insulated flange on the tension tube.

Base Block Development

Selection of a unit cell configuration described above leaves little choice among materials suitable for the 2300°F base block. Ceramics are excluded for their frangible properties and super alloys for their low strength. Of the refractory alloys commercially available, columbium and tantalum base alloys have order-of-magnitude better oxidation characteristics than molybdenum base alloys. Since very high strengths are not required for the base block and because oxidation protection of columbium has received considerable attention, several columbium alloys are being studied. At least one tantalum base alloy is also being studied.

B. TORY II-C-2 REACTOR

The critical development area in the Tory II-C-2 Reactor is in the design and fabrication of the large dome structure. The suitability of several materials and fabrication techniques are discussed below.

Material Requirements

It is assumed that relatively pure high density ceramic materials are required. It may be that cheaper grades of refractories can meet the requirements. Some of these lower grade refractories are presently made commercially in very large shapes, and it is planned to evaluate some of these materials. Some of those of interest are silicon-nitride-bonded silicon carbide, electro-cast alumina-zirconia-silica refractory, and commercial ramming mixes.

1. Oxidation Resistance

Data from a number of sources on several oxides and on silicon carbide indicate that for the intended application, oxidation is not apt to be a problem even to temperatures higher than the present range of interest.

2. Compressive Strength

Analysis indicates that compressive strengths of the order of 3000 psi for flight duration (several hours) is a minimum requirement. Expected temperature of the base dome is 2300°-2400°F. Compressive strength data for these materials at this temperature is generally lacking.

Carborundum's KT-SiC may have the required compressive strength.[1] Tensile tests of SiC were conducted at 1200°C (2200°F). The most highly stressed specimen sustained 8000 psi for 84.8 hours without failure. The others sustained lower stresses without failure. Compressive strength should be much greater than tensile strength. There is considerably more data on the effect of temperature on flexure strength. Common oxides start to lose strength rapidly at about 2000°F,[2] KT-SiC at 2700°F, however, has about 80% of its maximum strength.[3]

3. Fabricability

For fabrication of large oxide shapes, two basic techniques are available. They are cold-shaping and sintering, and hot-pressing. With the first method shrinkage is typically 20% and variation in shrinkage requires complete machining of the fired pieces if close tolerances are necessary. Machining with diamond tools is slow and expensive.

In hot-pressing, the length to wall-thickness ratio desired in the dome (150:1) is apparently much too high for precision hot-pressing, therefore, subsequent diamond machining would also be necessary.

KT Silicon Carbide is formed cold (consisting initially of about 75% minus-100 mesh granular SiC, the balance graphite and plastic binder). It can be green-machined externally with carbide tools and recent demonstrations have shown that holes can be green-drilled for the dome with air-cooled diamond core drills. Subsequent firing produces a dense, nearly pure silicon

---

[1] "The High Temperature Properties of Ceramics and Cermets", E. Glenny and T.A. Taylor, Powder Metallurgy, 1958, No. 1/2.

[2] "Oxides for High Temperature Applications", W.D. Kingery, Advance Paper for the High Temperature Technology Conference held at Asilomar, California, Sept. 6, 7, 8 and 9, 1959.

[3] "Selection of Materials for Hypersonic Leading Edge Applications", Anthony and Pearl, Institute of the Aeronautical Sciences No. 59-111.

carbide body with a shrinkage of about 1%. (3-1/2-in. pieces have exhibited a shrinkage of 0.4 percent when referred to the mold). This amount of shrinkage should allow use of the piece with little or no machining after firing.

4. Crack Resistance

The dome will have a temperature distribution dictated by the reactor. Temperature changes will probably be sufficiently slow that thermal shock is not a problem.

Steady state thermal stresses will be approximately proportional to the quantity $E\alpha$ where E is Young's modulus and α is the expansion coefficient. Measurements by Bell Aircraft Co. give $E\alpha$ (maximum value) = 90 for KT-SiC (using psi and °F). The value for BeO and Al_2O_3 is about 250 at temperatures of interest. KT-SiC shows a clear advantage but the oxides may be satisfactory. Resistance to this kind of thermal stress may be compared by the quantity $\sigma/E\alpha$ where σ is the tensile strength. A high value of this quantity minimizes the problem of thermal stresses.

The tensile strengths of KT-SiC and the common oxides are similar at 2000°F, but KT-SiC has a clear advantage over 2500°F. Hot-pressed silicon carbide has been produced by Alfred University and Carborundum with flexure strengths of about 50,000 to 60,000 psi at 2500°F. Hot-pressed BeO of very high density has been made with flexure strengths of about 40,000 psi at 2200°F by Atomics International. These high strengths were achieved at the expense of reduced ductility along with a considerable increase in fragility and ease of crack propagation. Therefore, very high strength compositions may be undesirable.

Fabrication of KT-SiC Dome

In preparing perforated SiC shapes the holes can be made up to 50 wall thicknesses by pressing. The deeper holes demanded for a base dome require more elaborate techniques. Previous drilling experience on green shapes by Carborundum was not very encouraging. Their biggest difficulty was breaking the thin web between holes.

Consequently, drilling green and fired shapes was studied by LRL at Hoffman Drill Co., Punxsutawney, Pa. Hoffman has had extensive and successful experience in diamond drilling hard materials.

Hoffman has now demonstrated that their diamond core drills can sink holes in fired KT-SiC at the rate of about 1 in./min. In unfired material the

rate is about 20 in./min. Considerably thinner webs are permitted than are required for the base dome. Their preliminary estimates of cost (relating only to the cost of the core drill proper) are $3.50/in. in fired SiC and $0.005/in. in unfired pieces.

Owing to this demonstrated drilling capability, development of techniques for pressing the holes has not been pursued. With drilling it is feasible to have holes with nonparallel axes, as is likely to be required in this instance.

Model Tests

General

The principal model tests consist of applying hydrostatic pressure through a diaphragm to the flat face of a model supported in a conical seat.

Proper structural similitude in this case requires that:

1. The model maintains complete geometric similarity.
2. The model is constructed of the same material as the prototype.
3. The material should be uniform and continuous. If these relationships hold, the pressure-stress relationship will be identical in both model and prototype. The load produced by the pressure and the resisting strength both vary as the square of the scaling factor.

Complete geometric similitude is not feasible for small perforated models however. These would be difficult to machine and the web thickness could reduce to an order of magnitude where grain size could no longer be ignored. Geometric similarity would be maintained at the expense of material consistency. However, the ratio of hole-to-dome diameters should have little effect if the number of holes remains large and equal porosity and similar hole patterns are maintained.

The high cost and fabrication difficulties encountered with actual materials would slow down model tests. Since, for all practical purposes, the magnitude of the rupture load is the only variable in their rupture characteristics almost any brittle material will provide most of the information required in short-time model tests.

Tests to Date

A series of 12-in.-diam plaster domes have been tested to destruction. Four of these were solid domes and eight were 50% porous with half-inch holes. Two of the latter were segmented 7-piece domes consisting of a keystone and 6 circumferential blocks.

The pressure deflection readings for the porous domes are shown in Fig. III-12. The curves are more regular than similar curves for solid model domes. Failure in these models occurs between 130 psi and 210 psi. There does not seem to be any significant decrease in static strength with segmentation for the 7-piece specimens.

The photograph Fig. III-13 shows both a one-piece and a segmented dome while supporting pressure. Figure III-14 shows these models after removal from the test equipment. The degree of destruction is obvious. However, most of the cracks were radial and did not interfere with the ability to support load by meridional stresses.

Cylindrical compression specimens of this plaster material failed at 2960, 2370, 2650, 2370, and 1600 psi. This indicates a factor of 10 to 15 between stress and pressure load in consistent units. It is significant that in a cold static short-time test, ordinary plaster-of-paris supported a load roughly equivalent to the design load. This indicates that a material with a lifetime high temperature strength of less than 5000 psi may be acceptable for an actual dome.

Elevated Temperature Model Test Equipment

For high temperature endurance testing the small hydrostatic test unit shown in Fig. III-15 has been built. This unit can accommodate a 3-1/2-in.-diam model.

The test equipment consists of a frame and seat machined from a single piece of molybdenum. After the dome has been set in place a pressure chamber with a replaceable moly diaphragm is inserted above it. The entire unit will then be placed in an inert atmosphere furnace for the test. The low volume of the pressure vessel and the small diameter inlet tube remove the danger of an explosion in the furnace. The pressure chamber must be faced off and a new diaphragm welded on after each test due to temperature embrittlement.

This type of construction eliminates fasteners and permits the use of very high pressures. Frame design capability is 2500 psi at 3000°F for 100 hours. This is ample to demonstrate the maximum strength capabilities of any of the high performance ceramics and to justify extrapolation of model test results.

Several SiC models have been built and tests on this equipment are now in progress.

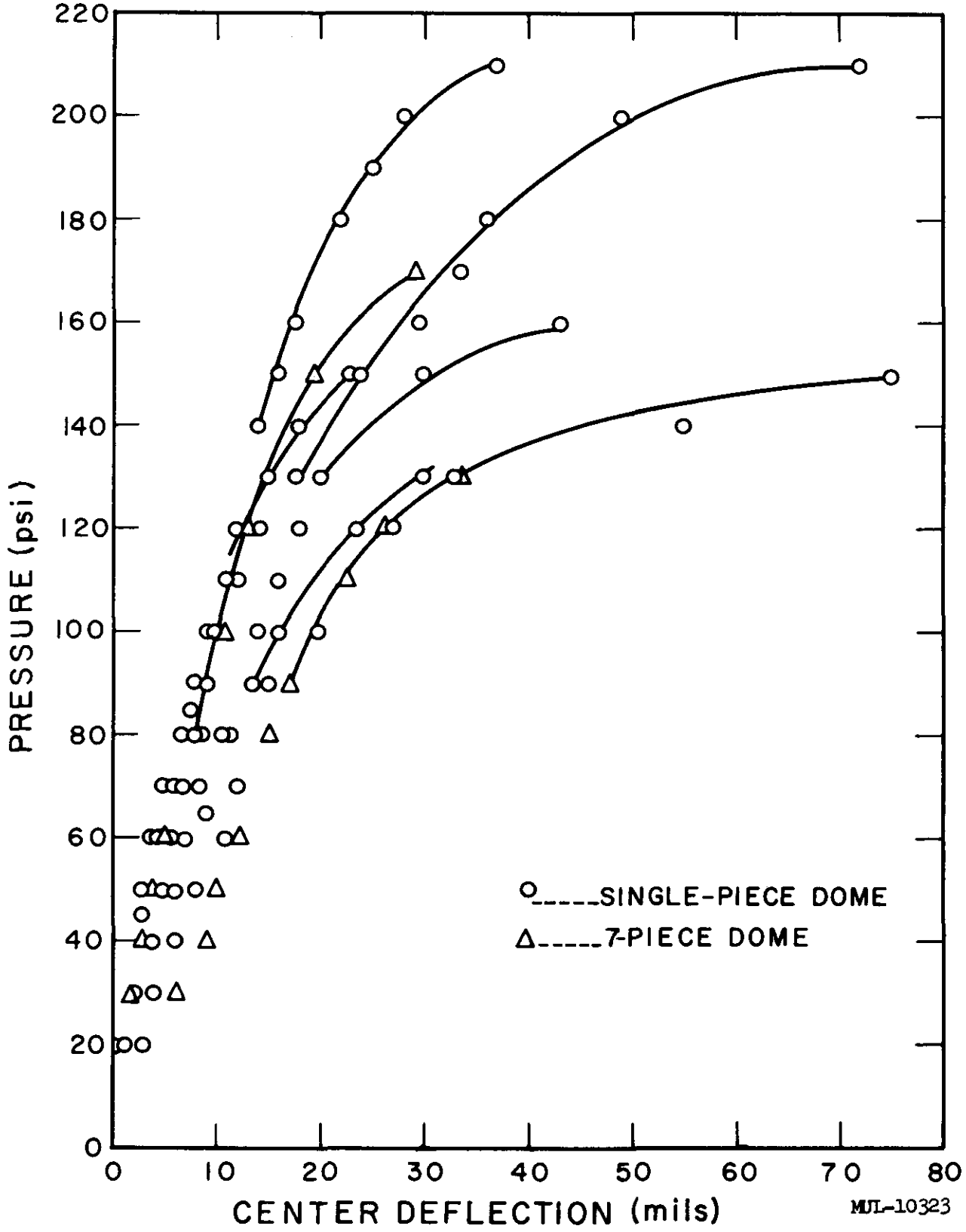

Fig. III-12. Pressure deflection porous plaster domes (50% porosity).

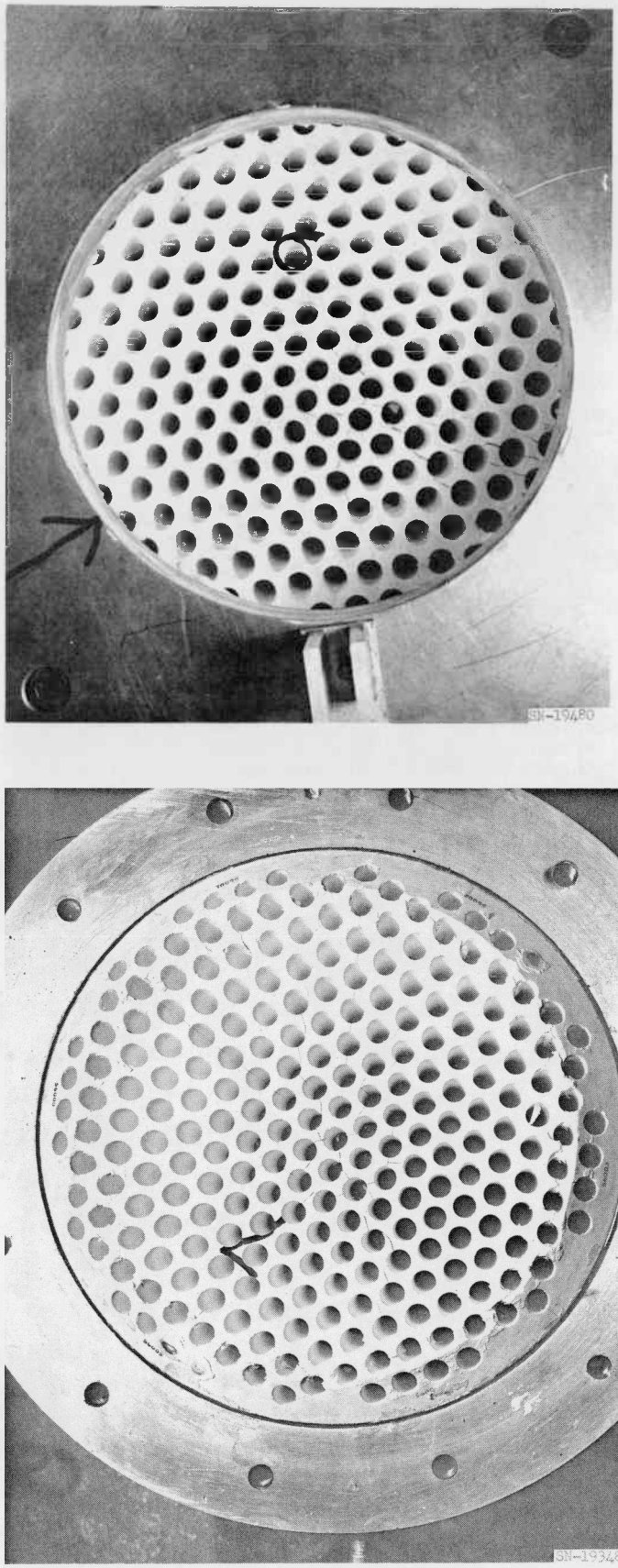

Fig. III-13. Upper: Single-piece dome supporting maximum pressure. Almost all major cracks shown had occurred 20 psi earlier. Below: Segmented dome after test. Dome had supported 130 psi while cracked as shown.

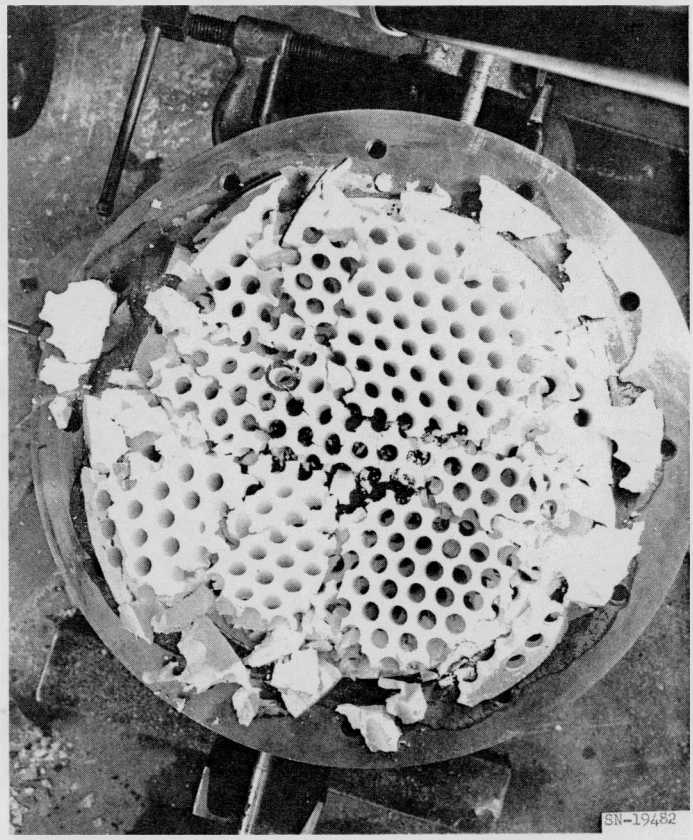

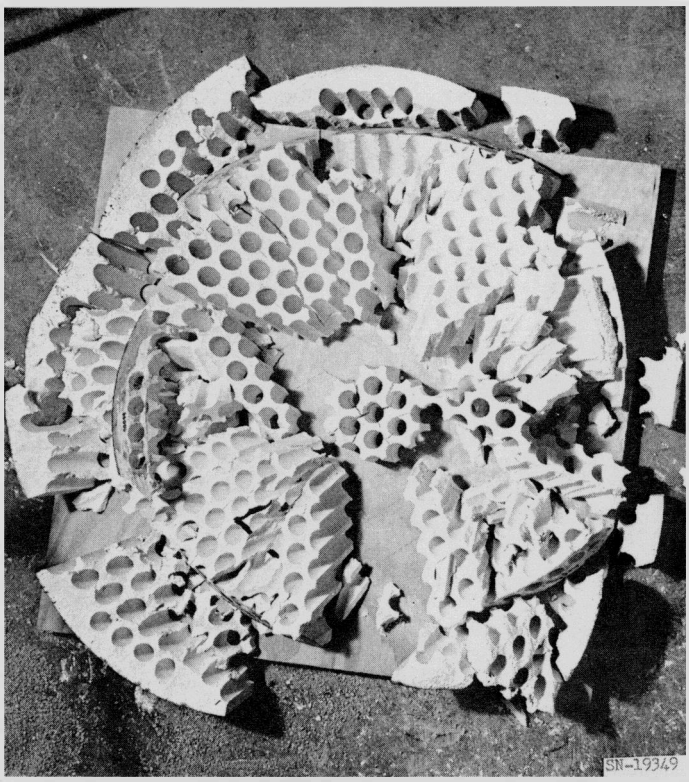

Fig. III-14. Upper: Single-piece dome removed from the test rig, showing extent of damage. Lower: Segmented dome removed from the test rig.

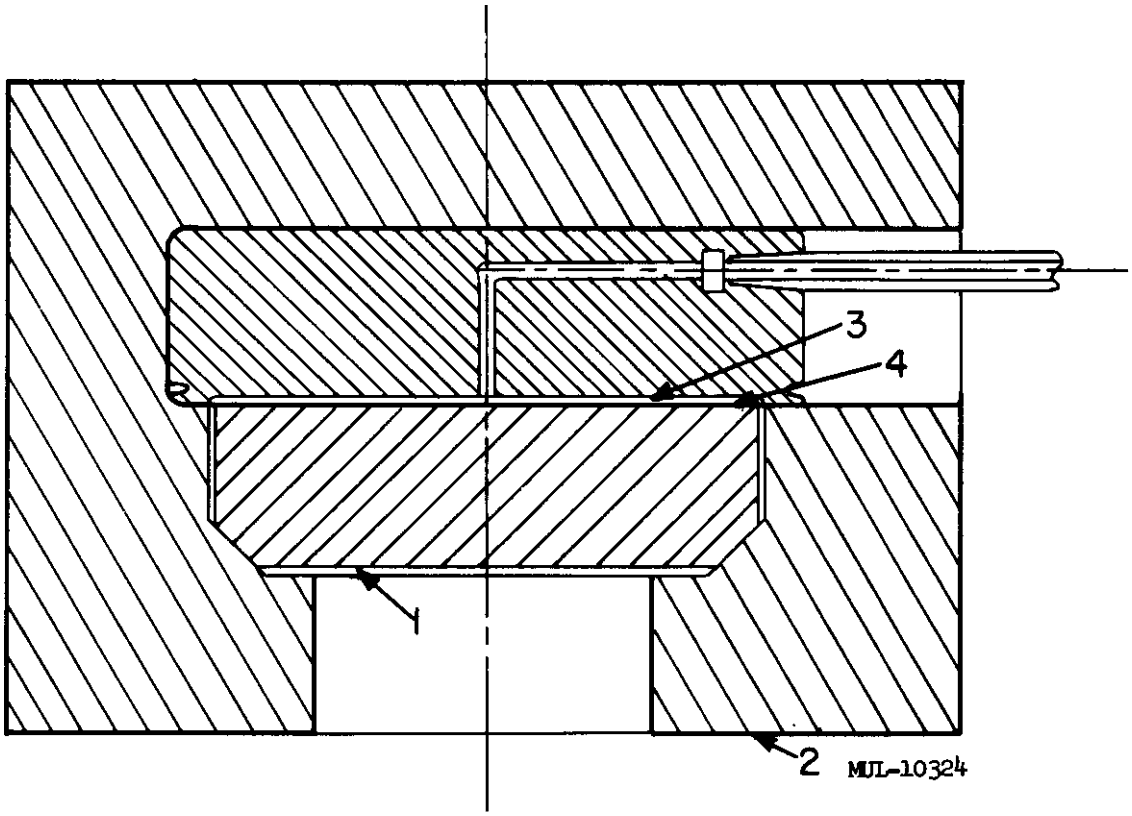

Fig. III-15. High temperature test cell. 1. Ceramic dome. 2. Moly frame. 3. Pressure chamber. 4. Moly diaphragm.

Both Tory II-C-1 and Tory II-C-2 reactors will utilize hexagonal fuel elements approximately 1/4-in. across flats with about a 3/16-in. diam hole. The elements will be 4-inches long.

TEST VEHICLE

Conceptual design of the following Tory II-C test vehicle items is complete.

1. Car. A special flatcar of standard railroad gauge will be fabricated. The purpose of this car is to support and transport the test reactor. The car will be 38 ft long. It will have a low-power electrical motor drive which can move the car for short distances. The car will be equipped to use the same tracks, outriggers and bunker as the Tory II-A car.

2. Inlet Ducts. The inlet ducts will consist of a forward diffuser section, an aft diffuser section, and a controls section. The ducts will be welded fabrications of heat-resistant nickel base alloys. The forward diffuser section will be designed to use the existing Tory II-A remote duct coupling. The diffuser throat diameter will be approximately 18 in. The diffuser divergent

half-angle will be 6°. The aft diffuser section will connect to the forward diffuser section and the controls section with bolted flanges. The control section to reactor coupling will be of the V-band type. Reactor control rod actuators will be located in the control section.

3. Nozzle Section. The nozzle section will be a welded fabrication of heat-resistant nickel base alloy. This section will be extremely air-cooled by high pressure cold air from the bottle farm (reduced to a controllable 200 psi level, 100°F max temp). The internal surfaces exposed to the exhaust air will be coated with ceramic materials for added protection. The nozzle will be convergent with a short divergent section. The throat diameter will be approximately 33 in. Cooling air for the nozzle will be supplied through the bunker wall to a rigid 8-in. pipe mounted on the car. The connection to the nozzle will be through a high pressure bellows and a V-band coupling. Instrumentation rakes will be located in the forward cylindrical portion of the nozzle section. Insertion and removal to these rakes will be through diametrally opposite part in the nozzle wall.

4. Electrical. All instrumentation and electrical lines will be routed through wiring trays built into the deck of the car. The Tory II-C test vehicle will use the Tory II-A main electrical disconnect in the test bunker.

Air Supply Extension

The following facilities are to be added to Area 401 air supply system under the Phase III construction program:

Addition of a 280,000-pound capacity air storage system to increase the air storage capacity from 120,000 pounds of air at 3600 psi to 400,000 pounds of air at 3600 psi.

Modification of the compressor house to permit the installation of a third high pressure air compressor and its associated equipment.

/md